ALMA MATER STUDIORUM · UNIVERSITY OF BOLOGNA

School of Science
Department of Physics and Astronomy
Master Degree Programme in Astrophysics and Cosmology

The ISM properties of ALPINE galaxies as probed by ALMA and JWST: a comprehensive line emission modelling

Supervisor:
Prof. Francesca Pozzi

Co-supervisors:
Dr. Livia Vallini
Dr. Federico Esposito

Submitted by:
Enrico Veraldi

Academic Year 2022/2023

Contano due princìpi:
non farsi mai troppe illusioni
e non smettere di credere
che ogni cosa che fai potrà servire.
(Italo Calvino, La giornata d'uno scrutatore)

Abstract

The main goal of this thesis is to provide a self-consistent modelling of the line emission from different ISM phases (HII regions and neutral gas in photodissociation regions (PDRs)) jointly detected by the James Webb Space Telescope (JWST) and Atacama Large Millimetre Array (ALMA), respectively, in galaxies at $z > 4 - 5$.

I developed HII region+PDR models to characterize the ISM properties of galaxies within the ALPINE ALMA Large programme (*PI: LeFevre*) survey. The exploitation of the models developed in this thesis allows me to derive the predicted emission lines ratio of UV, optical, and FIR lines for galaxies as a function of three free parameters: hydrogen density (n), ionisation parameter (U) and metallicity (Z). The modelling was performed with the CLOUDY v22.02 photoionisation code (Ferland et al., 2017). I modelled the gas incident radiation using two different stellar population synthesis codes: Starburst99 (SB99, Leitherer et al. (1999)) and Binary Population and Spectral Synthesis code (BPASS v2.2.1, Stanway & Eldridge (2018)). The output of SB99 and BPASS is used to produce the illuminating Spectral Energy Distribution (SED) on the gas slab, simulated then with CLOUDY. The BPASS code considers the presence of binary stars with respect to the SB99 code. I consider stellar populations with metallicities $Z = 0.5\,\mathrm{Z}_\odot$ and $Z = 1\,\mathrm{Z}_\odot$, with a continuous star formation rate of SFR$=1\,\mathrm{M}_\odot\,\mathrm{yr}^{-1}$, and the following evolutions: a star formation started $100\,\mathrm{Myr}$ ago without being quenched, one quenched $5\,\mathrm{Myr}$ ago, and another $35\,\mathrm{Myr}$ ago.

I validated the models using observed galaxies from the VANDELS, VUDS, and CANDELS/SHARD datasets. I used the CLOUDY models to infer the expected line ratios and fluxes for relevant UV (e.g. CIII] $1909\,\mathrm{\AA}$) and optical lines ([OIII] $5007\,\mathrm{\AA}$, Hα $6563\,\mathrm{\AA}$, [NII] $6583\,\mathrm{\AA}$) with respect to the FIR line [CII] $158\mu m$. Since in the VANDELS, VUDS, and CANDELS/SHARDS dataset the [CII] $158\mu\mathrm{m}$ line is not available, I estimate it using the relation [CII]-SFR from De Looze et al. (2014).

Once I validated my models, I made predictions for the UV/optical lines for the ALPINE galaxies that will be observed by JWST in Spring 2024 (*PI: Faisst*). To do so, I assumed a fiducial metallicity of $Z = 0.5\,\mathrm{Z}_\odot$ (Burgarella et al., 2022), and estimated the values of n and U using an analytical model (Ferrara et al., 2019) that links n and U to Σ_{gas} and Σ_{SFR}, hence ultimately to the Kennicutt-Schmidt relation (KS, Schmidt (1959); Kennicutt (1998)).

My Thesis results show that the UV binary stars produce harder/bluer SED with respect to stellar populations that do not account for the presence of such systems. The significance of this distinction is evident when we examine star formation history (SFH) models in which star formation has been quenched, respect with models in which star formation is continuous and not quenched. For harder spectra, due to the presence of binaries, the results show the presence of a more extended and hotter HII region, with consequences in the luminosity of the predicted UV and optical emission lines. This also has consequences in the fraction densities of the chemical elements.
With my models, by linking the observed [CII] luminosity with the predicted CIII], [OIII], $H\alpha$ and [NII], I derived a prediction for the CIII]-SFR, [OIII]-SFR, $H\alpha$-SFR and [NII]-SFR relations in the ALPINE sample, analogous to the [CII]-SFR relation already observed in the local Universe (De Looze et al., 2014). Subsequently, I performed a

linear regression to obtain an analytical expression for these relations. These relations found in my Thesis show a linear correlation between the predicted emission luminosity and the observed SFR. The linear relationship between CIII] and SFR, as well as between [NII] and SFR, is more accurately depicted. The correlation coefficients for SB99 and the BPASS model in the CIII]-SFR relation are $r = 0.549$ and $r = 0.563$, respectively. The associated p-values for the two models are $p - value \approx 0.1\%$ and $p - value \approx 0.09\%$. Regarding the [NII]-SFR relation, for the SB99 and BPASS models, $r = 0.689$ and $r = 0.693$, respectively. The associated p-values for the two models are $p - value \approx 0.00033\%$ and $p - value \approx 0.00036\%$. Finally, in my work, I also discussed the expected location of the ALPINE galaxies in the BPT diagram (Baldwin et al., 1981), finding that the ALPINE galaxies, using my predicted optical lines, occupy the position of star-forming galaxies, as expected because the AGN radiation is not implemented in the models. However, in the presence of binaries, this result is more uncertain. Moreover, I find that the BPT diagrams are particularly sensitive not only to the presence of binaries in the stellar population, but also to the star formation history (SFH) and the star formation efficiency (SFE) of the galaxy. This suggests that the BPT diagrams are less reliable in determining the presence of an AGN if we take care of all of these parameters, raising the question of how significant binaries, SFH and SFE are in EoR galaxies and if all these factors can mimic an AGN in a BPT diagram.

Contents

List of Figures

List of Tables

Chapter 1

The Interstellar Medium

The interstellar medium (ISM) is composed of gas, dust, cosmic rays, and radiation between stars. Together with the stars and dark matter, it is one of the main components of a galaxy. Investigating the physical and chemical properties of the ISM is essential to shed light on the process of star formation.

The ISM is made of hydrogen (70%), helium (28%) and metals (2%), namely chemical species with an atomic number greater than that of helium ($Z_e > 2$) (Tielens, 2005). The ISM can be described by characterising the different gas phases that coexist in the galactic environment (see Table 1.1 for details, Haverkorn & Spangler (2013)):

- Molecular clouds.
- Cold Neutral Medium (CNM).
- Warm Neutral Medium (WNM).
- HII regions.
- Warm Ionised Medium (WIM).
- Hot Ionised Medium (HIM).

In *Section 1.1* I will present the main features of all the gas phases composing the ISM of a galaxy with specific attention to the ionised and neutral gas that are the main focus of my Thesis work.

The ISM includes different interstellar objects (Tielens, 2005). In particular, we can observe the following:

- *HII regions*, ionised gas nebular feature formed by the incident radiation of mainly OB stars. OB stars are newly formed stars with a surface temperature that can span from $15000\,\mathrm{K}$ to $30000\,\mathrm{K}$ (Karttunen, 2007).
- *Reflection nebulae*, bluish nebulae that reflect the light of a nearby bright star.
- *Dark nebulae*, clouds characterised by the absence of stars, showing faint optical reflected light.

- *Photodissociation regions* (PDRs), they are the atomic-molecular zones between the ionised and molecular gas near bright luminous OB stars (e.g., surrounding HII regions and reflection nebulae).
- *Supernova remnants* (SNRs), formed by the material ejected by the explosion of massive stars at the end of their life cycle, characterised by the presence of a shock front.

1.1 The phases of the ISM

The phases of the ISM can be distinguished according to their temperature, density, and ionised / molecular fraction, as described in Table 1.1. In what follows, I will discuss them in detail.

Table 1.1: Main Phases of the Interstellar Medium, taken from Haverkorn & Spangler (2013).

Astronomical Name	Density (cm^{-3})	Temperature (K)	Filling Factor
Hot Ionised Medium (HIM)	5×10^{-3}	10^6	50 %
HII regions	5–10	8000	3×10^{-3} %
Warm Neutral Medium (WNM)	0.1–0.5	8000	30 %
Warm Ionised Medium (WIM)	0.1–0.5	8000	25 %
Cold Neutral Medium (CNM)	10–100	~ 100	1%
Molecular Cloud	$200 - \geq 10^5$	≤ 100	0.050 %

1.1.1 The ionised gas phase

The ionised medium can be distinguished in dense HII regions ($n \sim 5 - 10\,\mathrm{cm}^{-3}$), and diffuse ionised gas, which can be divided into warm ($n \sim 0.1 - 0.5\,\mathrm{cm}^{-3}$) and hot ($n \sim 5 \times 10^{-3}\,\mathrm{cm}^{-3}$) phases:

- **Hot ionised medium (HIM)**, mainly produced by shocks generated by supernova explosions (SNe) and super bubbles associated with OB stars. The main tracers of this phase are X-rays, Gamma-rays, and radio synchrotron emissions, caused by relativistic electrons spiralling around magnetic field lines. This gas phase is the raw material from which galactic fountains are generated. The high temperature of gas ($\sim 10^6\,\mathrm{K}$), linked to its high kinetic energy (where $1/2mv^2_{thermal} = k_bT$ Baumjohann (2006)), allows matter to escape from the galactic disc and, after cooling, to fall back to the disc. In Fig.1.1 is visible a representation of galactic fountains.

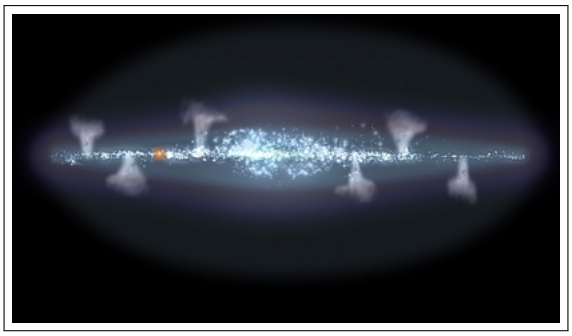

Figure 1.1: Artistic illustration of the Milky Way plane with the galactic fountain scenario: supernovae detonations in the galactic plane heat the interstellar medium and eject hot gas away from the plane, forming galactic fountains that will result in a halo of hot gas around the galaxy. Figure taken from `https://sci.esa.int/web/xmm-newton/-/47989-illustration-of-galactic-fountains`.

- **HII regions** are formed when the intense ultraviolet radiation from OB stars ionises and warms the surrounding gas. HII regions can be used to trace the location of young stars in a galaxy, thus allowing us to indirectly probe star formation (Kennicutt & Evans, 2012). As the optical depth increases, and so the hydrogen column density[1] of the gas increases, we can observe the transition to the neutral phase, which marks the beginning of the photodissociation region (PDR). This happens because photons with energies higher than $13.6\,\mathrm{eV}$ are absorbed in the HII regions, while those with lower energies can penetrate further into the gas and dissociate molecules. In Fig.1.2is reported a representation of an HII region and a PDR from a CLOUDY model of my Thesis (left panel) and a schematic representation from Wolfire et al. (2022) (right panel).

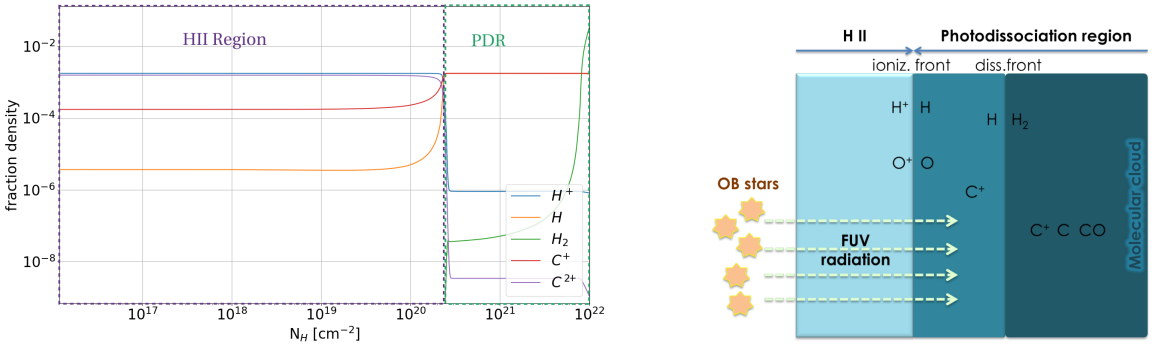

(a) **(b)**

Figure 1.2: *(left panel)* Fraction density of H,H^+,H_2,C^+ and C^{2+} in function of hydrogen column density from a CLOUDY model developed for my Thesis work ($U = -3$, $log(n) = 0.5$ and $Z = 0.15 Z_\odot$). For more information about CLOUDY models, see *Chapter 2*. *(right panel)* A schematic picture of the structure of HII region+PDR, taken from Wolfire et al. (2022).

[1]Hydrogen column density is the number of hydrogen atoms in a cylinder with a $1\,\mathrm{cm}^2$ base area extending from the observer to the source along the line of sight (Karttunen, 2007).

The balance between photoionisation and radiative recombination determines the level of ionisation. The energy that exceeds the ionisation potential of atoms in the HII region is taken away by the photo-electrons as kinetic energy (Tielens, 2005). Typically, ionised regions can be assumed to be spherical around the sources of ionisation and are known as *Strömgren spheres* (Strömgren, 1939), visible in Fig.1.3. By assuming equilibrium between recombination and ionisation, we can calculate the *Strömgren sphere radius*, which is an estimation of the size of HII regions around the sources of ionisation. By assuming a pure hydrogen gas, we indicate with Q_0 the emission rate of hydrogen-ionising photons (i.e. $h\nu > 13.6\,\mathrm{eV}$). Ionised hydrogen extends to a radius of R_S, where the hydrogen density is $n_H = n(H^+)$. The rates of photoionisation and radiative recombination are equal, which gives the steady-state condition for ionisation balance:

$$Q_0 = \frac{4\pi}{3} R_S^3 \alpha n_{H^+} n_e \tag{1.1}$$

where α is the hydrogen recombination coefficient and n_e is the density of free electrons. Since $n_{H^+} = n_e = n_H$, we can solve for the *Strömgren radius*:

$$R_S = (\frac{3Q_0}{4\pi n_H^2 \alpha})^{1/3} \tag{1.2}$$

The size of the HII regions increases as the number of ionising photons (Q_0) increases and the gas density decreases, meaning that there is less material to be ionised by the photons (Draine, 2011). Another way to indicate the intensity of incident radiation that hits the gas is the ionisation parameter U. It is defined as the dimensionless ratio of hydrogen-ionising photons to total-hydrogen densities evaluated at the illuminated face of the cloud:

$$U = \frac{\phi}{n_H c} \tag{1.3}$$

where ϕ is the surface flux of ionising photons at the illuminated face, n_H is the total hydrogen density and c is the speed of light.

- **Warm ionised medium (WIM)**, also known as diffuse ionised gas, is found in external galaxies. It is ionised by a variety of sources, including UV photons that escape HII regions, B stars that are not powerful enough to create HII regions, X-ray binaries, and the extragalactic UV background in the outer parts of the disk or at a considerable distance from the plane. The typical tracers of WIM are UV and optical emission lines, like Hα and high excitation forbidden lines [2], such as [OIII] $5007\,\text{Å}$ (O^+ ionisation energy $35.1\,\mathrm{eV}$). We can also detect radio continuum emission resulting from the collision of ions and free electrons, which produces bremsstrahlung radiation (*Section 1.2.3*).

[2]Forbidden lines have a very small Einstein coefficient A (*Section 1.2*), so in a highly dense environment it is unlikely that these emissions will be visible due to the higher probability of collisional de-excitation. However, the ISM can reach densities so low that collisions become extremely rare, allowing us to observe these types of emission (Tielens, 2005).

Figure 1.3: In figure is visible an image taken with Hubble Telescope (HT) at $H\alpha$ of Rosette Nebula. It is clearly visible the presence of the Stromgren Sphere. The center of the Rosette Nebula host a bright open cluster known as NGC 2244; the blue stars of the cluster emit ultraviolet radiation, which excites the gas of the nebula causing it to emit. Figure from John Corban & the ESA/ESO/NASA Photoshop FITS Liberator.

The ionised gas phase of the ISM can be traced by pulsar signals, ultraviolet (UV) and optical line emissions, and the $H\alpha\,6563\,\text{Å}$ recombination line. Hydrogen first ionisation energy corresponds to $13.6\,\text{eV}$. Neutral hydrogen can be ionised through two main processes: photo-ionisation and collisional ionisation. The former process (*Section 1.3.1*) involves the ionisation of hydrogen atoms through photons emitted by sources that are capable of continuously producing photons with $h\nu >= 13.6\text{eV}$. The ionising medium can only persist if it is supplied with a continuous flow of energy to keep the matter ionised. Otherwise, the gas will begin to cool down due to radiative cooling (*Section 1.2.1*). The ionisation sources have to produce extreme ultraviolet (EUV) photons that have an energy in the range $13.6 - 150\,\text{eV}$. The main sources capable of producing these photons are young and hot OB stars (surface temperature between $1.5 \times 10^4\,\text{K}$ and $3 \times 10^4\,\text{K}$ (Karttunen, 2007)) and Active Galactic Nuclei (AGN). Collisional ionisation is instead the process through which an electron is taken away from an atom or molecule by collision with another particle, for example, an electron, ion, or photon. The production of free electrons results from photoionisation, and as the number of ionising photons increases, the number of free electrons also increases, leading to an increase in collisional ionisation.

1.1.2 The neutral gas phase

The neutral medium can be divided into two main phases:

- **warm neutral medium (WNM)**, $T \sim 8000\,\text{K}$ and $n \sim 0.1 - 0.5\,\text{cm}^{-3}$.
- **cold neutral medium (CNM)**, $T \sim 100\,\text{K}$ and $n \sim 10 - 100\,\text{cm}^{-3}$.

The neutral gas is organised in HI clouds and warm inter-cloud gas, forming the first part of PDR. The main heating process that produces HI clouds is the photoelectric effect on dust grains (*Section 1.3.2*). This is the phenomenon of electrons being released when photons strike a material. These electrons that are emitted are called photoelectrons. The primary tracers and coolers of this gas phase are the $21\,\text{cm}$ hydrogen emission line and the [CII] $158\,\mu\text{m}$ emission line (radiative cooling, *Section 1.2.1*). The hyperfine structure line at $21\,\text{cm}$ of neutral hydrogen is caused by the combination of the electronic

angular momentum and the spin of the nucleus, which creates a magnetic field. The emission from individual clouds is exceptionally rare, with an Einstein factor (*Section 1.2*) of $\sim 10^{-15}\,\mathrm{s}^{-1}$, and is in competition with collisional de-excitation. We can only trace it when there is a high HI mass and low density, which is present in the neutral medium of the interstellar medium (ISM), as presented in Table 1.1.

A fraction of the neutral gas phase of the ISM resides in so-called **Photodissociation Regions (PDRs)**. These are patches of the ISM where the chemical and physical properties of the gas are influenced by the presence of far ultraviolet photons (FUV, $6 < h\nu < 13.6\,\mathrm{eV}$) with energies below the Lyman limit (Tielens, 2005). In a PDR the hydrogen is mostly neutral while metals with ionisation potential $< 13.6\,\mathrm{eV}$ (e.g. carbon) are ionised. A traditional PDR model involves FUV radiation emitted by OB stars penetrating beyond the HII region and being absorbed by an adjacent molecular cloud (Wolfire et al., 2022; Hernández-Vera et al., 2023). However, it is also possible to find PDRs in reflection nebulae, on the surfaces of pillars and globules, in embedded protostars and protostellar and protoplanetary disks (Wolfire et al., 2022). The FUV radiation is absorbed by the dust grains present in the PDR, and are re-emitted as infrared continuum (a phenomenon called dust extinction[3]). A portion of FUV radiation is also responsible for heating the gas due to the photoelectric effect (*Section 1.3.2*) on small grains and large molecules. In a PDR, molecules are photodissociated by FUV radiation (as seen in Figure 1.2, the density of H_2 molecules begins to increase within the PDR).

As can be seen in Figure 1.2, when the transition from HII region to PDR occurs, there is an increase in the amount of neutral hydrogen that is followed by an increase of ionised carbon. The [CII] emission (see *Section* 1.2) is the main source of line cooling, while the integrated Far-Infrared (FIR) dust emission is the primary source of continuum cooling in the Photodissociation Region (PDR). The [CII] emission is a measure of the incident FUV radiation, because of the equilibrium between the gas cooling processes caused mainly by the [CII] emission and the heating processes caused by FUV radiation (see *Sections* 1.2 and 1.3).

1.1.3 The molecular gas phase

The densest phase of ISM is the molecular gas, which often forms gravitationally bound clouds called Giant Molecular Clouds (GMCs). The GMCs are mainly made up of cold gas and dust, and are areas where FUV photons are unable to penetrate (due to

[3]Extinction is the term used to describe the removal of photons from a beam of light as it passes through a medium. It is the combination of absorption and scattering of the photons. We know from the radiative transfer equation (*Chapter 2*) that the change of intensity is proportional to the distance travelled and the medium density:

$$dI_\nu = -k_\nu \rho I_\nu ds \tag{1.4}$$

where k_ν is the extinction coefficient or opacity per unit mass $[cm^2/gr]$. The optical depth of the gas is related to the extinction coefficient by the relation $\tau = \int k_\nu \rho \nu ds$. The relation between the optical depth and extinction parameter A_ν, that indicates the change of magnitude due to extinction, is:

$$A_\nu = 1.086\tau_\nu \tag{1.5}$$

a shielding effect[4]). Hence, hydrogen is found in the molecular state. GMCs are also classified by their hydrogen column density, with $N_H \gtrsim 10^{22}\,\mathrm{cm}^{-2}$ (Froebrich & Rowles, 2010). The typical mass of a GMC is $10^5 - 10^6\,\mathrm{M}_\odot$ and the typical size is $5 - 200\,\mathrm{pc}$. Molecular hydrogen is often traced indirectly through the detection of rotational transitions of carbon monoxide (CO), such as the CO J=1-0 transition at $2.6\,\mathrm{mm}$. Molecular hydrogen (H_2), dominating the mass of the molecular gas, does not have a dipole moment, and the quadrupole transitions require high temperatures ($T = 500 - 2000\mathrm{K}$), only present in particular conditions in molecular clouds (e.g. if the gas is shock-heated). We can use carbon monoxide emission because it is abundant in PDR, it is present in the cold molecular phase ($5.5\,\mathrm{K}$) and the CO(1-0) line has almost the same critical density (see *Section1.2* for the definition of critical density) of molecular hydrogen ($n \sim 10^3\,\mathrm{cm}^{-3}$).

The primary source of heating in GMCs are the cosmic rays, which are high-energy electrons and completely ionised nuclei of atoms that come from all directions in equal amounts (*Section 1.3.3*), and X-ray photons that can be emitted either from the accretion of gas onto the central black hole in a galaxy (AGN), or by X-ray binary stars. The FUV photons are few as a result of the shielding effect phenomena. GMCs are characterised by significant dust thermal continuum emission in the infrared/submillimeter range, which is expressed by a modified black body (MBB) equation (Bianchi, 2013):

$$S_{\nu\ observed} = \Omega[B_\nu(T_d) - B_\nu(T_{CMB})](1 - e^{-\tau_\nu})(1+z)^{-3}\ [\mathrm{erg\,cm}^{-2}] \tag{1.6}$$

where S is the flux, Ω the solid angle, B the Plank function[5], τ the optical depth and z the redshift.

1.2 Cooling processes

In what follows, I will discuss the main cooling processes taking place in the different gas phases of the ISM. In particular, any process of cooling involves the conversion of the kinetic energy of particles into radiation that is emitted without being reabsorbed. The main cooling channels are the following:

- **Radiative cooling**, through collisional excitation of metal fine structure lines (e.g. [CII], [OIII]), hydrogen and helium excitation, ionisation and recombination.
- **Electronic recombination on dust grains**.
- **Bremsstrahlung continuum emission**.
- **Dust continuum emission in the infrared band**.

[4]When the FUV absorption lines become optically thick, the FUV pumping (excitation to higher bounds level) and dissociation rates rapidly drop with increasing H_2 column density. This optical depth effect is known as H_2 self-shielding and is an essential part of H_2 chemistry (Wolfire et al., 2022).

[5]$B(\nu,T) = \frac{2h\nu^3}{c^2}\frac{1}{\exp\left(\frac{h\nu}{k_\mathrm{B}T}\right)-1}$

1.2.1 Radiative Cooling

Radiative cooling is the process by which hot gases in space lose heat by emitting electromagnetic radiation. Radiative cooling rate depends on the temperature, density, and composition of the gas. To analyse radiative cooling, we can use a simplified version of an atom, called a two-level atom. Consider an atom with only two energy levels: a lower energy level l and an upper energy level u. We can divide the processes that cause the transfer of electrons between two energy levels into two categories: excitation processes and de-excitation processes (Tielens, 2005):

- **Excitation**
  - **Collision** of an atom with a more energetic particle, that results in a transfer of kinetic energy.
  - **Absorption** of a photon with energy corresponding to $h\nu_{ul}$.
- **De-excitation**
  - **Collision** with other less energetic particle, that results in kinetic energy transfer from the atom to the hitting particle.
  - **Spontaneous emission** of a photon with energy $h\nu_{ul}$.
  - **Stimulated emission** of a photon with energy $h\nu_{ul}$, stimulated by another photon.

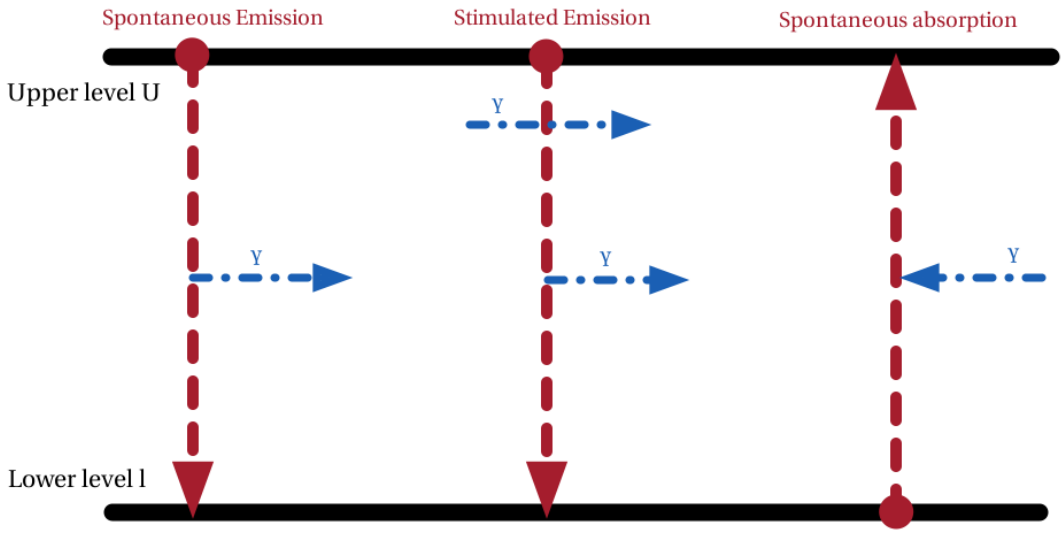

Figure 1.4: Schematic representation of emission and absorption processes.

We can write the *statistical equilibrium equation*, which imposes the equilibrium between the excitation and de-excitation:

$$n_l n_{coll} \gamma_{lu} + n_l B_{lu} J_\nu = n_u n_{coll} \gamma_{ul} + n_u A_{ul} + n_u B_{ul} J_\nu \tag{1.7}$$

where n_l (n_u) is the number density of atoms in the lower (upper) level, n_{coll} is the number density of the collision partner (usually electrons or neutral hydrogen atoms).

The γ_{lu} (γ_{ul}) is the collisional excitation coefficient (deexcitation) that can be expressed as:

$$\gamma \sim \langle \sigma v \rangle \tag{1.8}$$

where σ is the collision cross section of the colliders and v the velocity of the particles. B_{lu} is the Einstein coefficient corresponding to absorption, A_{ul} and B_{ul} are the Einstein coefficients, respectively, for spontaneous and stimulated emission, and J_ν is the intensity of the radiation field at the frequency ν corresponding to the line energy.

The inverse of A_{ul} is a measurement of the probability that a certain spontaneous emission can occur. The Einstein coefficient A_{ul} is defined in terms of the total rate of spontaneous emission W_{ul} for a system of N_u atoms in the upper level:

$$W_{ul} = A_{ul} N_u \tag{1.9}$$

The B_{ul} (B_{lu}) coefficients are defined in terms of the transition rates for induced absorption W_{lu} and induced/stimulated emission W_{ul}:

$$W_{lu} = B_{lu} r_w N_l \tag{1.10}$$

$$W_{ul} = B_{ul} r_w N_u \tag{1.11}$$

where r_w is the energy density per unit of angular frequency interval. The Einstein coefficients are connected to each other by the following equations:

$$A_{ul} = \frac{2h\nu^3}{c^2} B_{ul} \tag{1.12}$$

$$g_l B_{lu} = g_u B_{ul} \tag{1.13}$$

where g_l and g_u are the degeneracies (also called multiplicities) of the two energy levels, defined by quantum mechanics. The probability given by the Einstein coefficient for spontaneous emission A_{ul} is the transition probability. In the dipole approximation[6], this coefficient is proportional to:

$$A_{ul} \sim \mu^2 \sim \nu^3 \tag{1.14}$$

where μ is the dipole momentum of the transition and ν is the frequency of the transition. It can be said that transitions with a high frequency (which is equivalent to a high energy, recall $E = h\nu$) generally occur more quickly when they are allowed (Hilborn, 2002).

[6]The dipole approximation is a simplifying assumption used in physics to model the behaviour of charged systems. It is based on the idea that the electric field generated by a system of charges can be approximated as the field of a single dipole at large distances from the system.

A gas is in a state of local thermodynamic equilibrium (LTE) when the collisions in the medium occur so often that the level populations are thermalised, meaning they follow a Boltzmann distribution that is only dependent on temperature. Therefore, given a chemical species with density n, we find that the number of atoms n_i at the energy level i is:

$$n_i = \frac{g_i n}{Q(T)} \exp\left(-\frac{E_i}{kT}\right) \tag{1.15}$$

where Q is the partition function[7], g_i is the degeneracy of the i-level, k is the Boltzman constant and E_i is the i-level energy (Tielens, 2005). Hence, when the radiative de-excitation is negligible and there is no external radiative field, the statistical equilibrium equation becomes:

$$n_l \gamma_{lu} = n_u \gamma_{ul} \tag{1.16}$$

Substituting to n_u and n_l the corresponding Boltzmann distribution given by Eq.1.15, we obtain the detailed balance equation of collisional coefficients:

$$\gamma_{ul} = \gamma_{lu} \frac{g_l}{g_u} \exp\left(-\frac{E_u - E_l}{kT}\right) \tag{1.17}$$

In non-LTE and non-external radiative field case, the statistical equilibrium equation (Eq.1.7) becomes:

$$n_l n_{coll} \gamma_{lu} = n_u n_{coll} \gamma_{ul} + n_u A_{ul} \tag{1.18}$$

and by substituting the relation between the collisional coefficients, Eq.1.17, we obtain:

$$\frac{n_u}{n_l} = \frac{g_u}{g_l} \exp\left(-\frac{(E_u - E_l)}{kT}\right) \frac{1}{1 + \frac{n_{crit}}{n_{coll}}} \tag{1.19}$$

The Eq.1.19 introduces the *critical density* (n_{crit}), which is determined by the spontaneous emission Einstein coefficient A_{ul} and the collision parameter γ_{ul}:

$$n_{crit} = \frac{A_{ul}}{\gamma_{ul}} \tag{1.20}$$

The critical density is a significant factor in determining the behaviour of a single emission line in a gas medium (Tielens, 2005). More precisely, in a certain gas for a certain chemical species, we can have two different scenarios:

- $n > n_{crit}$: collisions are the main factor in the population distribution of energy levels, which means that we are in a state of local thermodynamic equilibrium. This means that the population of energy levels is determined by a Boltzmann distribution, and hence the levels with the highest probability are those that are thermally populated.

[7]The partition function is a function of the temperature T that describes the statistical properties of a system in thermodynamic equilibrium. It is defined as the sum of all possible microstates of the system. Mathematically, the partition function is:

$$Q(T) = \sum_i e^{-\beta E_i}$$

where i is the index of a microstate, E_i is the energy of microstate i, $\beta = \frac{1}{kT}$.

- $n < n_{crit}$: the energy levels are de-excited by radiation rather than collisions. Consequently, the levels depend on both n and T and are subthermally populated.

In the non-LTE case, but with the presence of an external black body radiation field (e.g. stellar population) and in case we can neglect collisions (i.e. in a low-density environment) the statistical equilibrium equation becomes:

$$n_l B_{lu} J_{BB} = n_u A_{ul} + n_u B_{ul} J_{BB} \tag{1.21}$$

where J_{BB} is the Plank function. The equation gives the following density distribution for a certain energy level i:

$$n_i = \frac{g_i n_x}{Q(T)} \exp\left(-\frac{E_i}{kT_{rad}}\right) \tag{1.22}$$

where T_{rad} is the temperature associated with the incident radiation. In this case, the excitation and de-excitation mechanisms are dominated by the radiation field. The level population is again described by a Boltzmann function, but depending on the source radiation temperature T_{rad}.

After the introduction of the two-level system in *Section 1.2.1*, now we can define the so-called cooling rate equation. In general, in the absence of background radiation, the cooling rate of the gas is as follows:

$$n^2 \Lambda = n x_i \frac{(g_u/g_l) e^{-E_{ul}/k_b T} A_{ul} E_{ul} \beta_{esc}(\tau_{lu})}{((g_u/g_l) e^{-E_{ul}/k_b T} + 1) + A_{ul} \beta_{esc}(\tau_{lu})/n\gamma_{ul}} \tag{1.23}$$

where x_i is the fractional abundance of the species i, g_u and g_l are the statistical weights of the upper and lower states of line transition, E_{ul} is the energy of the transition, k_b is the Boltzmann constant, T is the gas temperature, A_{ul} is the Einstein coefficient between the two energetic levels u and l, $\beta_{esc}(\tau_{lu})$ is the escape probability[8], τ_{lu} is the optical depth in the line, and γ_{ul} is the rate coefficient for collisional de-excitation (Wolfire et al., 2022).

[8]The chance of a photon to escape from the gas is denoted by β and varies between 0 and 1, depending solely on the geometry and optical depth of the material. The escape probability formalism supposes that the radiation field of the medium in the equation of statistical equilibrium can be expressed as:

$$J_\nu = S_\nu(1 - \beta)$$

where S_ν is the source function. If $\beta = 0$, no photons will be able to leave the medium. On the other hand, if $\beta = 1$, all photons will be able to escape from the medium. So we can write the critical density as:

$$n_{crit} = \beta \cdot \frac{A_{ul}}{\gamma_{ul}}$$

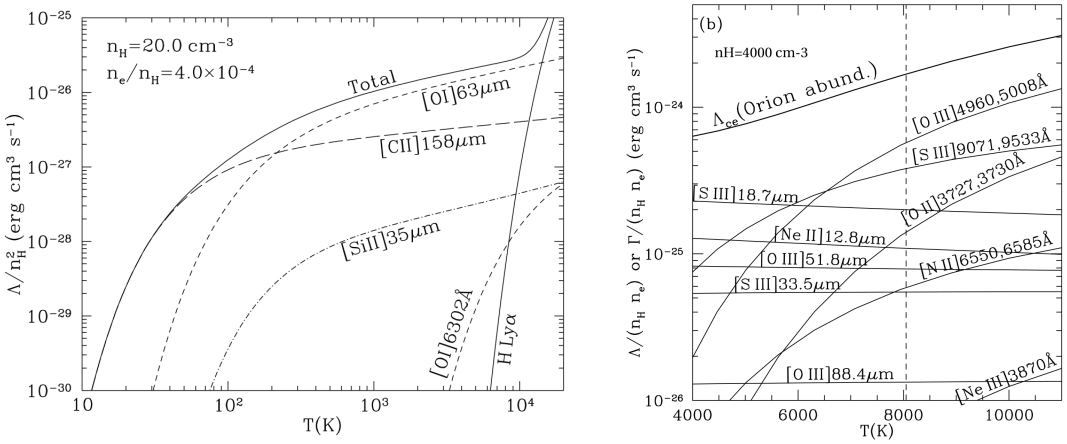

(a) **(b)**

Figure 1.5: Cooling function for some emission lines in HI regions (left panel) and HII regions (right panel), taken from Draine (2011).

In Figure 1.5, we observe some important emission lines associated with radiative cooling in HI regions (and thus PDRs) and HII regions. The plots illustrate that the cooling rate of each line is highly dependent on the temperature of the gas. In fact, to emit a significant amount of radiation through a given emission line, a certain chemical has to be found in an environment with a high enough temperature. A clear example is the hydrogen Lyman α emission visible in Figure 1.5 (left panel): at a temperature lower than $10000\,\mathrm{K}$, when the hydrogen becomes neutral, we have a cutoff in the cooling rate of the $Ly\alpha$ line, because all hydrogen starts to be in the energy ground state.

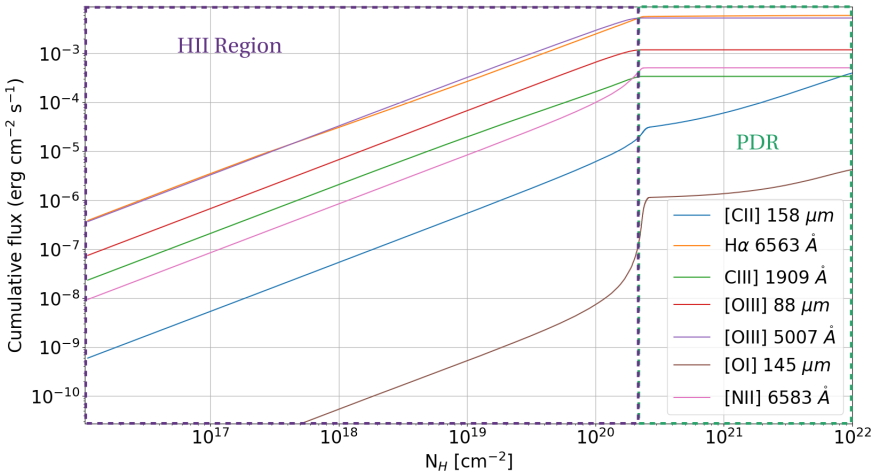

Figure 1.6: Cumulative flux of emission lines in function of hydrogen column density N_H. It is evident that the emission lines of Hα $6563\,\mathring{A}$, CIII] $1909\,\mathring{A}$, [OIII] $5007\,\mathring{A}$, [OIII] $88\,\mu$m and [NII] $6583\,\mathring{A}$ reach their highest flux at the edge of HII regions, making them good tracers of the ionised phase. Viceversa, we observe an increase in the emission of [CII] $158\,\mu$m and [OI] $145\,\mu$m entering the PDR, and it begins to plateau at the edge of the simulated cloud (around $N_H \approx 10^{22}\,\mathrm{cm}^{-2}$).

The [CII] fine structure transition ${}^2P_{3/2} \rightarrow {}^2P_{1/2}$ (at $158\mu\mathrm{m}$) is an important radiative cooling line for PDRs. It is a crucial tracer of the PDR, (Tielens, 2005; Wolfire et al., 2022), because the C^0 ionisation potential is $11.26\,\mathrm{eV}$ (i.e. below the Lyman limit of $13.6\,\mathrm{eV}$). For this reason, [CII] emission starts to become relevant in the warm and cold neutral ISM and in PDRs, as visible in Fig.1.6, where far ultraviolet (FUV, $6 - 13.6\,\mathrm{eV}$) radiation escapes the HII regions surrounding hot OB stars.

UV and optical lines as CIII] $1909\,\mathrm{\AA}$, [OIII] $5007\,\mathrm{\AA}$ and [NII] $6583\,\mathrm{\AA}$ are important radiative coolers in HII regions. The CIII] $1909\,\mathrm{\AA}$ line (C^+ ionisation energy $24.45\,\mathrm{eV}$) is an important ionised gas tracer for two main reasons. First, being a carbon line, it is not affected by uncertainties in the C vs O abundance when compared to the [CII] $158\,\mu\mathrm{m}$ trace of the neutral gas. Second, CIII] is the brightest line in the UV rest frame. This couple of emission lines from the same chemical element can describe two different ISM phases: the ionised one characterising the HII regions and the neutral one characterising the PDRs (Le Fèvre et al., 2019).

The [OIII] $5007\,\mathrm{\AA}$ emission line is a forbidden oxygen line emitted by a gas that is highly ionised (the O^+ ionisation energy is $35.1\,\mathrm{eV}$). It is one of the brightest emission lines in the optical spectrum of AGNs and star-forming galaxies. This line is used to measure the mass of the central black hole in an AGN (Wang et al., 2011) and can also be used to study the evolution of galaxies. In star-forming galaxies, the [OIII] emission line is typically narrow and symmetric. However, in AGNs, the line can be broad and asymmetric, indicating that the gas is being turbulently stirred by the black hole's outflow (Harrison et al., 2014).

The [NII] $6583\,\mathrm{\AA}$ emission line is a forbidden nitrogen line that is emitted by a highly ionised gas (the N^0 ionisation energy is $29.6\,\mathrm{eV}$). Furthermore, this line is one of the brightest in the optical spectrum of AGNs and star-forming galaxies (Hamann & Barlow, 1997). The [NII] can be used to measure the electron density in the gas around an AGN or in regions forming stars. This is because the ratio of the intensities of the emission lines [NII] $6583\,\mathrm{\AA}$ and [NII] $6548\,\mathrm{\AA}$ depends on the electron density. The higher the electron density, the more collisional excitation of the [NII] atoms will occur, and the stronger the $6583\,\mathrm{\AA}$ emission line will be relative to the $6548\mathrm{\AA}$ emission line. The [NII] emission line can also be used to study the evolution of galaxies. In star-forming galaxies, [NII] is typically weak, but it can become stronger in AGNs. This is because the line is sensitive to the presence of high-energy photons (Osterbrock & Ferland, 2006).

1.2.2 Electronic recombination on dust grains

Dust particles act as a repository of gas energy. If the thermal energy of electrons that recombine on grains is greater than that of electrons ejected from the grain surface, then the gas will experience net cooling. The cooling rate due to the electron recombination on the dust grains (Λ_{gr}) is proportional to $x \equiv G_0 T^{1/2}/n_e$:

$$n_H^2 \Lambda_{gr} = 4.65 \times 10^{-30} T^{0.94} (G_0 T^{1/2}/n_e)^{\beta} n_e n_H \;\; [\mathrm{erg\,cm^{-3}\,s^{-1}}] \tag{1.24}$$

where $\beta = 0.74/T^{0.068}$ (Tielens, 2005) and G_0 is the Habing unit ($G_0 = 1.6{\times}10^{-3}\,[\mathrm{erg\,s^{-1}\,cm^{-2}}]$, Habing (1968)).

1.2.3 Bremsstrahlung emission

Radiation produced by the acceleration of a charge in the electric field of another charge is called bremsstrahlung, or free-free emission. For small-angle scatterings, the emission from a single collision between an electron and an ion is:

$$\frac{dW(b)}{d\omega} = \frac{8Z^2e^6}{3\pi c^3 m^2 v^2 b^2} \quad b << v/\omega \quad [\text{energy} \cdot \text{time}] \tag{1.25}$$

where Ze is the ion charge, b is the impact parameter, v is the free-electron impact velocity, m is the ion mass, ω is the dipole frequency and $W(b)$ is the total energy emitted (Rybicki & Lightman, 2004).

1.2.4 Dust continuum emission in the infrared band

The hitting radiation passing through the gas is partially absorbed by dust and re-emitted at higher wavelengths. Dust grains emit as a grey body and, as shown in Bianchi (2013), a reasonable estimate of the dust temperature can be obtained by assuming that the dust emits as a single grey body:

$$I_\nu = B_{Black\,Body}(\nu)(1 - e^{-\tau}) \tag{1.26}$$

This is the Modified Black Body equation, where the optical depth τ is dependent on a parameter β that modified the shape of a pure black body emission:

$$\tau = \left(\frac{\nu}{\nu_0}\right)^\beta \tag{1.27}$$

1.3 Heating processes

In this section, I will instead present the major heating channels of the different gas phases in the ISM:

- **photoionisation heating**.
- **photoelectric heating**.
- **cosmic-ray heating**.

1.3.1 Photoionisation heating

Photoionisation is the main heating mechanism in the case of ionised gas (e.g. HII regions). It is the process by which a photon is taken by an atom (or molecule) when the energy of the photon is greater than the energy of ionisation of the chemical species. This process requires a photon with energy that is at least equal to the ionisation potential. As a result, an electron is ejected. More in detail, if the upper state of the atom lies in the continuum, there can be absorption in a continuous range of frequencies, and this absorption results in the ejection of an electron from the atom (Rybicki & Lightman, 2004). If the energy of the incident photons is $h\nu_0$ and the photoionisation cross-section

is σ_ν, we have that the number of ionising photons per unit volume and per unit time is:

$$N = 4\pi n_a \int_{\nu_0}^{\infty} \frac{\sigma_\nu J_\nu}{h\nu} d\nu \tag{1.28}$$

where n_a is the number density of atoms and J_ν is the flux per unit of frequency.

1.3.2 Photoelectric heating

Photoelectric heating is the main heating process in the case of neutral gas (e.g. PDRs). It is driven by collisions between the gas and the fast-ejected electrons, resulting in the photoelectric effect (PE) on dust grain. The PE occurs when a photon, absorbed by the dust grain, causes the emission of an electron from the dust, which in turn heats the gas. The resulting energy of the emitted electron is $E_e = h\nu - W$, where $h\nu$ is the energy of the hitting photon and W is the work necessary to extract an electron from the grain.

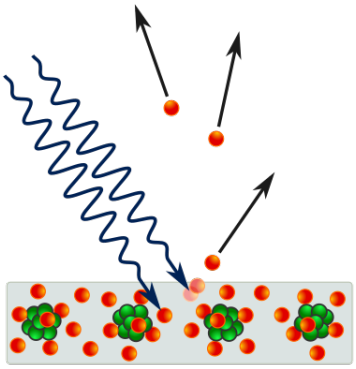

Figure 1.7: Representation of the photoelectric effect, image taken from `https://en.wikipedia.org/wiki/Photoelectric_effect`

The photoelectric heating rate can be written as follows:

$$n\Gamma = 10^{-24} n G \epsilon \; [\mathrm{erg\,cm^{-3}\,s^{-1}}] \tag{1.29}$$

where n is the hydrogen density, Γ is the heating rate per hydrogen atom in $erg\,s^{-1}$, G is a measure of the integrated far-ultraviolet (FUV) radiation field in Habing units ($G_0 = 1.6 \times 10^{-3}\,[\mathrm{erg\,s^{-1}\,cm^{-2}}]$, Habing (1968)), and ϵ is the photoelectric heating efficiency (Wolfire et al., 2022). The efficiency of this process depends mainly on the dimension of dust grains and polycyclic aromatic hydrocarbons (PAH): the larger the grain, the more probable the electron is reabsorbed by the grain. The efficiency rate ϵ can be expressed as (Wolfire et al., 2022):

$$\varepsilon = \frac{4.87 \times 10^{-2}}{1.0 + 4 \times 10^{-3} \gamma^{0.73}} + \frac{3.65 \times 10^{-2} (T/10^4)^{0.7}}{1 + 2 \times 10^{-2} \gamma} \tag{1.30}$$

where γ is the gamma parameter[9].

1.3.3 Cosmic-ray heating

The cosmic-ray heating is the main heating process within molecular clouds. Cosmic rays (CRs) are energetic charged particles with a high percentage of nuclei and a small fraction of electrons. In Figure 1.8 the typical energy spectrum of the CRs is shown as the result of different experiments.

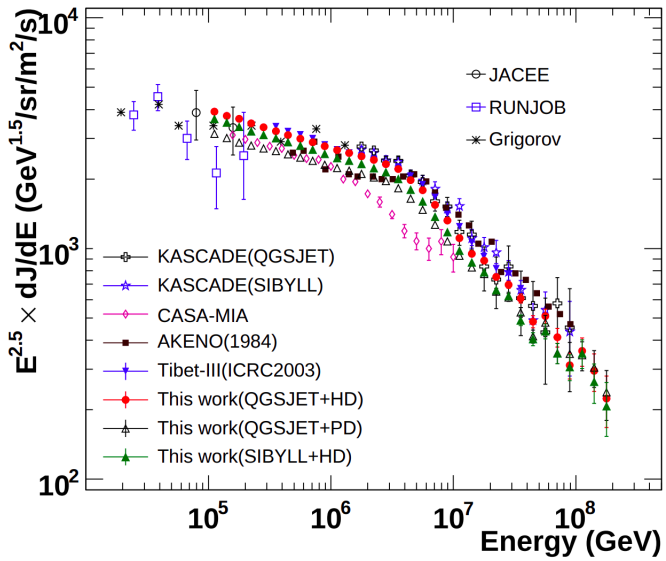

Figure 1.8: Energy distribution of cosmic rays. Figure taken from Amenomori et al. (2008).

CR particles can be generated from a variety of sources, including supernova explosions, stellar winds, and AGN accretion. The role cosmic rays play in heating gas is significant when the gas is sufficiently shielded from the interstellar radiation field. In this instance, the photoelectric effect is not as significant because there are no photons present to generate photoelectrons. Cosmic rays transfer kinetic energy to atoms through collisions, hence heating the gas (Wolfire et al., 2022).

1.4 ISM observations in high-z galaxies

Characterisation of the ISM in the Early Universe is a challenging task both from an observational and theoretical perspective. Understanding the ISM properties in the high-z galaxies is crucial to clarify the impact of these galaxies on the reionisation process during the Epoch of Reionisation (EoR), due to the strict connection between star formation (SF) and gas properties. EoR is a crucial era in cosmic history ($6 < z < 30$),

[9]The gamma parameter, also referred to as the shape parameter, is one of two parameters that define the gamma distribution. It is a positive real number that influences the shape of the distribution. A higher gamma parameter will lead to a distribution with a longer tail. The gamma distribution is a continuous probability distribution that is often used to model the time it takes for a certain event to take place (Hogg, 1978).

where the Universe has been reionised by ionising photons emitted on the surface of the first stars and escaped from the first galaxies. These EoR galaxies are the first formed in our Universe after the collapse of gas clouds at the end of the dark age (Coles & Lucchin, 2002). In the last years, the Atacama Large Millimetre Array (ALMA) has revolutionised the study of the neutral and molecular gas phases traced by far-infrared (FIR) emission lines. Recently, the launch of the James Webb Space Telescope (JWST) is making it possible to study the ionised gas phase traced by optical and ultraviolet (UV) nebular emission lines. The main issues with EoR galaxies observations stem from the technical challenges in detecting different gas tracers (e.g. nebular emission lines from the ionised gas, or far-infrared lines from the cold neutral/molecular gas) at sufficiently high spatial resolution and sensitivity.

1.4.1 Observations of neutral gas with ALMA

ALMA is a ground-based radio interferometer[10] operating in the wavelength range $0.3-9.6\,\mathrm{mm}$ (Wootten & Thompson, 2009). In the past ten years, ALMA allowed [CII] at $158\,\mu\mathrm{m}$ detection in high-z galaxies (e.g. Maiolino et al. (2015); Carniani et al. (2018); Béthermin et al. (2020); Bouwens et al. (2022)). [CII] is a crucial tracer of the PDRs (*Section* 1.2). The [CII] radiation has been found to correlate with gas mass at $1 < z < 6$ (Zanella et al., 2018). Moreover, the balance between the cooling provided by [CII] and the heating provided by star formation makes it a valuable tool for investigating the star formation activity within galaxies (Wolfire et al., 2022). The connection between [CII] and SFR has been studied for different galaxy populations. At redshift $z = 0$, De Looze et al. (2014) first established the [CII]-SFR relation for local starburst galaxies:

$$\log(\mathrm{SFR}/[\mathrm{M}_\odot\,\mathrm{yr}^{-1}]) = (1.00 \pm 0.04)\log(\mathrm{L}_{[\mathrm{CII}]}/\mathrm{L}_\odot) + (-7.06 \pm 0.33) \tag{1.31}$$

this relationship seems to hold also for high-z systems, as revealed by ALMA up to $z = 7$ (Schaerer et al., 2020) in the ALMA Large Program to Investigate [CII] at Early Times (ALPINE) sample:

$$\log(L_{[\mathrm{CII}]}/\mathrm{L}_\odot) = (1.00 \pm 0.12)\log(\mathrm{SFR}/[\mathrm{M}_\odot\,\mathrm{yr}^{-1}]) + (7.03 \pm 0.17) \tag{1.32}$$

ALPINE is a 70 hours survey (*PI: Le Fèvre*) that measured the far-infrared properties of 118 galaxies in the Early Universe at redshift $4 < z < 6$ (Faisst et al., 2020; Béthermin et al., 2020; Fujimoto et al., 2020; Le Fèvre et al., 2020). Among the 118 galaxies, 75 galaxies were detected in [CII] and over the last 3 years many results based on the ALMA data have been presented (e.g. Béthermin et al. (2020); Gruppioni et al. (2020); Loiacono et al. (2021); Pozzi et al. (2021)). The [CII] detections allowed, for example, a characterisation of the cold interstellar medium in the sample, the study of the gas mass and of the [CII]-SFR relation (e.g. Béthermin et al. (2020); Schaerer et al. (2020); Dessauges-Zavadsky et al. (2020)). The ALPINE main goal has been to gain a deeper understanding of the galaxy evolution at the end of the EoR. An important result found thanks to ALPINE data is the discovery of a continuous decline of the

[10] An interferometer is an array of radio antennas which operate together by observing the same object at the same time, and by correlating the signals detected by the different dishes. This results in an amplification of the sensitivity that single radio telescopes would achieve, and also a better spatial resolution.

molecular gas depletion timescale from $z = 0$ to $z = 5.9$, which reaches a mean value at $z \sim 5.5$, suggesting a slight enhancement of star formation efficiency towards high redshifts (Dessauges-Zavadsky et al., 2020). Furthermore, the ALPINE data are the first to sample the faint end of the infrared luminosity function (LF), showing little evolution from $z \approx 2.5$ to $z \approx 6$, and a flat slope up to the highest redshifts (i.e. $4.5 < z < 6$) (Gruppioni et al., 2020).

Another relevant ALMA survey focused on the high-z Universe is the Reionization Era Bright Emission Line Survey (REBELS, *PI: Bouwens*), a 70-hours ALMA large programme that observed 40 galaxies at $6.5 < z < 9.5$, scanning for either the $157.7\mu m$ [CII] and the $88.4\mu m$ [OIII] lines (Bouwens et al., 2022). REBELS data show that star-forming galaxies, on average, show no evolution in the size of the [CII] emitting regions between $z \sim 7$ and $z \sim 4$, suggesting that star-forming galaxies could be morphologically dominated by gas over a wide redshift range (Fudamoto et al., 2022). Moreover, REBELS permit to compute the specific star formation rate (sSFR) associated to galaxies in the EoR, showing that sSFRs increase rapidly toward higher redshifts for massive galaxies, evolving as $(1 + z) \cdot (1.7 \pm 0.3)$, broadly consistent with expectations from the evolving baryon accretion rates (Topping et al., 2022).

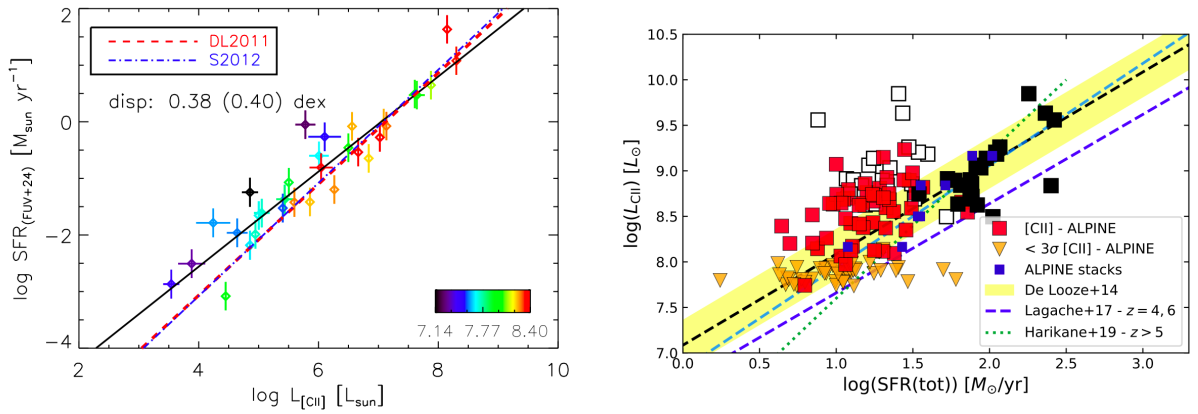

(a) **(b)**

Figure 1.9: (left panel) Relation between the SFR and [CII] luminosity on global galaxy scales, for local galaxies. Galaxies are color-coded according to metallicity with increasing oxygen abundances going from black over blue, green and yellow to red colors. The best fitting SFR calibration is presented as a solid, black line. Figure taken from De Looze et al. (2014). (right panel) [CII] as a function of UV or UV+IR-derived SFR for the $z \sim 5$ ALPINE sources. Squares show the [CII] detections, orange triangles the 3σ upper limits. Black squares show galaxies with continuum detection (black filled squares show SFR(UV)+SFR(IR), empty squares the SFR(UV) of the same sources); red squares shows the SFR(UV) for the other (non-continuum-detected) ALPINE sources. Blue circles show the results from stacks of ALPINE sources in four bins of L([CII]) and two redshift bins. Figure taken from Schaerer et al. (2020).

1.4.2 Observations of ionised gas with JWST

The launch, in 2022, of the JWST opened a further, and entirely new, window on the rest-frame optical/UV emission lines tracing the ionised gas in high-z galaxies. JWST is

an infrared telescope with a $\approx 6.5\,\mathrm{m}$ primary mirror, equipped with four instruments, including cameras and spectrometers, capable of detecting extremely faint signals from the early galaxies in our Universe. The four equipped instruments are (Gardner et al., 2006):

- **Near InfraRed Spectrograph (NIRSpec)**,designed to operate within the wavelength range of $0.6 - 5\,\mu\mathrm{m}$. Thanks to its specialised technological construction, NIRSpec can simultaneously obtain 100 spectra during an observation.
- **Mid-Infrared Instrument (MIRI)**, which sees light in the mid-infrared region of the electromagnetic spectrum. MIRI covers the wavelength range of $5 - 28\,\mu\mathrm{m}$.
- **Near Infrared Camera (NIRCam)**, is the primary imager that covers the infrared wavelength range 0.6 to 5 microns.
- **Fine Guidance Sensor (FGS)**, which allows the telescope to be orientated precisely so that it can obtain high-quality images. The Near-Infrared Imager and Slitless Spectrograph part of the FGS/NIRISS are used to investigate the following science objectives: first-light detection, exoplanet detection and characterisation, and exoplanet transit spectroscopy. FGS/NIRISS has a wavelength range of 0.8 to 5.0 microns.

The sensitivity of the JWST instruments is summarised in Figure 1.10.

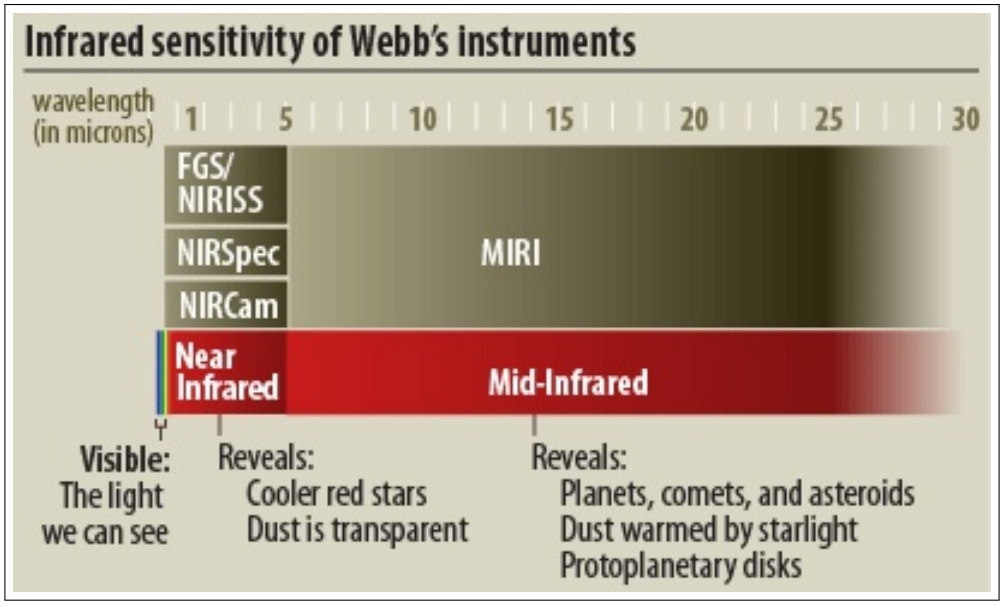

Figure 1.10: The JWST instruments sensitivity. Figure taken from `https://jwst.nasa.gov/content/observatory/instruments/fgs.html`.

The detection of nebula lines makes it possible to characterise the ionised gas in HII regions created by UV photons from newly formed stars, which are likely the main sources of the reionisation process (Mascia et al., 2023). Many JWST surveys are being (or will be) performed, and many results that are already coming are completely changing our theoretical understanding of the EoR galaxies. For instance, the recent confirmation of the presence of an AGN in a very distant galaxy ($z \approx 10.1$, Goulding et al. (2023),

Figure 1.11), and an intriguing number of AGN discovered at very high redshift values (e.g. Harikane et al. (2022); Furtak et al. (2023); Larson et al. (2023); Maiolino et al. (2023a,b)) are opening new questions about the formation of AGN within the first galaxies. In fact, at high redshifts, we expect rare AGN presence within small galaxies, due to the relatively less dense environment and to the relatively young stellar population of the EoR galaxies.

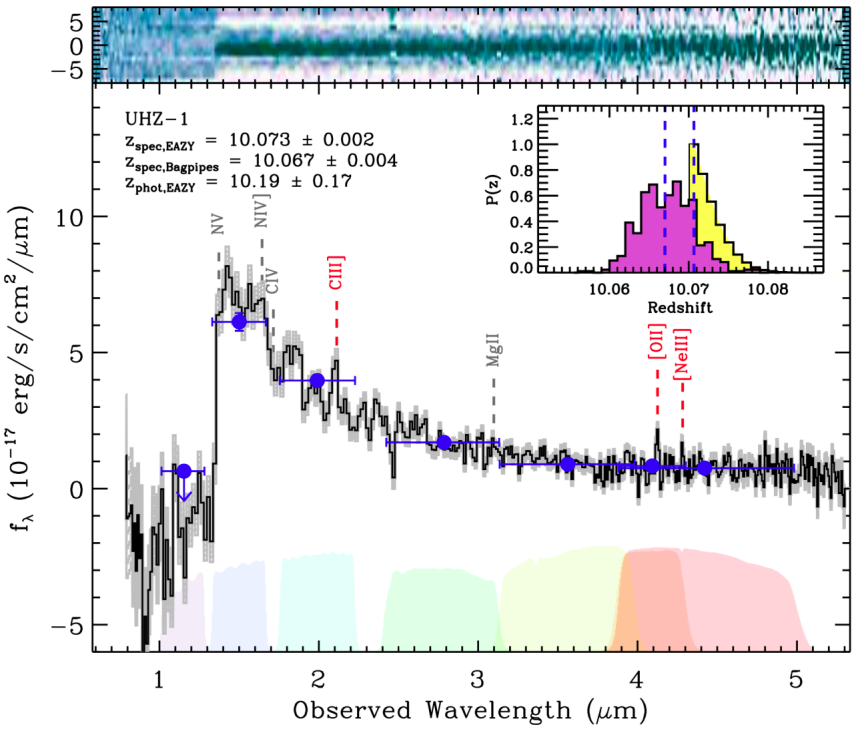

Figure 1.11: JWST/NIRSpec Prism spectroscopy of UHZ-1. Upper panel: 2D MSA Prism spectroscopy produced by msaexp. Lower panel: 1D spectral extraction in f_λ (in units of $10 - 17\,\mathrm{erg\,s^{-1}\,cm^{-2}\,\mu m^{-1}}$) with associated statistical uncertainties (gray shaded region). Prominent and/or expected emission features are highlighted assuming $z_{spec} = 10.07$ with significant $> 3\sigma$ detections and non-detections labeled in red and gray, respectively. Overlaid are the JWST/NIRCam photometry (blue circles) with associated filter responses highlighted. Inset panel: Redshift probability distributions for fits to the NIRSpec spectroscopy produced by EAZY (yellow) and BAGPIPES (purple) packages. Figure taken from Goulding et al. (2023).

Here I report a list of some key cosmological JWST surveys:

- **JWST Advanced Deep Extragalactic Survey (JADES)**, is a survey conducted by the Near-Infrared Camera (NIRCam) and Near-Infrared Spectrograph (NIRSpec) Instrument Development Teams in collaboration (Eisenstein et al., 2023). The JADES project is carrying out a comprehensive programme of deep infrared imaging and multi-object spectroscopy in the two most renowned deep fields in the sky: the Hubble Deep Field (GOODS-N) and the Hubble Ultra Deep Field (GOODS-S). The primary goal of the JADES survey is to investigate the evolution of the first galaxies.
- **Cosmic evolution early universe release science survey (CEERS)**, this survey

will cover an area of 100 square arcminutes in the Extended Groth Strip (EGS) field with imaging and spectroscopy from JWST's NIRCam, MIRI, and NIRSpec. This project will demonstrate, assess, and validate effective extragalactic surveys with simultaneous, overlapping parallel observations in a field that has a wealth of HST/CANDELS multi-wavelength data (Yang et al., 2023).

- **Public Release IMaging for Extragalactic Research (PRIMER)**, is a major public Treasury Programme that has been created to give the astronomical community access to a large-scale, uniform, and deep imaging survey of the JWST NIRCam+MIRI for COSMOS and UDS fields, which will be of great benefit and have a lasting impact. Exploiting the unique near-mid IR imaging capabilities of JWST, PRIMER will have an immediate scientific impact, revolutionising our knowledge of early galaxy and black hole formation/evolution out to the highest redshifts yet probed (Dunlop et al., 2021).

Recently, a JWST proposal (*PI: A.Faisst*) has been accepted to observe with NIRSpec 18 representative ALPINE galaxies between $4.4 < z < 5.7$, to obtain all major optical emission lines ([OII], Hβ, [OIII], [NII], Hα and [SII]). This redshift range corresponds to the end of the EoR and the highest redshift where it is possible to obtain a UV-submillimeter reference sample with today's facilities (JWST and ALMA).

1.5 Thesis Purpose

The main goal of my Master Thesis is to provide a self-consistent modelling of the line emission from different ISM phases (ionized gas in HII regions and neutral gas in PDRs) jointly detected by JWST and ALMA, respectively, in the ALPINE galaxies at $z \sim 5 - 6$. The aim is to identify and describe the ionised and neutral components of high-redshift galaxies through the use of emission lines that can be linked to the physical properties of the galaxies. I used my developed HII+PDR models to characterise the ISM properties of galaxies (e.g. gas density, ionisation parameter, gas metallicity) within the ALPINE survey. With the models developed in my Thesis I produced predictions regarding UV/optical ([OIII], [NII], CIII] and Hα) vs FIR line ([CII]) ratios in the sample.

In Chapter 2, I will discuss how the modelling has been implemented, together with details regarding the numerical modelling of the HII region + PDR radiative transfer. I will explain in detail the use of an analytical approach to calculate the ionisation parameter (U) and the density (n) for the ALPINE sample.
In Chapter 3, I will describe the datasets used for my Thesis work.

In Chapter 4, I will present the results of my work, namely the forecasts of the ratios between UV/optical lines ([OIII], [NII], CIII] and Hα) and FIR lines ([CII]). Moreover, I provide the Model validation using observations from the datasets described in the previous chapter and an in-depth analysis of the physical parameters determined for the ALPINE sample and the correlation between the UV/optical lines and the SFR. Finally, I will present the results relative to the predicted positions of the BPT diagrams for the ALPINE sample.

Chapter 2

ISM modelling

In this chapter, I provide an overview of the codes utilised to model the HII regions and PDRs for my study. I will provide a brief theoretical overview of the radiative transfer equation, which is the foundation of the CLOUDY code (Ferland et al., 2017). I will then provide a comprehensive overview of my simulation parameters.

2.1 Radiative transfer equation

Radiation coming from a source (usually called background radiation) is altered when passing through a medium, and so is detected by an observer (Tielens, 2005). We begin by considering the simplest scenario, in which only absorption material are present. In this case, a source emits radiation, and the medium between the source and the observer absorbs some of the photons (Karttunen, 2007):

$$dI_\nu = -\alpha\nu I_\nu ds \tag{2.1}$$

where I_ν is the flux for unit solid angle of the source $[\mathrm{ergs^{-1}Hz^{-1}cm^{-2}sr^{-1}}]$, ds is the infinitesimal distance between the source and us, and α is the absorption coefficient $[\mathrm{cm^{-1}}]$, that can be defined also by the opacity $k_\nu\,[\mathrm{cm^2\,gr^{-1}}]$:

$$\alpha = k_\nu \rho \tag{2.2}$$

The absorption coefficient of a gas is a measure of how much of a beam of light is absorbed by a unit volume of the gas (Karttunen, 2007). It is determined by the decrease in the intensity of the beam for each unit of distance through which it passes through the gas.

Now, assuming that the material absorbs and re-emits photons, the equation that explains the change in brightness will be now:

$$dI_\nu = -\alpha\nu I_\nu ds + \frac{j_\nu}{4\pi} ds \tag{2.3}$$

where j_ν is the emission coefficient, defined as the amount of energy released per unit time, solid angle, and frequency ($[\mathrm{erg\,s^{-1}\,sr^{-1}\,Hz^{-1}}]$) (Karttunen, 2007). We can define,

with the physical quantities just introduced, two important new quantities used to characterise the medium.
Optical depth (or optical thickness) is a measure of how much light is absorbed or scattered by a material (Karttunen, 2007):

$$\tau = \int \alpha\nu ds \tag{2.4}$$

The value of optical depth can describe if the medium can be defined as been optically thick or optically thin:

- **optically thick** $\tau >> 1$, for the Eq.2.4 we have that the absorption parameter would be high. An optically thick medium is one in which photons are so often absorbed or scattered that they cannot travel a long distance before being taken in or deflected. The intensity of light decreases rapidly as it travels through the medium.
- **optically thin** $\tau << 1$, for Eq.2.4 we have that the absorption parameter would be small. A medium is considered to be optically thin when a photon has a small chance of being absorbed by it as it passes through.

The source function is defined as the photon emission rate for a unit volume of gas (Karttunen, 2007). It is defined as the ratio of the emission coefficient to the absorption coefficient:

$$S_\nu = \frac{j_\nu}{4\pi\alpha\nu} \tag{2.5}$$

We can express the radiative transfer (RT) equation using the two quantities that were introduced to describe how the medium responses when it is exposed to a radiation field:

$$\frac{dI_\nu}{d\tau} = -I_\nu + S_\nu \tag{2.6}$$

The formal solution (Karttunen, 2007) for the radiative transfer equation, with S_ν constant, is:

$$I_\nu = I_\nu(0)e^{-\tau} + S_\nu(1 - e^{-\tau}) \tag{2.7}$$

If the optical depth approaches infinity, the intensity of the radiation, I_ν, will be equal to the source function, S_ν, and the emission of the background will no longer be distinguishable from the emission of the medium. In order to find a solution to the radiative transfer equation for a medium, we must solve the following equation simultaneously:

$$\begin{cases} \frac{dI_\nu}{d_\tau} = -I_\nu + S_\nu \\ \tau = \int \alpha\nu ds \\ \alpha\nu = \frac{h\nu}{4\pi}\phi(\nu) n_l B_{lu}(1 - \frac{g_l n_u}{g_u n_l}) \\ S_\nu = \frac{j_\nu}{4\pi\alpha\nu} \\ n_l n_{coll}\gamma_{lu} + n_l B_{lu} J_\nu = n_u n_{coll}\gamma_{ul} + n_u A_{ul} + n_u B_{ul} J_\nu \\ J_\nu = \frac{1}{4\pi}\int I_\nu d\Omega \end{cases} \tag{2.8}$$

where $\phi(\nu)$ is a function that describes the shape of the emission lines[1]

This system is complex to solve because there is not only one species present in the medium, and the energy level populations and intensity of radiation at a certain point in the medium are affected by the same parameters at another point in the medium and vice versa. Hence, we can get the physical condition of the medium in two different ways:

- **Escape probability formalism**, is an approximation that is applied by using the Large Velocity Gradient approximation (LVG) (see *Appendix A*).
- **Solve numerically full radiative transfer equations**, using a photoionising code like **CLOUDY** (Ferland et al., 2017).

2.2 CLOUDY code

CLOUDY is an open source nonlocal thermodynamic equilibrium (NLTE, *Section 1.2.1*) spectral synthesis and plasma code designed to simulate astrophysical environments and predict their spectra (Ferland et al., 2017). With the term "spectral synthesis code" we indicate a tool that can be used to model the emission spectra of stars and galaxies, given fixed physical properties (e.g. metallicity, initial mass function (IMF), age).

CLOUDY is able to model gas clouds with temperatures ranging from that of CMB at $z = 0$, to a maximum of $\sim 10^{10}\,K$, hence encompassing a variety of physical states from molecular gas to completely ionised gas. It can give predictions about the thermal, ionisation, and chemical structure of a cloud within these limits, and predict its observed spectrum.
The interesting feature of photoionisation codes such as CLOUDY is that they can provide predictions about emission lines for a given galactic environment with only a few physical parameters as input. The most basic CLOUDY modelling can be done by providing only three input parameters: the shape and strength of the SED that is impacting the cloud, the chemical composition of the cloud's gas, and the assumed geometry of the gas (usually spherical or slab).

CLOUDY is capable of calculating the non-equilibrium ionisation, thermal, and chemical state of a cloud that is exposed to an external source of radiation under the assumption that the chemical reactions have had enough time to reach equilibrium. This

[1] An example of this type of function is the shape function related to the natural broadening of a line, which is a result of the uncertainty principle of quantum mechanics. The so-called Lorentz profile:

$$\phi(\nu) \approx \frac{1}{[(\nu - \nu_0)^2 + (\frac{\gamma}{4\pi})^2]} \tag{2.9}$$

A different kind of shape function is the one caused by Doppler broadening of a line:

$$\phi(\nu) \approx \frac{1}{\Delta\nu_d * \sqrt{\pi}} exp(-(\nu - \nu_0)^2/\Delta\nu_d^2) \tag{2.10}$$

For more information about line profile, see Tielens (2005); Karttunen (2007).

implies that CLOUDY solves the radiative transfer equations associated with each element of the gas in order to achieve the stability of the gas.

Assuming incident radiation as the only energy source for the cloud, CLOUDY can calculate the reflected radiation, which is the emission from the illuminated side of the cloud that is sent back, as well as the transmitted radiation, which is the emission from the shielded side of the cloud that includes the diffuse radiation field and the attenuated incident radiation (see Figure 2.1).

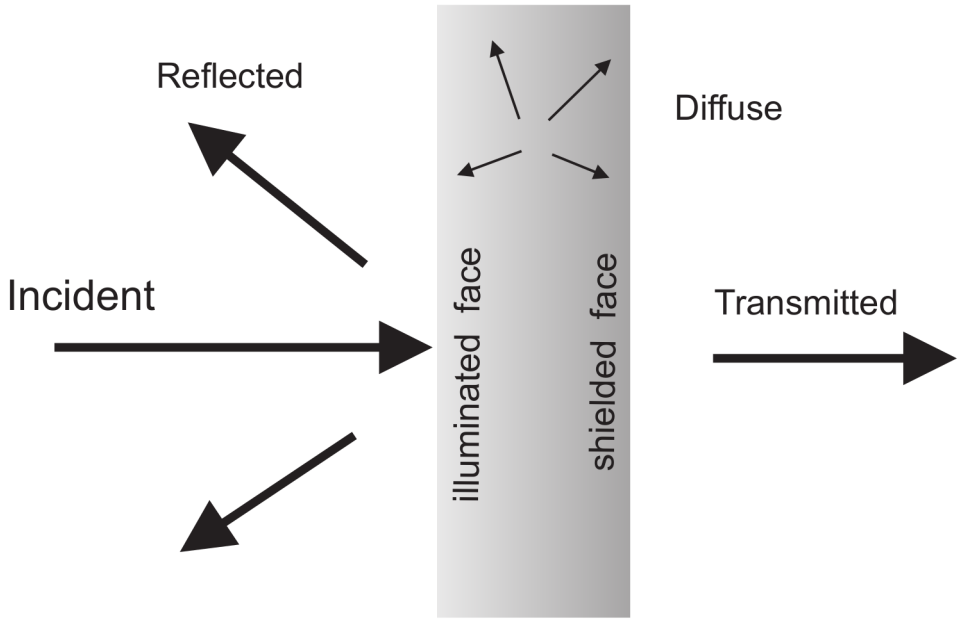

Figure 2.1: The radiation fields enetering in CLOUDY calculation. Figure taken from CLOUDY C22 version documentation.

The density of a certain gas species n_i is given by the following balance equation, derived from a different formulation of the radiative equations; see *Section 2.1*:

$$\frac{\partial n_i}{\partial t} = \sum_{j \neq i} n_j R_{ji} + Source - n_i(\sum_{ji} R_{ij} + L_i) = 0 \ \ [\mathrm{cm^{-3}\,s^{-1}}] \tag{2.11}$$

where R_{ji} represents the rate (in $\mathrm{s^{-1}}$) for a certain species to move from the energetic level j to i, $Source$ is the rate per unit volume (in $\mathrm{cm^{-3}\,s^{-1}}$) at which new atoms appear in i energetic level and L_i the rate (in $\mathrm{s^{-1}}$) at which they are lost (since they moved back to the j level or to another energetic level).
Together with the fluid equations, these can fully describe the cloud state. CLOUDY provides information about the fluid modelled by solving the dynamical equations of a fluid for each model cell. The equations for a non-magnetized fluid are (Clarke & Carswell, 2014):

$$\begin{cases} \frac{\partial \rho}{\partial t} + \nabla(\rho \mathbf{u}) = 0 \\ \rho(\frac{\partial \mathbf{u}}{\partial t} + (\mathbf{u}\nabla)\mathbf{u}) = -\rho\nabla\phi - \nabla P + \nabla\mathbf{\Pi} \\ \rho T(\frac{\partial s}{\partial t} + \mathbf{u}\nabla s) = \nabla\mathbf{u} \bullet \mathbf{\Pi} - \nabla\mathbf{F}_c \end{cases} \tag{2.12}$$

where ρ is the density of the gas, $\mathbf{u}$ is the average velocity of the gas, P is the pressure of the gas, ϕ is the potential (self-gravitating gas or external potential), T is the temperature of the gas, s is the specific entropy of the gas, $\mathbf{\Pi}$ is the viscosity stress tensor and $\mathbf{F}_c$ is the heat conduction.

In my Thesis, I used the 2022 version (C22 hereafter) of the code. Further details can be found in CLOUDY project website.

2.3 Incident Radiation Modelling

As pointed out in the previous section, any CLOUDY simulation needs the incident radiation as input. In what follows, I will discuss in detail how I modelled the shape of the spectral energy distribution (SED) produced by a star population in my Thesis. The shape of the incident SED is a major factor in predicting the emission lines from a cloud, as the properties of the emitting sources can impact the rate of ionisation and excitation of certain chemical species, thus influencing the predicted luminosity of that particular line. Regarding the modelling of HII regions and PDRs, we must simulate an incident radiation flux from a young stellar population, primarily emitting in the far ultraviolet (FUV) and extreme ultraviolet (EUV). I employed two distinct spectral synthesis programmes (Starburst99 and BPASS) which simulate the emitted spectrum of stellar populations as a function of their age, metallicity, and of the processes happening within the stellar sources (e.g. convection, nuclear fusion, etc...).

2.3.1 Starburst 99

Starburst99 (SB99, Leitherer et al. (1999)) is a comprehensive set of model predictions of the spectrophotometric properties of galaxies characterised by active star formation. SB99 can be employed to model the SED of a simple stellar population, without the inclusion of binary stars, with the option of either a single starburst or a continuous star formation rate. An example from the 1999 dataset (Leitherer et al., 1999) is shown in Figure 2.2, which displays the various SED shapes that occur as the stellar population evolves. It is evident that, as the stellar population evolves, the number of UV photons decreases in comparison to the number of IR photons, which are mainly emitted by older stars.

For my modelling, I choose two metallicities: sub-solar metallicity $Z \simeq 0.5\,\mathrm{Z}_\odot$ and solar metallicity $Z \simeq 1\,\mathrm{Z}_\odot$. The parameters employed for the SED modelling are listed in the Table 2.1, and a continuous star formation rate was adopted. Choosing a continuous star formation as a model is more reasonable than choosing a single starburst when considering the evolution of the earliest galaxies. This is because I want to analyse the first life instant of high-z galaxies, and I do not have clues about the fact that all the stars have been formed in a single burst. From this perspective, the assumption of continuous star formation is a less restrictive assumption with respect to the star formation history of the galaxy.

Total Stellar Mass $[\mathrm{M}_\odot]$	SFR $[\mathrm{M}_\odot\,\mathrm{yr}^{-1}]$	IMF exponent	Star mass limits $[\mathrm{M}_\odot]$
10^6	1	-2.35 (Salpeter)	$1-300$

Table 2.1: Principal settings for SED shape modelling for my study. These parameters are employed to create two SED shapes with a sub-solar metallicity of approximately 0.5 times the solar metallicity and a solar metallicity of approximately 1 solar metallicity.

I have chosen an age of $100\,\mathrm{Myr}$ for my models, so that the stellar population of my galaxies is very young. I have taken a continuous SFR for all 100 Myr. Moreover, I have decided to use a single starburst model of SB99 to create two SED shapes for a continuous SFR that was quenched at 5 and 35 Myr ago. The construction of these SED shapes is illustrated in the next subsection. All models have been running using servers of the Starburst99 project.

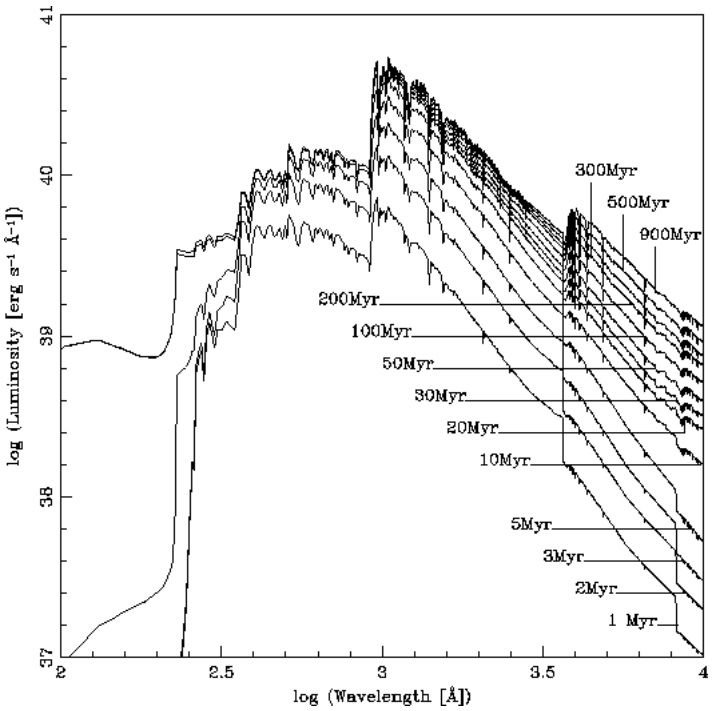

Figure 2.2: SED shape modelling from a SB99 simulation. The shape is reported for different time-steps of stellar population evolution. The model is based on a continuous star-formation rate of $1\,\mathrm{M}_\odot\,\mathrm{yr}^{-1}$, a single Salpeter IMF law (power-law with index $\alpha = 2.35$), a metallicity of $Z \sim 1\,\mathrm{Z}_\odot$ and a range of star masses between $1\,\mathrm{M}_\odot$ and $100\,\mathrm{M}_\odot$. The figure is taken from `https://www.stsci.edu/science/starburst99/docs/popmenu.html`.

2.3.2 Binary Population and Spectral Synthesis code (BPASS)

The Binary Population and Spectral Synthesis code (BPASS, Stanway & Eldridge (2018)) is a suite of synthetic stellar population and of binary stellar evolution models. In contrast to SB99, the BPASS code can include the effect of a population of binary

stars in the spectral energy distribution. Two stars that are orbiting around their common centre of mass form a binary star system. The most luminous star is classified as the primary star, while the faintest star is classified as the secondary star. These systems can move mass from the primary stars to the secondary one, providing the secondary one with additional fuel to burn as an accretion disc. The emission coming from this process can alter the calculation of the stellar population age.

The presence of binary stars can have a significant effect on the study of ultraviolet emission lines, particularly those that are used to trace HII regions. The presence of binary stars in fact leads to a greater emission of FUV and EUV photons from a star population than if there were no binaries. In *Chapter* 4, I will discuss further this aspect.

The BPASS code is based on the solution of three main steps, based on the equation of stellar evolution and stellar dynamics. In Figure 2.3 I present a sketch of these stages, as outlined in the BPASS user manual.

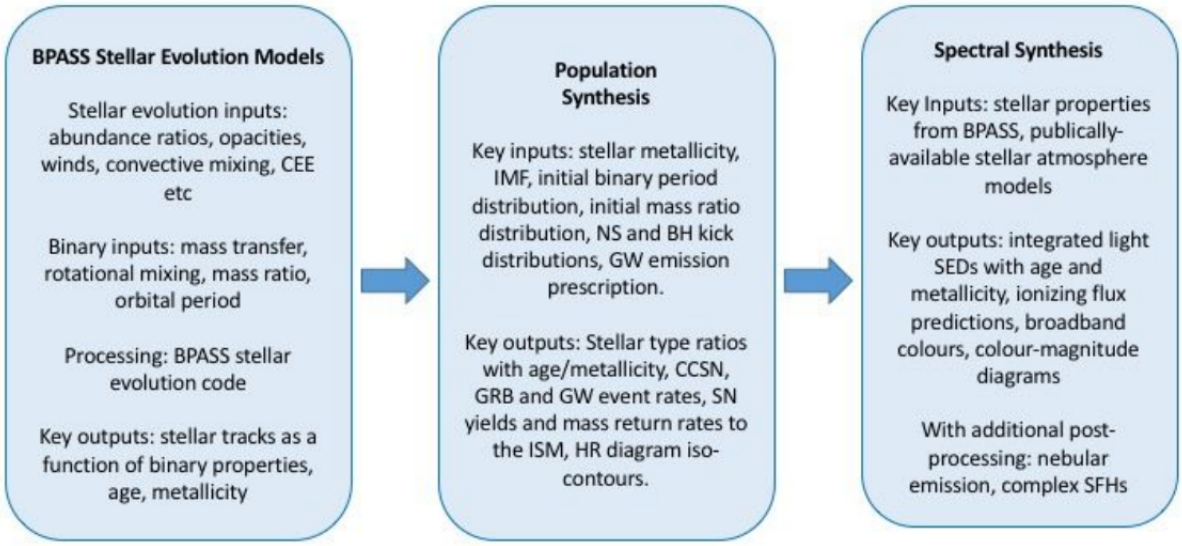

Figure 2.3: Three main steps of BPASS code for generation of SED shape models. The figure is taken from the BPASS v2.2.1 manual.

In the Figure 2.4 is reported an example of SED shape from a BPASS model. For my modelling, I used the BPASS models from BPASS v2.2.1, with the parameters listed in Table 2.2. As for the SB99 case, I assumed two metallicities ($Z = 0.5\,Z_{\odot}$ and $Z = 1\,Z_{\odot}$), 100 Myr for the age of the stellar population and another two SED shapes with quenching in SF.

Total Stellar Mass $[\mathrm{M}_\odot]$	IMF exponent (a) [0.1-0.5 $\mathrm{M}_\odot$]	IMF exponent (b) [0.5-300 $\mathrm{M}_\odot$]	Star mass limits $[\mathrm{M}_\odot]$
10^6	-1.30	-2.35 (Salpeter)	$1 - 300$

Table 2.2: Principal settings for SED shape modelling for my study. The two IMF exponents are related to the reported range of star mass simulated. These settings are related to a single starburst model. For more information, refer to the BPASS v2.2.1 manual.

Unfortunately, BPASS does not provide complex or composite stellar populations as part of the standard release. However, it is possible to construct a composite stellar population by assuming a certain star formation history and combining models of different ages in the correct proportion to build a mixed-age population. The same technique was employed with SB99 models to generate SEDs for star populations with quenching in SF. I built the simplest case of a constant SFR $1\,\mathrm{M}_\odot\,\mathrm{yr}^{-1}$ to have a continuous star formation mode comparable to that I used for SB99. To achieve this, I developed a `Python` programme that computes:

$$F(\lambda) = f_0(\lambda)\Delta t_0 + \sum_{i=1}^{max} f_i(\lambda)\Delta t_i \tag{2.13}$$

where $F(\lambda)$ is the flux of the composite population, f_i is the flux of the simple stellar population in age bins. In particular, we have $\Delta t_i = 10^{6.15+0.1i} - 10^{6.05+0.1i}$ for $i > 0$. The interested reader can find the code in *Appendix D*.

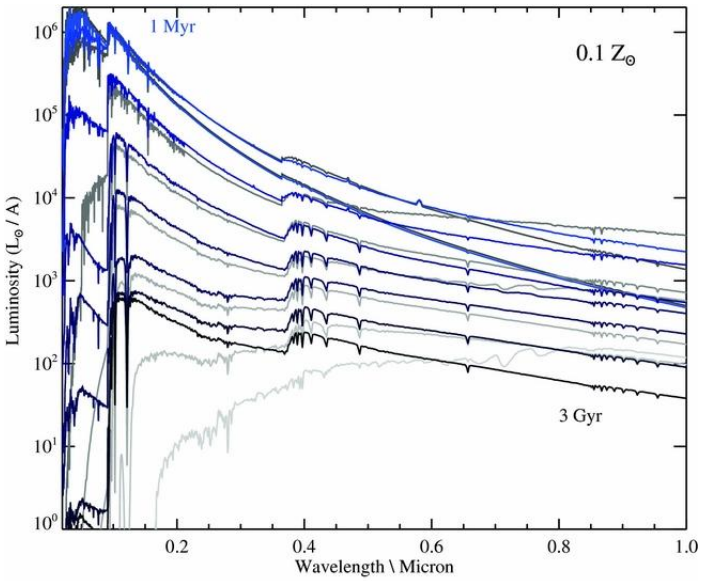

Figure 2.4: The synthetic spectra produced for a co-eval population (i.e. instantaneous starburst) at times of 1, 3, 10, 30, 100, 300, 1 000, and 3 000 Myr after star formation. Spectra are shown for binary populations (bold, coloured lines) and single stars (pale, greyscale line), and at metallicities of $Z = 0.1\,\mathrm{Z}_\odot$. Figure taken from Eldridge & Stanway (2022).

2.4 The final set of CLOUDY models

I will now explain in detail the CLOUDY input file I created to perform the CLOUDY radiative transfer calculations that allowed me to obtain the expected line emission from HII regions and PDRs (see *Appendix E*).

CLOUDY simulates the HII regions + PDRs by performing a radiative transfer computation through a 1-D gas slab of fixed hydrogen gas density (n), ionisation parameter (U) and metallicity (Z). I create a grid of CLOUDY models varying these three free parameters as outlined in Tab.2.3. The `Python/bash` programme I developed to generate all the CLOUDY input files is visible in *Appendix F*.

logarithmic hydrogen density ($log(n)$)	$[0.5, 3.5]$, 0.5 steps
ionisation parameter (U)	$[-3, -0.5]$, 0.5 steps
metallicity SED sub-solar (Z [$Z_\odot$])	$[0.15, 0.55]$, in 0.10 steps
metallicity SED solar (Z [$Z_\odot$])	$[0.65, 1.05]$, in 0.10 steps

Table 2.3: Adopted values of free-parameters for the CLOUDY simulations.

For incident radiation, I assumed the different SED shapes from SB99 and BPASS, normalised with the value of U. The radiation emitted by the stellar population strikes the illuminated face of the cloud in CLOUDY, which is assumed to have a slab geometry.

CLOUDY read the SB99 and BPASS SED constructed, and normalised it with respect to the U value.

```
table sed "<SB99><BPASS>_0.008_100Myr.sed"
ionization parameter -3
```

The abundance of metal species is set to match the values from Grevesse et al. (2010) (the "abundance *GASS*" command in CLOUDY) at solar value, and I assume that they linearly scale with Z. I included the ISM grain distribution assuming the default one for the Milky Way (MW) and the CMB radiation intensity at $z = 6$, which is approximately the redshift of the ALPINE sample. I considered a microturbulence gas velocity of $1.5\,\mathrm{km\,s^{-1}}$ a Galactic cosmic-ray background contribution (Indriolo et al., 2007). Turbulence affects the shielding and pumping of the lines, and can be important in an astrophysical fluid with an higher value of Reynolds number[2] ($Re > 10^2 - 10^3$, Clarke & Carswell (2014)). The cosmic-ray background must be included if the calculation extends into molecular regions, due to the ion-molecule chemistry that occurs in the cold ISM that requires a source of ionisation, for a cosmic-ray definition (see *Section 1.3.3*).

```
hden 0.5
abundances GASS no grains
metals and grains linear 0.15
```

[2]The dimensionless Reynolds number is defined as the ratio between the inertia associated to the gas $\sim \rho U^2$, where U is the average velocity and ρ the average density of the gas, and the viscosity stress tensor Π:

$$Re = \frac{\rho U^2}{\Pi}$$

In general, the astrophysical fluids have values of $Re >> 1$.

```
turbulence 1.5 km/s
CMB, z=6
cosmic rays background
iterate to convergence
grains ISM no qheat
grains PAH no qheat function 3
```

In the code, `hden` is the logarithmic hydrogen density, `metals and grains linear` is the Z value. The `grains` commands are associated to the ISM grain distribution for the MW. With the `iterate to convergence` command, the code will continue to iterate the computation of the single gas cells until the optical depths have converged. The stopping criterion for my models is set in terms of the gas column density ($N_H = 10^{22}\,\mathrm{cm}^{-2}$), to simulate the entire HII region and part of the neutral PDR.

```
stop temperature off
stop column density 22
```

The input file ends with instructions that store the results of the CLOUDY simulation, particularly the emission lines that are emitted from the HII region and PDR that are specified in the code.

```
save last overview last ".ovr"
save last PDR ".pdr"
save last heating ".het"
save last cooling ".col"
save last lines, array ".lina" last, units microns
save last continuum last ".con" units microns
save last species all densities ".spc"
save last grain temperature last ".grntem"
save last lines zone cumulative emergent ".linc"
...
C  2  157.636m
...
O  3  88.3323m
...
H  1  6562.81A  #H-alpha
H  1  4862.72A  #H-beta
O  3  5006.84A
O  3  4958.91A
...
N  2  6583.45A
...
C  3  1908.73A
...
end of lines
```

2.5 Derivation of U and n

The CLOUDY models are obtained on a grid of three free parameters (n, U and Z). For this reason, to predict the expected line ratios of a given galaxy, I need to estimate the gas density, ionisation parameter, and metallicity for the observed galaxy. For my Thesis, I have fixed the metallicity value for the galaxies being studied. Instead, the ionisation parameter and the gas density are computed by exploiting the analytical model presented in Ferrara et al. (2019).

The Ferrara et al. (2019) model has been built in order to clarify the origin of [CII]-deficiency observable in high-redshift galaxies ($z > 5$) in respect to the tight relation between [CII] and star formation rate in local galaxies. The analytical model assumes that a galaxy can be represented as a flat, parallel slab of gas with a uniform number density, metal content, and total gas column density. The galaxy is illuminated by a source able to emit ionising and non-ionising radiation. The representation of the structure of the analytical model is visible in Figure 2.5.

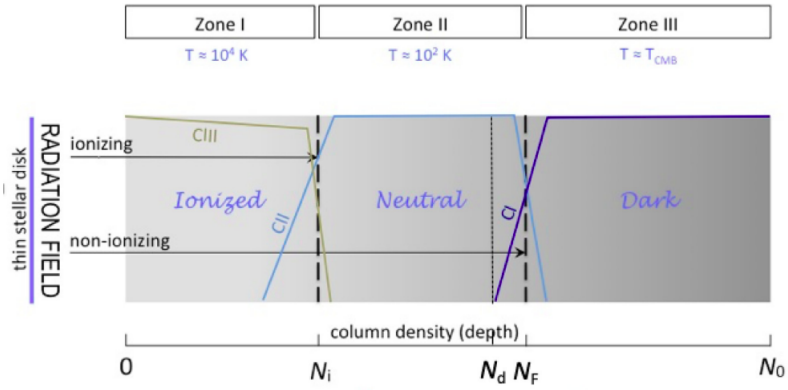

Figure 2.5: Schematic ionisation structure of galaxy model. The radiation field produced by the thin layer of stars located at the galaxy mid-plane illuminates the overlying gas slab of total column density N_0. Figure taken from Ferrara et al. (2019).

The model links U and n to global (measurable) galaxy properties, namely:

$$n = 5.4 \times 10^{-13} {\Sigma_g}^2 {\sigma_{kms}}^2 \ [\mathrm{cm}^{-3}] \tag{2.14}$$

$$U = 1.7 \times 10^{14} \frac{\Sigma_{SFR}}{\Sigma_g^2} \tag{2.15}$$

Where Σ_g is the gas surface density, Σ_{SFR} is the SFR surface density, and σ_{kms} is defined by the rms turbulent velocity σ as $\sigma_{kms} = \sigma/(\mathrm{km\,s^{-1}})$.
For σ_{kms}, I assumed a reference value of $10\,\mathrm{km\,s^{-1}}$ reported in Ferrara et al. (2019).

I used the Kennicutt-Schmidt (KS, Schmidt (1959); Kennicutt (1998)) law to derive Σ_{gas} from the measured Σ_{SFR} in ALPINE galaxies, by inverting the relation:

$$\Sigma_{SFR} = 10^{12} k_s \Sigma_g^m \ \ [\mathrm{M_\odot\,yr^{-1}\,cm^{-2}}] \ \ (\mathrm{m} = 1.4) \tag{2.16}$$

I estimated Σ_{SFR} from the SFR and the r_{UV} measured for ALPINE galaxies (Fujimoto et al., 2020). In the previous equation, Ferrara et al. (2019) introduced the burstiness parameter (k_s), defined as the deviation from the Kennicutt-Schmidt relation. Galaxies with higher values of k_s can convert gas more efficiently in new stars, compared to non-deviating KS law galaxies. This suggests that these galaxies are highly efficient star-forming galaxies (starburst galaxies). The dependence of the parameters n and U on the KS law makes both strictly connected with the burstiness parameter k_s.

Chapter 3

Datasets

In this chapter, I present an overview of the observational data that I used for my Thesis work. I will discuss the ALPINE dataset, for which I have forecasted the UV and optical luminosities of different lines. Next, I will present two collections of galaxies, VANDELS & VUDS and CANDELS/SHARDS, that I have used to validate my models.

3.1 ALPINE

As introduced in *Section* 1.4.1, ALPINE (Béthermin et al., 2020; Le Fèvre et al., 2020; Faisst et al., 2020) is an ALMA large programme, aimed at measuring [CII] $158\,\mu\mathrm{m}$ and rest-frame FIR continuum emission from a representative sample of 118 main-sequence galaxies at $4.4 < z < 5.8$. Observations were carried out between May 2018 and February 2019 (Béthermin et al., 2020; Faisst et al., 2020). The ALMA angular resolution reched for [CII] observation is $0,9''$ and a sensitivity of $0.35\,\mathrm{mJy\,beam^{-1}}$ per spectral channel. All galaxies are located in the regions of the Cosmic Evolution Survey (COSMOS), and the Extended Chandra Deep Field South (ECDFS). The data used in the area of the ECDFS are from the Cosmic Assembly Near-Infrared Deep Extragalactic Legacy Survey (CANDELS) survey.

COSMOS is an astronomical survey that investigates the formation and evolution of galaxies in terms of both cosmic time and the local galaxy environment. The survey covers an equatorial field with spectroscopy and X-ray to radio imaging from both space and ground-based telescopes. More than 2 million galaxies have been detected, spanning 75% of the age of the Universe (Scoville, 2007). ECDFS field is an area of the sky that has been extensively studied by various telescopes and observatories across different wavelengths, from radio waves to X-rays. It's located in the Southern Hemisphere and spans approximately 30 square arcminutes. CANDELS is designed to document the first third of galactic evolution, over the approximate redshift range $1.5 - 8$. It images > 250000 distant galaxies using the Hubble Space Telescope, from the mid-ultraviolet to the near-infrared, and has the objective of measuring Type Ia supernovae to test their accuracy as standardisable candles for cosmology (Grogin et al., 2011).

The galaxies of the ALPINE sample have star-formation rates SFR$\gtrsim 10\,\mathrm{M_\odot\,yr^{-1}}$ and stellar masses $M_\star \sim 10^9 - 10^{11}\,\mathrm{M_\odot}$. Both the stellar mass and the SFR have been

obtained from SED fitting by Faisst et al. (2020).

For my Thesis work, I selected 36 ALPINE galaxies for which I have the values of SFR, [CII] luminosity (Faisst et al., 2020) and UV radius (Fujimoto et al., 2020). These data are necessary to use the analytical model described in *Section* 2.5 to find the values of the physical parameters n and U, corresponding to the ISM density and the ionisation parameter of the radiation field (see *Section* 2.5), respectively. In Table 3.1 the properties of the 36 galaxies analysed are reported.

In Table 3.2 instead, I report the corresponding values (U, n) associated with each of these 36 galaxies for different assumed values of the burstiness parameter k_s (see *Section* 2.5). I adopted three values of k_s (1,5 and 10) to calculate U and n for the galaxies under analysis, then these three sets of analytical predictions of n and U for different values k_s were used to make line ratio predictions from the relevant CLOUDY models. These values are assumed because from Markov et al. (2022) and Vallini et al. (2021) the values of k_s for galaxies at redshift around $z \sim 5$ is around $k_s = 5$. Taking also $k_s = 1$ and $k_s = 10$, I am taking the possibilities of non-starburst galaxies and extreme starburst galaxies.

Considering a couple of (U, n) values, and assuming that the ALPINE sample has $Z = 0.5\,\mathrm{Z}_\odot$ (Burgarella et al., 2022), I can take the corresponding line ratio $R(n, U, Z)$ with respect to the [CII] line from the output of my CLOUDY models (see *Chapter* 2) and thus make predictions of UV and optical lines from the observed [CII] $158\mu\mathrm{m}$ luminosities:

$$L_{prediction} = R(n, U, Z) \cdot L_{[CII]} \tag{3.1}$$

3.2 VANDELS and VUDS galaxies

Before proceeding with the ultimate goal of the thesis work, namely predicting nebular line luminosities in the ALPINE sample, I need to check the goodness of the modelling procedure. For doing that I validate the model with a control sample of galaxies with both [CII] and UV (or optical luminosity) observed. Llerena et al. (2023) published the CIII] $1909\mathring{A}$, [OIII] $5007\mathring{A}$ and $H\alpha$ $6563\mathring{A}$ fluxes for 17 VANDELS and 18 VUDS galaxies with redshifts $z \sim 3$. Moreover, for this sample, we also have the SFRs.

VANDELS is a deep VIsible MultiObject Spectrograph (VIMOS) survey (*PI: Pentericci*) of the CANDELS fields. It is a completed ESO public spectroscopic survey carried out using the Very Large Telescope (VLT)(Llerena et al., 2023) using the VIMOS spectrograph. It was designed to build a sample of high signal-to-noise, medium resolution spectra of galaxies at redshifts between 1 and 6.5. The VIMOS Ultra Deep Survey (VUDS) (*PI: Le Févre*) is a massive spectroscopic campaign that is conducted using VIMOS reaching extreme depths ($< 25\,\mathrm{mag}$) in three well-studied extragalactic fields, in particular COSMOS (Llerena et al., 2023). It contains $\sim 10^4$ very faint galaxies at redshifts between 2 and 6.

In Table 3.3 the observed data used to validate my models are reported. In particular, the luminosities have been computed from the integrated line flux densities using the

following equation:

$$L_{lines} = F_{lines} \cdot 4\pi D_L(z)^2 \tag{3.2}$$

where $D_L(z)$ is the luminosity distance, computed under the assumption of a Λ_{CDM} cosmology[1]. To compute the [CII] luminosity, I use the De Looze et al. (2014) relation, reported in Eq.1.31.

For the validation of CLOUDY models, the free parameters n and Z are varied. The parameter U is computed from the SFR values, assuming the following relations (Pallottini et al., 2022):

$$G = G_0(SFR/\mathrm{M_\odot yr^{-1}}) \tag{3.3}$$

$$G/G_0 \sim U(n/\mathrm{cm^{-3}})10^3 \tag{3.4}$$

where G_0 is the Habing unit.

3.3 CANDELS/SHARDS Catalogue in GOODS-N

Another dataset used to check the validity of CLOUDY models is the CANDELS/SHARDS multi-wavelength catalogue in GOODS-N. From this catalogue, I take the observed [OIII] $5007\mathring{\mathrm{A}}$ and Hα $6563\mathring{\mathrm{A}}$ fluxes, and the associated value of SFR for these galaxies. In particular, I selected all the galaxies in the catalogue with $z > 2.5$.

GOODS aims to unite extremely deep observations from space and ground-based facilities. The survey consists of two $10 \times 16.5\,\mathrm{arcmin}^2$ fields: GOODS-N coincides with the Hubble Deep Field North, while GOODS-S coincides with the Chandra Deep Field South (Giavalisco et al., 2004) CANDELS/GOODS-N field containing photometry from ultraviolet (UV) to far infrared (FIR), photometric redshifts, and stellar parameters derived from the analysis of the multiwavelength data. The catalogue contains 35445 galaxies (Barro et al., 2019). SHARD stands for "Survey for High-z Absorption Red and Dead Sources" It is an additional survey within the CANDELS project that focuses on identifying high-redshift galaxies showing signs of "quenching" or ceasing to form new stars.

The treatment of these data is the same adopted for the selected VANDELS and VUDS galaxies (details in *Section* 3.2). I reported the observed data used to validate my models in Table 3.4.

[1] $\Omega_M = 0.3$, $\Omega_\Lambda = 0.7$, $H_0 = 70\,kms^{-1}Mpc^{-1}$

Table 3.1: ALPINE galaxies considered in this thesis.

Galaxy ID	z	r_{UV} [kpc]	$L_{[CII]}$ [10^8 $L_\odot$]	$\log(SFR_{SED})$ [$M_\odot$ yr^{-1}]
DC_308643	4.5253	0.9	(5.69 ± 0.89)	$1.83^{+1.95}_{-1.61}$
DC_351640	5.7058	0.24	(2.35 ± 0.51)	$1.19^{+1.39}_{-1.08}$
DC_372292	5.1364	1.01	(3.93 ± 0.50)	$1.45^{+1.69}_{-1.21}$
DC_396844	4.5424	0.58	(11.53 ± 1.02)	$1.74^{+1.98}_{-1.47}$
DC_416105	5.6309	0.97	(1.34 ± 0.30)	$1.08^{+1.20}_{-0.97}$
DC_417567	5.67	0.65	(3.13 ± 0.54)	$1.87^{+2.11}_{-1.65}$
DC_422677	4.4381	0.58	(4.22 ± 0.70)	$1.90^{+2.11}_{-1.71}$
DC_432340	4.4045	1.0	(3.57 ± 0.86)	$1.79^{+2.05}_{-1.53}$
DC_434239	4.4883	1.94	(14.07 ± 1.66)	$2.00^{+2.27}_{-1.71}$
DC_454608	4.5834	0.87	(6.44 ± 1.08)	$1.67^{+1.87}_{-1.38}$
DC_488399	5.6704	0.47	(10.79 ± 0.50)	$1.67^{+1.93}_{-1.39}$
DC_493583	4.5134	0.64	(4.32 ± 0.63)	$1.36^{+1.63}_{-1.14}$
DC_494763	5.2337	0.65	(4.87 ± 0.56)	$1.30^{+1.60}_{-1.00}$
DC_539609	5.1818	0.77	(4.91 ± 0.64)	$1.48^{+1.58}_{-1.41}$
DC_552206	5.5016	0.96	(15.25 ± 1.17)	$2.24^{+2.51}_{-1.96}$
DC_627939	4.5341	0.86	(7.24 ± 0.63)	$1.71^{+1.92}_{-1.45}$
DC_628063	4.5327	0.77	(1.16 ± 0.32)	$1.39^{+1.72}_{-1.12}$
DC_683613	5.542	0.57	(7.97 ± 0.68)	$1.77^{+2.01}_{-1.51}$
DC_733857	4.5445	0.6	(4.82 ± 0.77)	$1.59^{+1.82}_{-1.39}$
DC_773957	5.6773	0.76	(4.18 ± 0.56)	$1.43^{+1.69}_{-1.19}$
DC_818760	4.5613	0.75	(43.00 ± 1.69)	$2.68^{+2.87}_{-2.43}$
DC_834764	4.5058	0.88	(5.63 ± 1.14)	$1.36^{+1.57}_{-1.23}$
DC_842313	4.5537	1.9	(4.54 ± 0.81)	$2.28^{+2.49}_{-2.12}$
DC_848185	5.2931	0.9	(16.02 ± 0.95)	$2.46^{+2.57}_{-2.24}$
DC_873321	5.1542	0.91	(9.51 ± 1.07)	$1.96^{+2.18}_{-1.79}$
DC_873756	4.5457	1.08	(36.22 ± 1.30)	$0.73^{+1.19}_{-0.51}$
DC_880016	4.5415	0.77	(5.53 ± 0.74)	$1.50^{+1.76}_{-1.22}$
VC_5100537582	4.5501	0.54	(4.43 ± 0.67)	$1.17^{+1.46}_{-0.94}$
VC_5100559223	4.5627	0.97	(4.39 ± 0.78)	$1.52^{+1.74}_{-1.29}$
VC_5100822662	4.5205	1.32	(7.86 ± 0.65)	$1.82^{+2.05}_{-1.57}$
VC_5100969402	4.5785	0.59	(5.23 ± 0.55)	$1.29^{+1.54}_{-1.06}$
VC_5100994794	4.5802	1.63	(5.6 ± 0.51)	$1.45^{+1.71}_{-1.16}$
VC_5101218326	4.5739	1.46	(18.25 ± 0.78)	$1.06^{+1.57}_{-0.95}$
VC_510786441	4.4635	0.85	(6.60 ± 0.70)	$1.60^{+1.89}_{-1.46}$
VC_5110377875	4.5505	0.93	(17.14 ± 1.06)	$2.00^{+2.25}_{-1.76}$
VC_5180966608	4.5296	0.71	(13.72 ± 1.09)	$2.15^{+2.42}_{-1.90}$

Note: r_{UV} is derived from rest-frame UV emission in the HST/F814W map (Fujimoto et al., 2020). SFRs are derived from template SED fitting using the ancillary photometry available data sets from the rest-frame UV to IR wavelengths (Faisst et al., 2020). [CII] luminosity is taken from Béthermin et al. (2020).

Table 3.2: ALPINE galaxies considered, with the corresponding ionization parameter U and hydrogen density n values for different burstiness parameter k_s values. These values are computed following the analytical model presented in *Section* 2.5.

Galaxy ID	$U_{k_s=1}$	$U_{k_s=5}$	$U_{k_s=10}$	$n_{k_s=1}$ $[\mathrm{cm}^{-3}]$	$n_{k_s=5}$ $[\mathrm{cm}^{-3}]$	$n_{k_s=10}$ $[\mathrm{cm}^{-3}]$
DC_308643	-3.39	-2.40	-1.97	4.48	3.48	3.05
DC_351640	-3.61	-2.62	-2.19	5.21	4.22	3.79
DC_372292	-3.19	-2.19	-1.76	3.80	2.80	2.37
DC_396844	-3.52	-2.52	-2.09	4.90	3.90	3.47
DC_416105	-3.04	-2.04	-1.61	3.31	2.31	1.88
DC_417567	-3.53	-2.53	-2.10	4.95	3.95	3.52
DC_422677	-3.59	-2.59	-2.16	5.12	4.13	3.70
DC_432340	-3.34	-2.34	-1.91	4.30	3.30	2.87
DC_434239	-3.18	-2.18	-1.75	3.76	2.77	2.34
DC_454608	-3.34	-2.34	-1.91	4.29	3.29	2.86
DC_488399	-3.57	-2.57	-2.14	5.05	4.05	3.62
DC_493583	-3.32	-2.32	-1.89	4.23	3.24	2.81
DC_494763	-3.29	-2.29	-1.86	4.13	3.13	2.70
DC_539609	-3.30	-2.30	-1.87	4.18	3.18	2.75
DC_552206	-3.55	-2.55	-2.12	4.99	3.99	3.56
DC_627939	-3.36	-2.36	-1.93	4.37	3.37	2.94
DC_628063	-3.26	-2.26	-1.83	4.04	3.05	2.62
DC_683613	-3.54	-2.54	-2.11	4.95	3.96	3.53
DC_733857	-3.44	-2.45	-2.02	4.65	3.65	3.22
DC_773957	-3.29	-2.29	-1.86	4.12	3.12	2.69
DC_818760	-3.83	-2.83	-2.40	5.92	4.92	4.49
DC_834764	-3.20	-2.20	-1.77	3.84	2.84	2.41
DC_842313	-3.31	-2.31	-1.88	4.20	3.20	2.77
DC_848185	-3.66	-2.66	-2.23	5.37	4.37	3.94
DC_873321	-3.45	-2.45	-2.02	4.65	3.65	3.22
DC_873756	-2.85	-1.85	-1.42	2.68	1.68	1.25
DC_880016	-3.31	-2.31	-1.88	4.21	3.21	2.78
VC_5100537582	-3.30	-2.30	-1.87	4.17	3.17	2.74
VC_5100559223	-3.23	-2.24	-1.81	3.95	2.95	2.52
VC_5100822662	-3.25	-2.25	-1.82	3.99	2.99	2.56
VC_5100969402	-3.32	-2.32	-1.89	4.23	3.23	2.80
VC_5100994794	-3.01	-2.01	-1.58	3.21	2.21	1.78
VC_5101218326	-2.89	-1.89	-1.46	2.78	1.79	1.36
VC_510786441	-3.32	-2.32	-1.89	4.22	3.22	2.79
VC_5110377875	-3.45	-2.45	-2.02	4.67	3.67	3.24
VC_5180966608	-3.62	-2.62	-2.19	5.23	4.23	3.80

Table 3.3: VANDELS and VUDS galaxies data from the work of Llerena et al. (2023).

Galaxy ID	z	$\log(SFR_{SED})$ $[\mathrm{M_\odot\,yr^{-1}}]$	$L_{[CII]}$ $[10^8\,\mathrm{L_\odot}]$	$L_{CIII]}$ $[10^8\,\mathrm{L_\odot}]$	$L_{[OIII]}$ $[10^8\,\mathrm{L_\odot}]$	$L_{H\alpha}$ $[10^8\,\mathrm{L_\odot}]$
UDS020394	3.308	0.84 ± 0.10	0.37	1.11 ± 0.17	16.29 ± 0.86	–
CDFS020954	3.496	1.72 ± 0.03	2.82	1.30 ± 0.24	34.51 ± 3.95	–
CDFS023527	3.11	1.53 ± 0.09	1.82	2.04 ± 0.31	328.20 ± 4.94	–
UDS021601	3.344	1.01 ± 0.10	0.55	0.75 ± 0.20	8.85 ± 0.33	–
CDFS022563	3.003	1.19 ± 0.07	0.83	0.66 ± 0.10	9.16 ± 0.34	–
UDS022487	3.064	1.34 ± 0.15	1.17	0.84 ± 0.19	27.35 ± 5.49	–
CDFS015347	3.516	1.18 ± 0.08	0.81	0.74 ± 0.29	10.98 ± 0.51	–
CDFS019276	3.4	2.27 ± 0.07	10.00	2.05 ± 0.58	43.28 ± 7.12	–
UDS020928	3.137	1.78 ± 0.05	3.24	0.72 ± 0.16	32.11 ± 3.11	–
CDFS019946	2.437	1.21 ± 0.06	0.87	0.39 ± 0.07	6.23 ± 1.00	4.05 ± 0.25
UDS020437	3.207	1.42 ± 0.11	1.41	0.95 ± 0.35	26.13 ± 2.67	–
CDFS018182	2.317	1.34 ± 0.07	1.17	0.95 ± 0.15	17.83 ± 1.29	10.04 ± 0.37
CDFS018882	3.403	1.80 ± 0.08	3.39	0.79 ± 0.17	17.29 ± 0.87	–
CDFS025828	3.35	2.03 ± 0.05	5.75	1.38 ± 0.32	10.67 ± 0.36	–
CDFS022799	2.544	1.86 ± 0.04	3.89	1.27 ± 0.16	33.46 ± 5.10	18.38 ± 0.42
UDS021398	2.492	1.41 ± 0.05	1.38	0.40 ± 0.09	16.98 ± 1.55	10.05 ± 0.54
UDS015872	2.301	1.66 ± 0.04	2.45	0.30 ± 0.07	7.36 ± 0.82	6.96 ± 0.30
5100998761	2.453	0.84 ± 0.04	0.37	2.41 ± 0.20	13.48 ± 0.86	4.56 ± 0.81
5101444192	3.42	1.77 ± 0.03	3.16	2.97 ± 0.30	70.18 ± 1.33	–
510994594	3.297	1.31 ± 0.12	1.10	2.31 ± 0.24	32.61 ± 2.35	–
5101421970	2.47	1.08 ± 0.07	0.65	3.02 ± 0.28	22.31 ± 2.24	11.77 ± 1.02
510838687	2.557	1.22 ± 0.09	0.89	1.61 ± 0.22	18.04 ± 0.45	4.34 ± 0.82
5100556178	2.537	1.16 ± 0.08	0.78	1.25 ± 0.14	17.83 ± 0.63	13.12 ± 1.76
511229433	3.256	1.25 ± 0.16	0.95	2.27 ± 0.33	69.90 ± 3.74	–
511245444	3.038	$1.31 \pm .12$	1.10	1.60 ± 0.43	43.88 ± 10.02	–
530048433	2.312	0.95 ± 0.06	0.48	1.50 ± 0.26	27.43 ± 0.64	15.45 ± 0.44
510583858	2.417	1.09 ± 0.06	0.66	0.88 ± 0.18	29.31 ± 2.88	16.47 ± 1.40
511451385	2.37	1.46 ± 0.05	1.55	0.63 ± 0.16	6.35 ± 0.14	–
511025693	3.256	1.07 ± 0.13	0.63	1.78 ± 0.30	61.76 ± 4.65	–
5100997733	3.003	1.72 ± 0.14	2.82	1.14 ± 0.30	20.44 ± 1.48	–
511228062	3.354	1.53 ± 0.05	1.82	1.10 ± 0.43	29.72 ± 2.20	–
5101001604	3.157	2.00 ± 0.03	5.37	0.83 ± 0.37	7.93 ± 0.27	–
510996058	2.493	1.88 ± 0.06	4.07	0.17 ± 0.04	3.60 ± 0.28	5.31 ± 0.79
511001501	2.227	1.41 ± 0.09	1.38	0.47 ± 0.09	18.99 ± 3.23	14.00 ± 0.29
530053714	2.436	0.97 ± 0.05	0.50	0.43 ± 0.16	14.53 ± 0.26	11.18 ± 0.64

Note: SFRs obtained with the SED fitting (Llerena et al., 2023).

Table 3.4: CANDELS/SHARD galaxies used in this thesis.

Galaxy ID	z	$\log(SFR_{SED})$ $[\mathrm{M_\odot\ yr^{-1}}]$	$L_{[CII]}$ $[10^8\,\mathrm{L_\odot}]$	$L_{[OIII]}$ $[10^8\,\mathrm{L_\odot}]$	$L_{H\alpha}$ $[10^8\,\mathrm{L_\odot}]$
889	2.754	2.08	6.46	170.42	–
902	3.501	1.76	3.09	–	303.82
908	3.49	2.14	7.41	301.54	–
920	5.048	2.2	8.51	724.00	–
1068	6.254	2.49	16.59	–	1.75
1225	4.209	3.3	107.15	–	9.76
2181	5.294	1.37	1.26	809.58	–
2350	4.26	2.26	9.77	12.25	–
2403	4.146	1.79	3.31	–	71.65
5286	2.658	1.74	2.95	–	156.36
6512	5.461	2.45	15.14	–	47.23
8489	2.737	2.65	23.99	–	4.26
8767	2.507	1.08	0.65	–	135.63
11774	2.967	1.95	4.79	–	204.06
15580	4.89	3.3	107.15	–	7.19
15801	3.1255	2.06	6.17	231.35	–
15808	3.239	2.13	7.24	5.73	–
16380	3.6538	2.81	34.67	3.54	–
24256	4.058	2.31	10.96	18.11	–
24619	2.952	2.77	31.62	201.58	–
25048	4.993	2.58	20.42	–	209.54

Note: SFRs for all galaxies in the catalog using the SFR ladder method, which is based on a combination of UV and IR SFR tracers (Barro et al., 2019).

Chapter 4

Results

In this chapter, I will illustrate the main results of my Thesis work. In the first part of this chapter, I will present the CLOUDY models, and in particular the differences between those that include binaries vs. those that do not consider that type of stars. In the second part, I will show that the models reproduce observed quantities and, finally, I will provide predictions regarding the expected luminosity of UV and optical lines in the ALPINE sample.

4.1 Spectral analysis

In *Chapter* 2, I have introduced the two main spectral synthesis codes that I used for my Thesis work: BPASS and SB99. I am seeking to determine the importance of including binaries in a stellar population when making predictions about emission lines for galaxies. As reported in Stanway & Eldridge (2018), the evolution of very massive stars ($M_\star > 100\,\mathrm{M}_\odot$) may be crucial to fully understanding aspects of early galaxies. Closed binaries, which are unable to evolve independently, are typically composed of a compact object (e.g. a white dwarf) and a more massive star (e.g. a red giant). The mass transfer between the two stars can cause the emission of extreme ultraviolet radiation from the accretion disk that forms around the smaller star, thus increasing the emission below the Lyman break. In Figure 2.4, it is evident that including binary stars in the models becomes increasingly important as the age of the stellar population increases, particularly in the case of a spectrum generated by an instantaneous burst. The explanation is connected to the duration of a star's main-sequence phase, which is directly related to its mass scaling as $\tau_{MS} \propto M^{-2.5}$ (Hansen & Kawaler, 1994; Stanway & Eldridge, 2018). Once the instantaneous burst has ended, a stellar population begins to age and to become redder. However, the presence of binaries slows down this process as they emit EUV photons for a longer time. In particular, as time passes, stellar population stars can form new closed binary systems.

In my Thesis, I have looked at the impact of binary stars in the case of a continuous SFR. The spectra from my models are shown in figure 4.1.

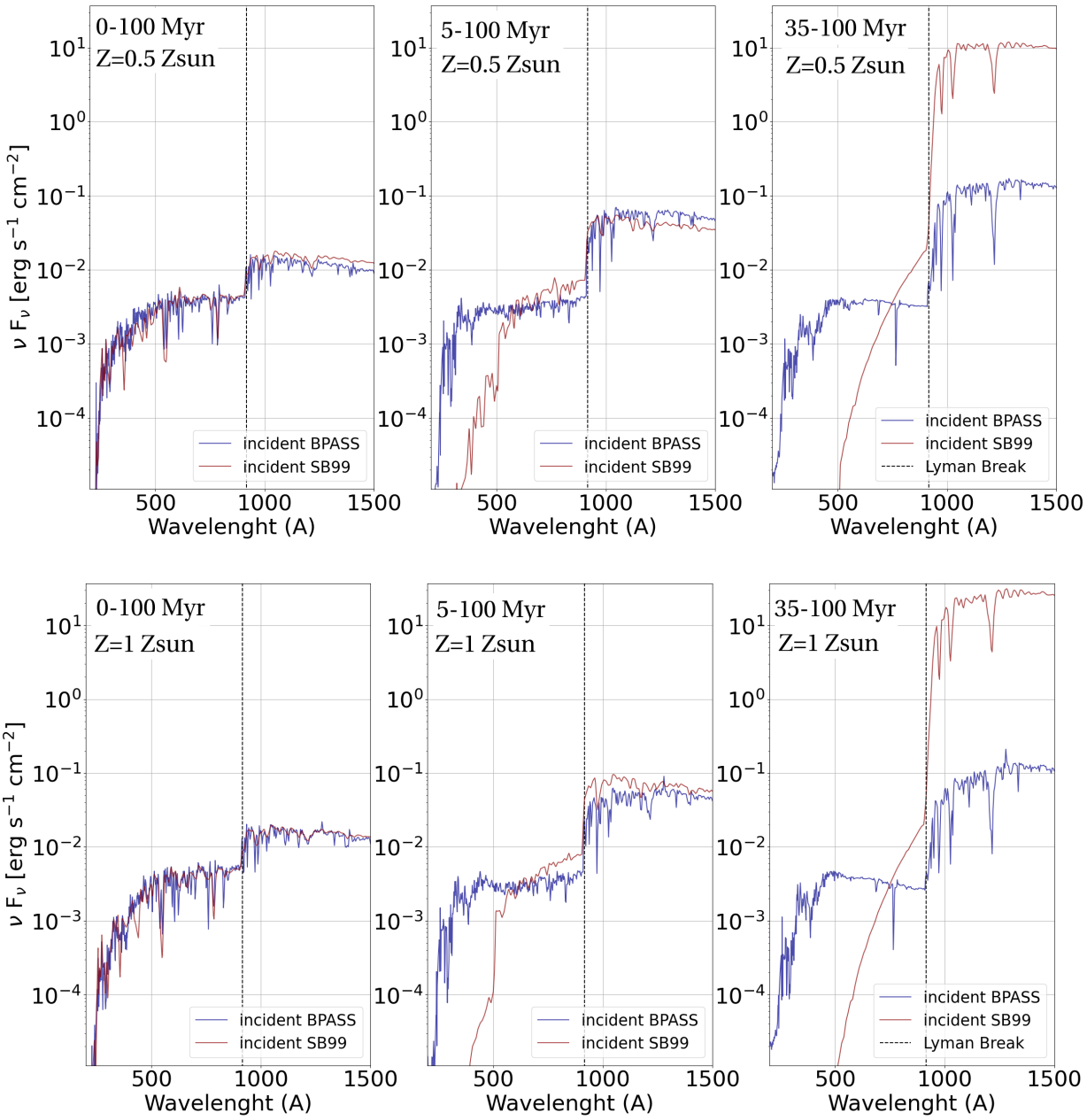

Figure 4.1: The incident spectra for the CLOUDY models. The three upper plots are obtained for stellar metallicity $Z = 0.5\mathrm{Z}_{\odot}$, while the lower row is obtained assuming $Z = \mathrm{Z}_{\odot}$. The plots are arranged from left to right assuming that the continuous star formation is ongoing (left), quenched $5\,\mathrm{Myr}$ ago (middle) or $35\,\mathrm{Myr}$ ago (right). The star formation is assumed continuous and to have started $100\,\mathrm{Myr}$ ago, with SFR$= 1\,\mathrm{M}_{\odot}\,\mathrm{yr}^{-1}$. The blue lines represent the SED from BPASS while the red lines those from SB99.

It is clear from the Figure that, in the case of continuous SFR and observing a relatively young stellar population ($\sim 100\,\mathrm{Myr}$), the impact of binary stars in the total spectrum is negligible (see left plots Figure 4.1). The SF in this case is never-quenched, which can be considered the explanation for this result. Both stellar populations are producing new, young stars that emit in the EUV. Therefore, binary stars have a minimal effect on EUV emission compared to the emission from young stars.

If the star formation is quenched, we instead observe a variation in the total EUV budget produced with BPASS vs. SB99. It is evident that the spectra show a dramatic increase in the difference as the age of star formation quenching increases (see the central and right plots in Figure 4.1). This suggests that binary stars play a significant role in keeping EUV ($\lambda < 912\mathring{A}$) emission high. In a single stellar population without binary stars, the end of star formation results in all stars becoming older, which leads to a decrease in emission below the Lyman break and an increase in emission after the Lyman break. This process is slowed down when binaries are included in the modelling. The metallicity of the spectra (see upper and lower plots Figure 4.1) has the effect of making all the spectra redder, as expected from the emission of metal-rich stars (Hansen & Kawaler, 1994).

The different SEDs affect the transition from the HII region to the PDR. This is shown in Figure 4.2, where we can see the free-electron temperature as a function of the hydrogen column density within the gas slab. We define the HII to PDR transition the layer where the electron temperature drops from $T_e = 10000\,K$ to $T_e = 100\,K$ (see *Section* 1.1). In case of continuous SFR without quenching, the HII regions approximately have the same total column density and temperature. When SF is quenched, we can observe that the emission from binary stars increases the size and temperature of the HII region compared to a stellar population without binaries.

We further note that, as the metallicity increases, the temperature and size of the HII region decrease (the upper models have a lower metallicity than the lower models, as seen in Figure 4.2). This is due to the more efficient cooling induced by the presence of metals.

In Figure 4.3*(left panel)* it is evident that density has a minor effect on the size of the HII region, slightly increasing it for higher values. Additionally, the PDR outer temperature is higher at lower densities. This is in reality connected mainly to the ionisation parameter definition (see Eq.1.3). The ionisation parameter is closely linked to n, so if we keep U constant and raise n, the flux of ionising photons will also increase. This is why in my models there is not a significant dependence on density. Viceversa, as seen in Figure 4.3*(right panel)*, increasing the ionisation parameter significantly enlarges the size of the HII region, which affects the PDR component of my CLOUDY models, which stops at a hydrogen column density of approximately $N_H = 10^{22}\,\mathrm{cm}^{-2}$. Generally, for densities that are higher, and especially for U increasing, my models show a decrease in the flux of lines such as [CII] which are indicators of PDR, and an increase in the flux of UV emission lines that are markers of HII regions.

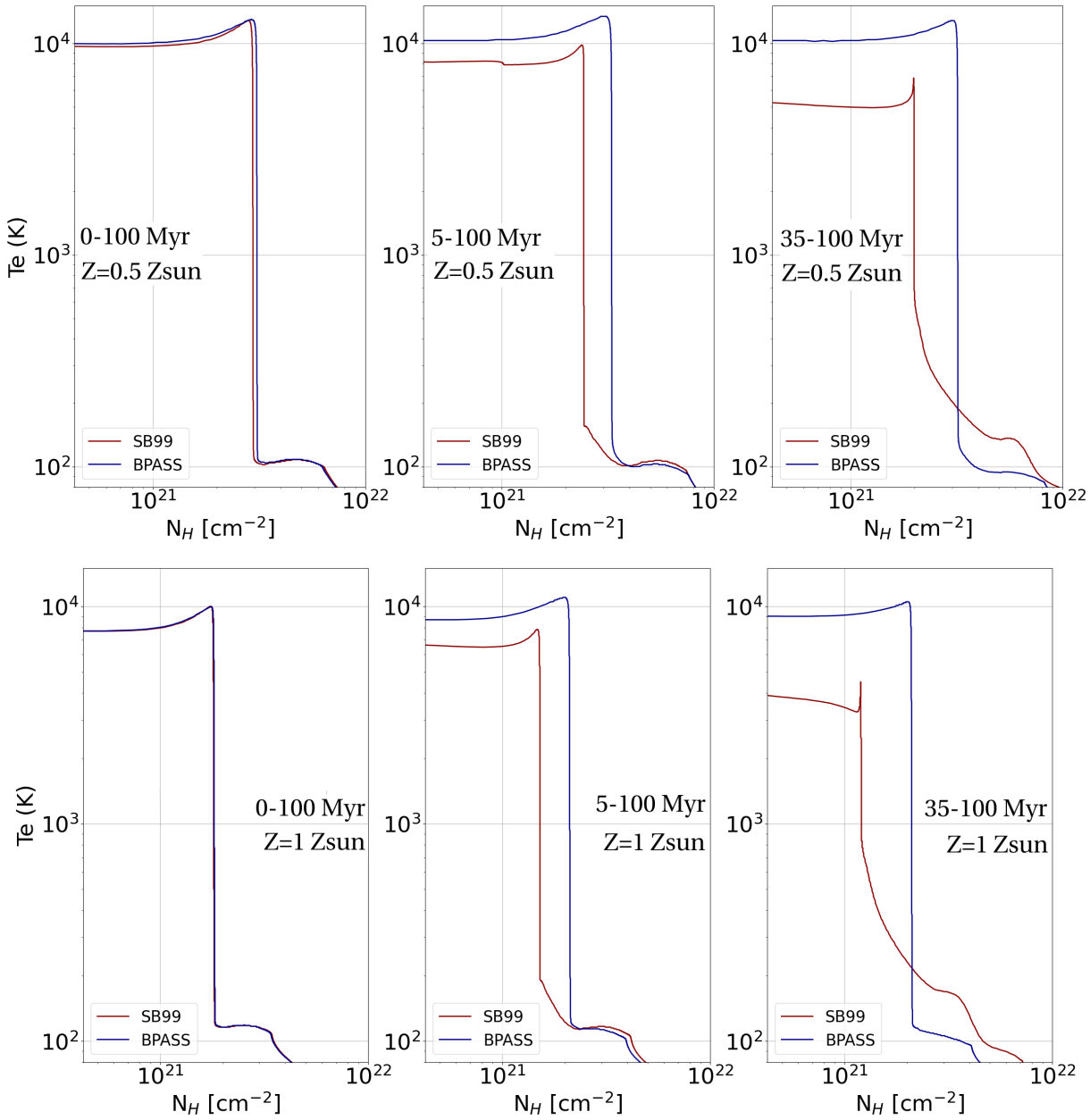

Figure 4.2: The free electron temperature in function of hydrogen column density for the CLOUDY models [$U = -1$, $log(n_H) = 2$ and $Z = 0.55\,\mathrm{Z}_\odot$ (upper models) / $Z = 1.05\,\mathrm{Z}_\odot$ (lower models)]. The three upper plots are obtained for stellar metallicity $Z = 0.5\mathrm{Z}_\odot$, while the lower row is obtained assuming $Z = \mathrm{Z}_\odot$. The plots are arranged from left to right assuming that the continuous star formation is ongoing (left), quenched $5\,\mathrm{Myr}$ ago (middle) or $35\,\mathrm{Myr}$ ago (right). The star formation is assumed continuous and to have started $100\,\mathrm{Myr}$ ago, with SFR$= 1\,\mathrm{M}_\odot\,\mathrm{yr}^{-1}$. The blue lines represent the SED from BPASS while the red lines those from SB99.

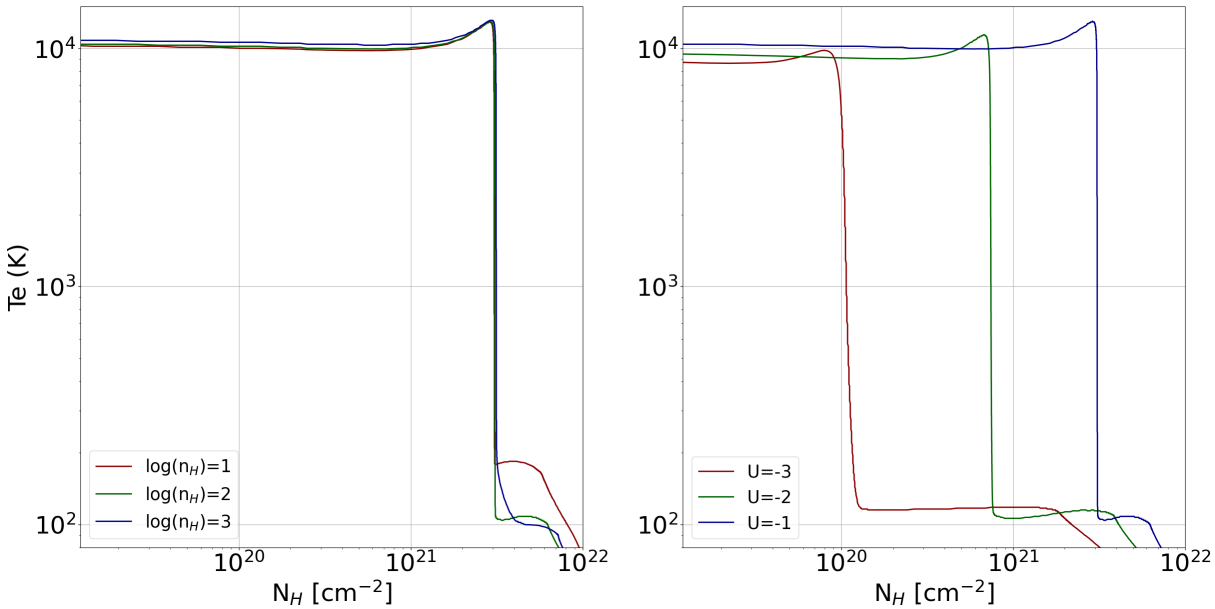

Figure 4.3: (left panel) The free electron temperature in function of hydrogen column density for the CLOUDY models with three different density values ($log(n_H) = 1, 2, 3$, respectively red, green, and blue) and fixed $U = -1$ and $Z = 0.55\,Z_\odot$. The plot is related to a SED produced by a stellar population of metallicity $Z \sim 0.5\,Z_\odot$. It is a BPASS spectra model without any quenching in SF. (right panel) Free-electron temperature as a function of the hydrogen column density for the CLOUDY models with three different ionisation parameter values ($U = -3, -2, -1$, respectively red, green, and blue) and fixed $log(n_H) = 2$ and $Z = 0.55\,Z_\odot$. The plot is related to a SED produced by a stellar population of metallicity $Z \sim 0.5\,Z_\odot$. It is a BPASS spectra model without any quenching in SF.

4.2 Model analysis

In this section, I will analyse the results of my models, particularly those with a SED shape generated by a stellar metallicity $Z \sim 0.5\,Z_\odot$ that is the typical value of the gas metallicity in the ALPINE sample (Burgarella et al., 2022). Additionally, as can be seen in Figure 4.1, the differences in the SED shape between a solar and sub-solar stellar population are negligible in the EUV.

For the initial analysis, I will show the density fraction plots related to the chemical elements of the emissions that are relevant for my Thesis: hydrogen, carbon, oxygen, and nitrogen. All these plots are arranged from left to right according to the time of quenching: never quenched, $5\,\mathrm{Myr}$ and $35\,\mathrm{Myr}$ ago.

In Figure 4.4, is visible the fraction density of neutral and ionised hydrogen as function of the hydrogen column density of the gas slab. It is evident where the transition occurs between the HII region and the PDR. We observe a decrease in ionised hydrogen and a corresponding increase in neutral hydrogen. This transition corresponds in terms of hydrogen column density at the point in which we observe a cut-off in free electrons temperatures, as visible in Figure 4.2. In fact, the ionising temperature of hydrogen is

around $\sim 10000\,\mathrm{K}$, below it the neutral hydrogen fraction starts to rise. In the case of models with quenched star formation, SB99 models produces a transition that occurs at lower N_H.

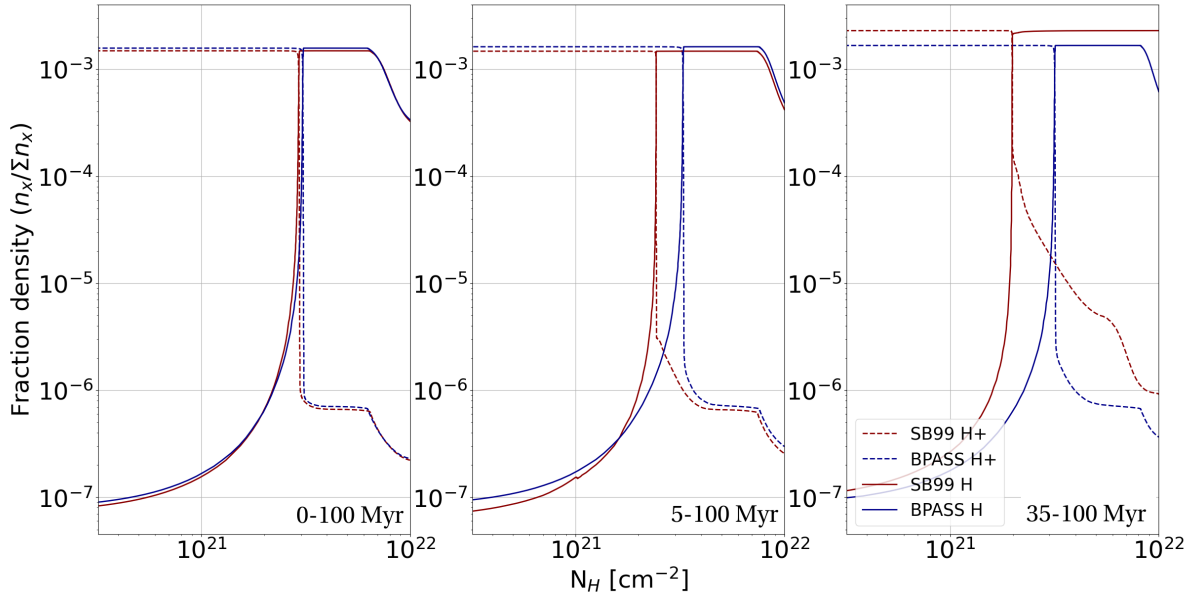

Figure 4.4: The neutral and ionised hydrogen fraction density in function of N_H for the CLOUDY model $U = -1$, $log(n_H) = 2$ and $Z = 0.55\,\mathrm{Z}_\odot$. All the plots are for $Z_{sp} \sim 0.5\,\mathrm{Z}_\odot$. The plots are arranged from left to right according to the time of quenching: never quenched, $5\,\mathrm{Myr}$ and $35\,\mathrm{Myr}$ ago. Red lines are SB99 models, blue lines BPASS models.

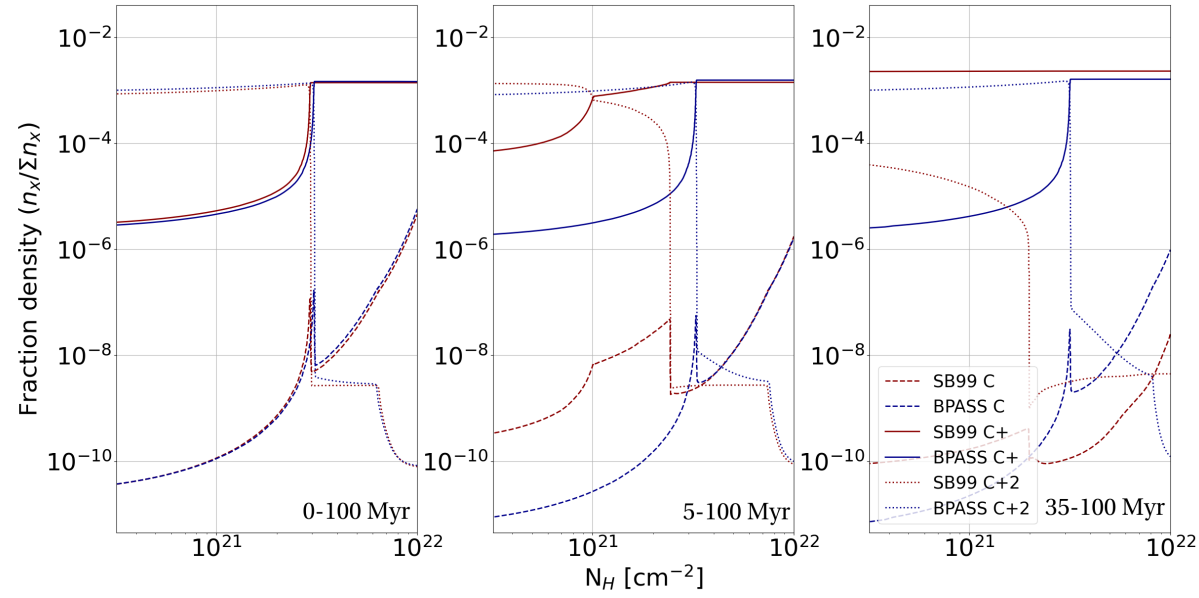

Figure 4.5: The C^0,C^+ and C^{2+} fraction density in function of N_H for the CLOUDY model $U = -1$, $log(n_H) = 2$ and $Z = 0.55\,\mathrm{Z}_\odot$. All the plots are for $Z_{sp} \sim 0.5\,\mathrm{Z}_\odot$. The plots are arranged from left to right according to the time of quenching: never quenched, $5\,\mathrm{Myr}$ and $35\,\mathrm{Myr}$ ago. Red lines are SB99 models, blue lines BPASS models.

In Figure 4.5 I plot the density fractions for C^0, C^+ (the C ionisation potential is $11.26\,\mathrm{eV}$) and C^{2+} (the C^+ ionisation potential is $24.45\,\mathrm{eV}$). At the transition between the HII region and the PDR, there is a decrease in C^{2+} and an increase in C^+. This is caused by the lower ionisation potential of C than that of hydrogen. On the other hand, the ionisation potential of C^+ is higher than that of hydrogen, so C^{2+} is more abundant in regions where EUV photons are present (HII regions). We observe an increase in C^+ at lower values of hydrogen column density in SB9 models with quenched SF. This is due to the lower amount of EUV photons (see Figure 4.1) that are able to produce C^{2+}. The neutral carbon increases in any case as the hydrogen column density increases, as a result of the decrease in the number of ionising photons.

A similar behaviour to that described for carbon is associated to oxygen, see Figure 4.6. The differences are mainly due to the different ionisation potentials of the oxygen species with respect to carbon species. The O^0 has an ionisation potential of $13.618\,\mathrm{eV}$ and O^+ of $35.1\,\mathrm{eV}$.

Finally, in Figure 4.7 I plot the fraction density for neutral and ionised nitrogen (the N^0 ionisation potential is $29.6\,\mathrm{eV}$). It is evident that, in the case of non-quenched star formation, the amount of N^0 increases at the transition between the HII and PDR, whereas the amount of N^+ decreases. In the case of quenched SF, SB99 models show an increase in ionised nitrogen in HII regions, which is contrary to the prediction of a smaller quantity of EUV photons in non-binary stellar population models. This can be explained by the fact that we are seeing a decrease in multiple ionised nitrogen species, which is raising the proportion of single-ionised nitrogen. This is further corroborated by the fact that in these models we are witnessing an increase in neutral nitrogen in the HII regions, which suggests a smaller amount of ionising photons emitted by the spectra.

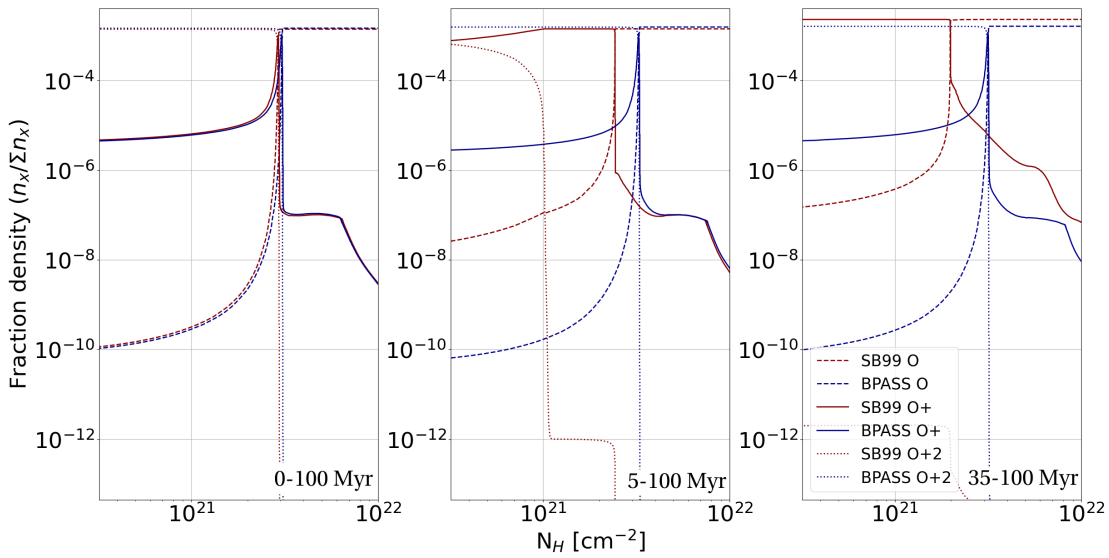

Figure 4.6: The O^0,O^+ and O^{2+} fraction density in function of N_H for the CLOUDY model $U = -1$, $log(n_H) = 2$ and $Z = 0.55\,\mathrm{Z}_\odot$. All the plots are for $Z_{sp} \sim 0.5\,\mathrm{Z}_\odot$. The plots are arranged from left to right according to the time of quenching: never quenched, $5\,\mathrm{Myr}$ and $35\,\mathrm{Myr}$ ago. Red lines are SB99 models, blue lines BPASS models.

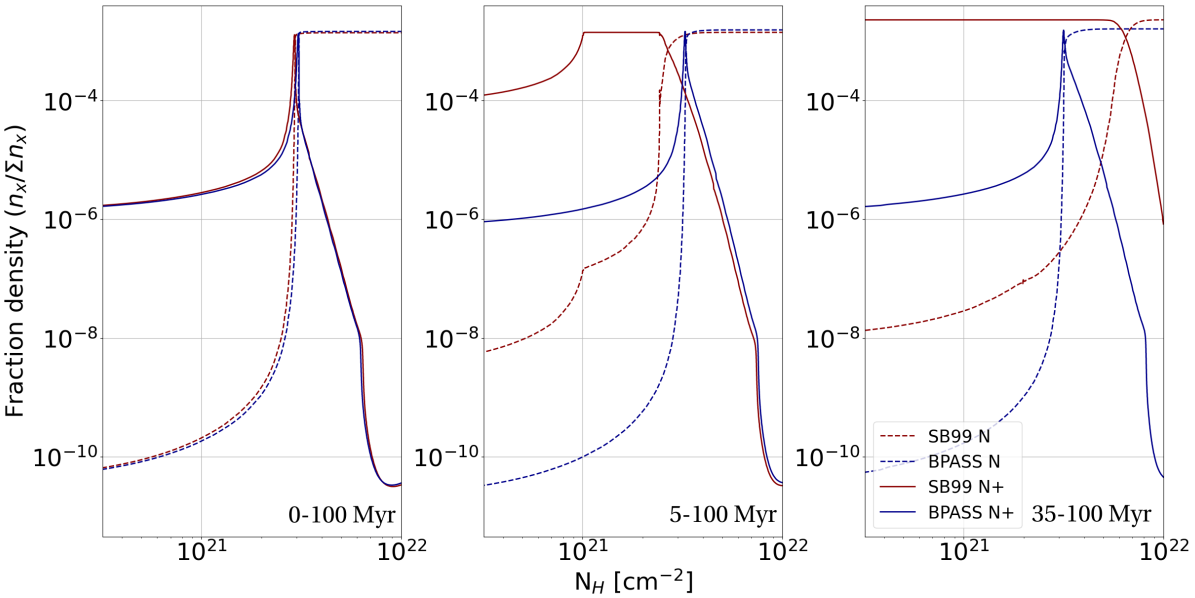

Figure 4.7: The N^0 and N^+ fraction density in function of hydrogen column density for the CLOUDY model $U = -1$, $log(n_H) = 2$ and $Z = 0.55\,Z_\odot$. All the plots are for $Z_{sp} \sim 0.5\,Z_\odot$. The plots are arranged from left to right according to the time of quenching: never quenched, $5\,\mathrm{Myr}$ and $35\,\mathrm{Myr}$ ago. Red lines are SB99 models, blue lines BPASS models.

4.2.1 CIII] 1909$\mathring{A}$

The CIII] $1909\mathring{A}$ is an UV line tracing ionised gas phase (see *Section* 1.2.1 for details). The line will be compared with the [CII] 158μm in order to clarify the potential synergy between the UV and optical lines observed by JWST and the FIR line detected by ALMA. In Figure 4.8, the cumulative flux of the [CII] emission line is plotted as a function of N_H. From left to right, I reported models with different quenching ages. In the left plot, the difference between models with and without binary stars is negligible, which is consistent with the small differences in the spectra discussed in *Section* 4.1 for the case of no quenching in SF. However, if the SF quenched 5 or 35 Myr ago, it is evident that the SB99 models have an increase in [CII] emission line flux at lower values of hydrogen column density. This is closely related to the ionisation potential of carbon and the fact that the spectra of SB99 models are less hard than those of the BPASS models in this case. Therefore, we expect that the HII regions in the case of a softer spectrum will be thinner (see *Section* 4.2), and indeed the [CII] emission, which is a tracer of the PDR, indicates a PDR region that begins at lower values of hydrogen column density.

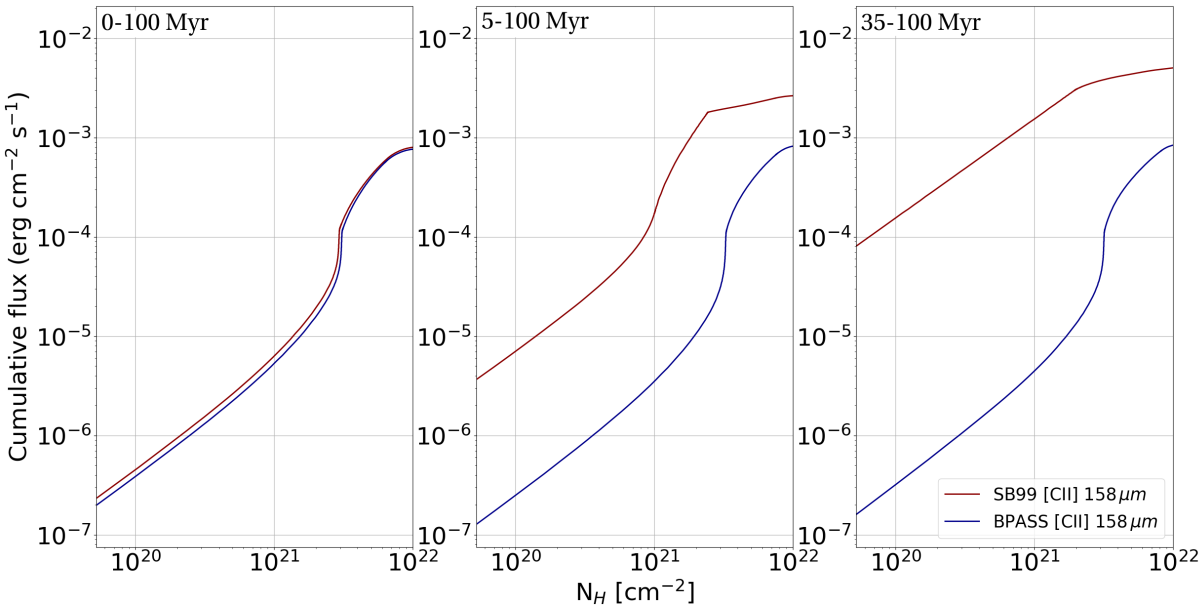

Figure 4.8: The cumulative flux of [CII] emission as a function of hydrogen column density for a CLOUDY model with $U = -1$, $log(n_H) = 2$ and $Z = 0.55\,Z_\odot$. The plots are arranged from left to right in accordance with the time frame in which we observe a quenching in star formation: never quenched, $5\,$Myr and $35\,$Myr ago. The red line is related to SB99 model, the blue line to BPASS model.

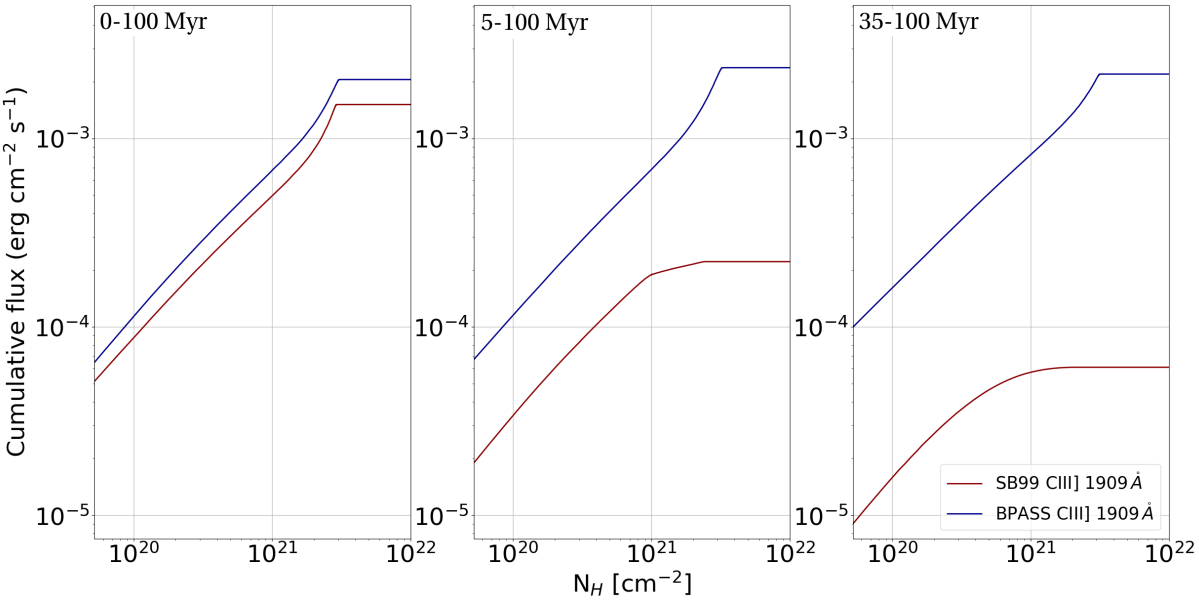

Figure 4.9: The cumulative flux of CIII] emission as a function of hydrogen column density for a CLOUDY model with $U = -1$, $log(n_H) = 2$ and $Z = 0.55\,Z_\odot$. The plots are arranged from left to right according to the time of quenching: never quenched, $5\,\mathrm{Myr}$ and $35\,\mathrm{Myr}$ ago. Red lines are SB99 models, blue lines BPASS models.

In Figure 4.9 I plot the cumulative flux of CIII] emission as a function of N_H. The UV line has a behaviour that is the opposite of [CII]. In this case, the cumulative emission remains constant for all three BPASS models due to the presence of binary stars, which keep the spectra harder. On the other hand, the SB99 models have softer spectra that reduce the emission in the gas cloud, resulting in a significant decrease in cumulative emission for the models with quenching in SF, obviously associated with a thinner HII regions. It is noteworthy that even in the case without quenching in SF, the binaries cause a harder spectrum compared to SB99 models; thus, the CIII] emission is higher in this case as well.

Finally, I plotted the contour plots for the CIII]/[CII] ratio as a function of hydrogen density and the ionisation parameter of my CLOUDY models, with a fixed metallicity of $Z = 0.55\,Z_\odot$. The flux of the emission lines was taken at the highest value of the hydrogen column density of my CLOUDY models ($N_H = 10^{22}\,\mathrm{cm}^{-2}$) to take all the flux emitted by the gas cloud. This is a good choice for HII region emission lines, since the peak of emission is usually reached at lower values of hydrogen column density (see, e.g., Figure 4.9). However, for the [CII] emission line, this may lead to an underestimation of the emission, since the peak is usually reached in PDRs at $N_H > 10^{22}$. It is evident that the ratio of CIII] to [CII] increases with increasing density and in particular the ionisation parameter. This cannot be attributed to the different critical densities of CIII] and [CII]. According to Lagache et al. (2018), the critical density for excitation of [CII] by collisions with neutral hydrogen atoms is $n_{crit_H} \sim 1300\,\mathrm{cm}^{-3}$. The critical density for the excitation of CIII] by collisions with free electrons in the HII region is $n_{ce}(CIII]1909\mathring{A}) \sim 10^{10}\,\mathrm{cm}^{-3}$ (Le Fèvre et al., 2019).

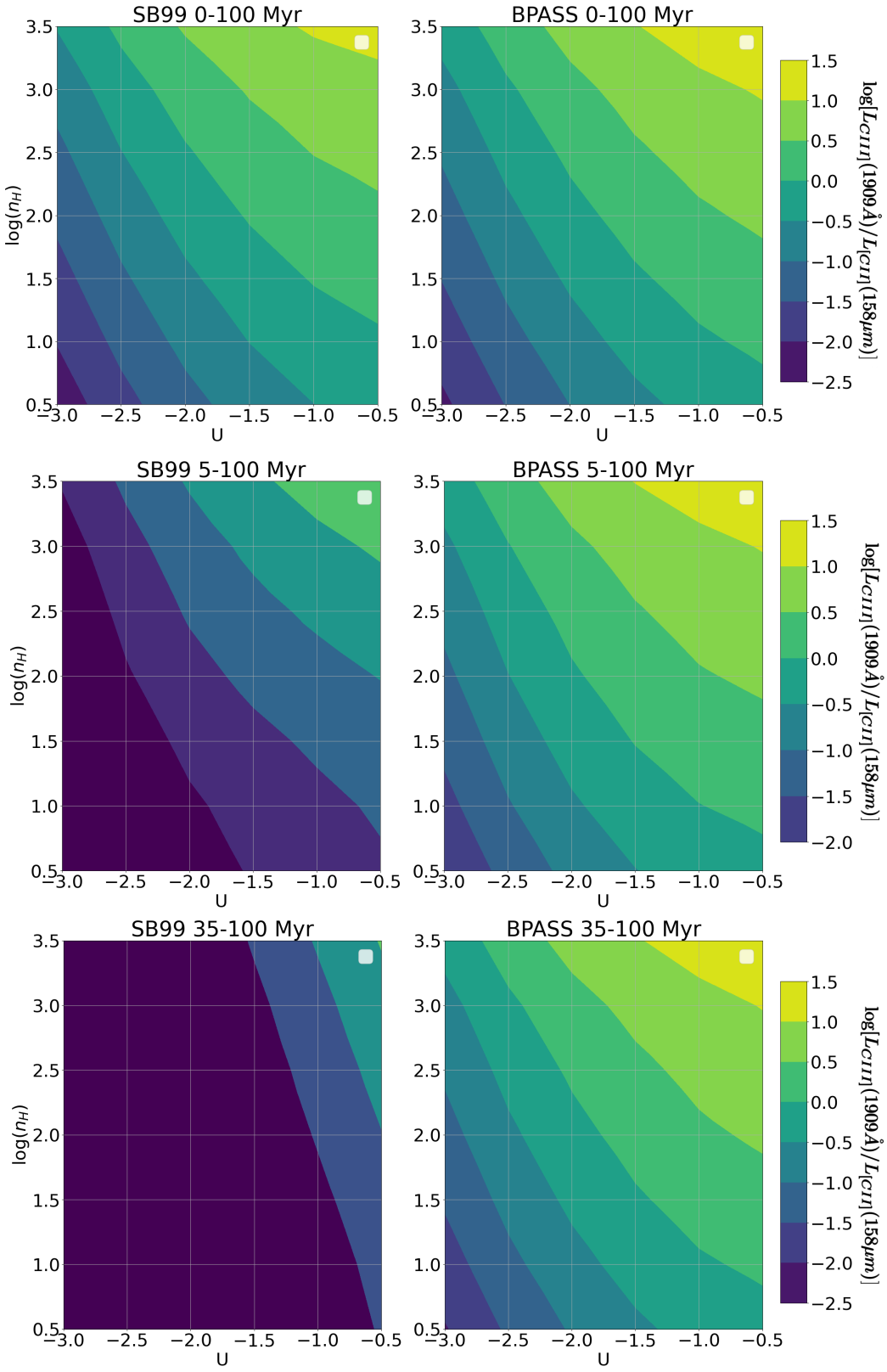

Figure 4.10: Contour plots of log(CIII]/[CII]) flux, as a function of hydrogen density and ionisation parameter, with a fixed metallicity of $Z = 0.55\,\mathrm{Z}_{\odot}$. The left plots are related to the SB99 models, the right plots to the BPASS models. The plots are arranged from up to down in accordance with the time frame in which we observe a quenching in star formation: never quenched, $5\,\mathrm{Myr}$ and $35\,\mathrm{Myr}$ ago.

This implies that both [CII] and CIII] emission are affected by both the temperature and density of the gas. The behaviour can be attributed to the increase in the temperature of the PDR when the density increases and the widening of the HII region when U increases, as discussed in *Section* 4.1. Then, the emission of the UV lines increases and the flux of [CII] decreases, because the HII region is increasing but I always take the flux at the same value of $N_H \sim 10^{22}\,\mathrm{cm}^{-2}$.The PDR is moving to higher values of N_H, resulting in the peak of the [CII] emission being reached deeper into the gas slab. In the case of quenching in SF, the ratio remains constant for the BPASS models, while it decreases significantly for the SB99 models, as can be seen in Figures 4.8 and 4.9. This can be explained by the fact that the SB99 spectra are softer in respect to BPASS spectra, and so we have a decrease in terms of UV emission line fluxes.

4.2.2 [OIII] 5007$\mathring{A}$

In Figure 4.11, the cumulative flux of the [OIII] emission is shown as a function of N_H. As expected, due to the ionisation potential of O^+ being much higher than that of hydrogen ($\sim 35.1\,\mathrm{eV}$ and $\sim 13.6\,\mathrm{eV}$ respectively, as discussed in *Section* 1.2.1), the emission for the SB99 models is lower than that of the BPASS models.

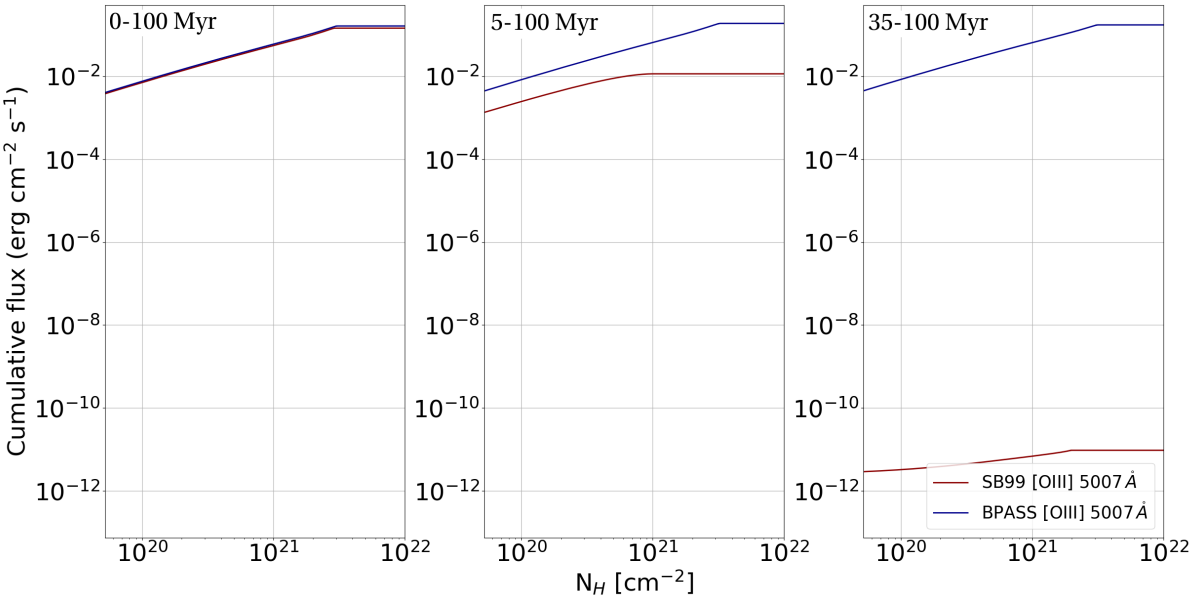

Figure 4.11: The cumulative flux of [OIII] emission as a function of hydrogen column density for a CLOUDY model with $U = -1$, $log(n_H) = 2$ and $Z = 0.55\,\mathrm{Z}_\odot$. The plots are arranged from left to right according to the time of quenching: never quenched, $5\,\mathrm{Myr}$ and $35\,\mathrm{Myr}$ ago. Red lines are SB99 models, blue lines BPASS models.

The contour plots for the [OIII]/[CII] ratio as a function of hydrogen density and ionisation parameter are presented in Figure 4.12, with a fixed metallicity of $Z = 0.55\,\mathrm{Z}_\odot$. The flux of the emission lines was taken at the highest value of the hydrogen column density of the CLOUDY models ($N_H = 10^{22}\,\mathrm{cm}^{-2}$) to capture all the flux emitted by the gas cloud (see *Section* 4.2.1). This behaviour is similar to the one reported in *Section* 4.2.1, with the critical density for [OIII] being $n_{ce}([OIII]\,5007\mathring{A}) \sim 10^{5.85}\,\mathrm{cm}^{-3}$ (Baskin & Laor, 2005). The same pattern is also visible in the quenched SF models, where

the decrease in [OIII] emission flux is more pronounced in the models with the oldest quenching. The $35\,\mathrm{Myr}$ ago quenching model is not represented in the form of contour plots, as the ratio only reaches values close to zero (approximately 10^{-10}).

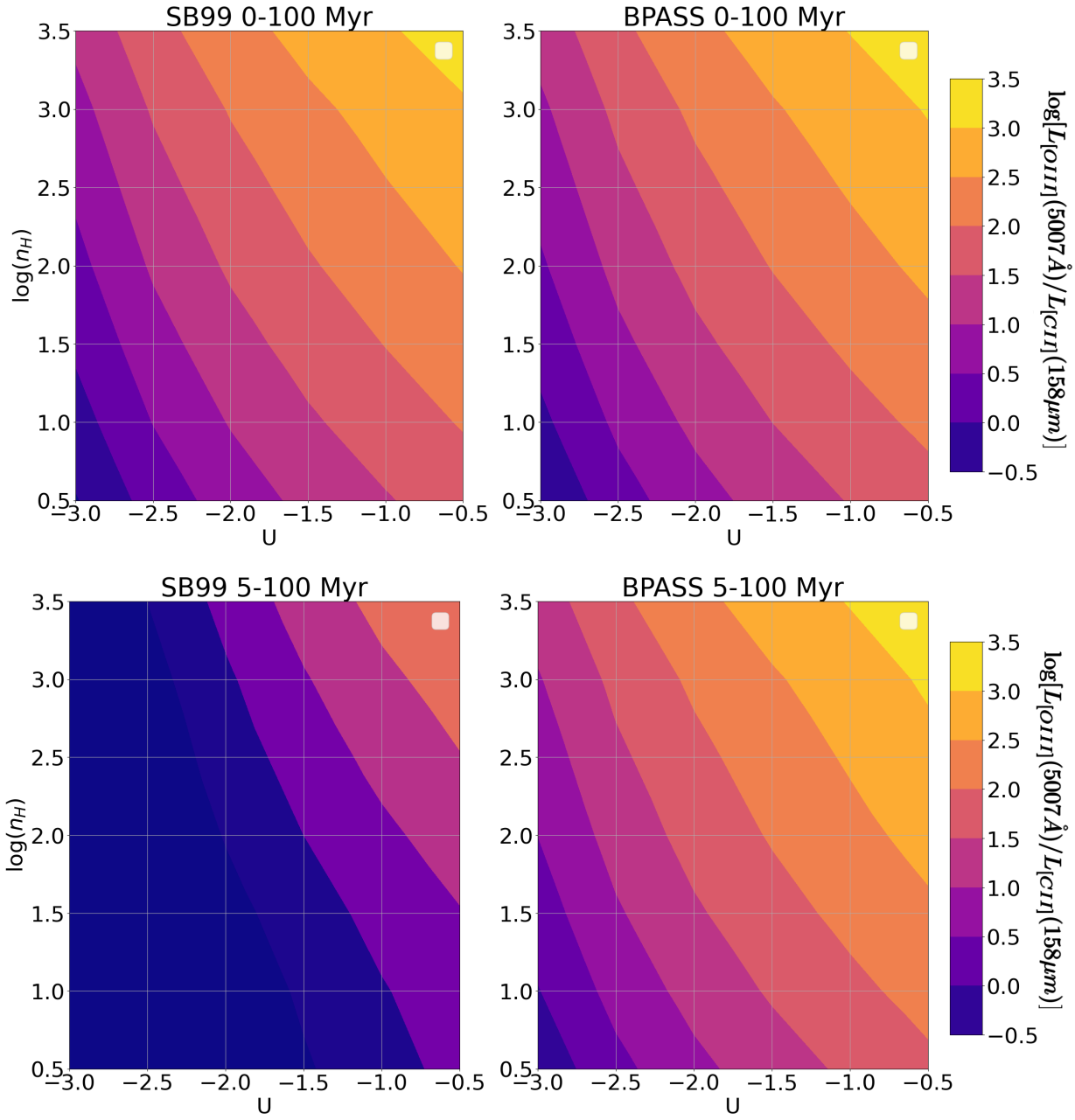

Figure 4.12: Contour plots of log([OIII]/[CII]) flux, as a function of hydrogen density and ionisation parameter, with a fixed metallicity of $Z = 0.55\,\mathrm{Z}_{\odot}$. The left plots are related to the SB99 models, the right plots to the BPASS models. The plots are arranged from up to down in accordance with the time frame in which we observe a quenching in star formation: never quenched and $5\,\mathrm{Myr}$ ago.

4.2.3 Hα 6563$\mathring{A}$

The $H\alpha$ $6563\mathring{A}$ is an important tracer of star formation in a galaxy (see *Section* 1.1.1 for a detailed explanation). In Figure 4.13, the cumulative flux of the $H\alpha$ emission is

shown as a function of N_H. The SB99 models demonstrate an increase in the emission of this line in the quenched star formation cases. This is because the emission line $H\alpha$ is usually caused by the excitation of energetic levels of hydrogen by FUV radiation (which is below the energy of hydrogen ionisation). Therefore, this emission is usually higher in the case of softer spectra and thus in the case of a quenched SF for SB99 models. Moreover, as we have already observed in *Section* 4.1, the free electron temperature of the quenched SB99 models is lower than the typical hydrogen ionisation temperature ($\sim 10000\,\mathrm{K}$), resulting in more neutral hydrogen that can be excited in comparison to the BPASS models.

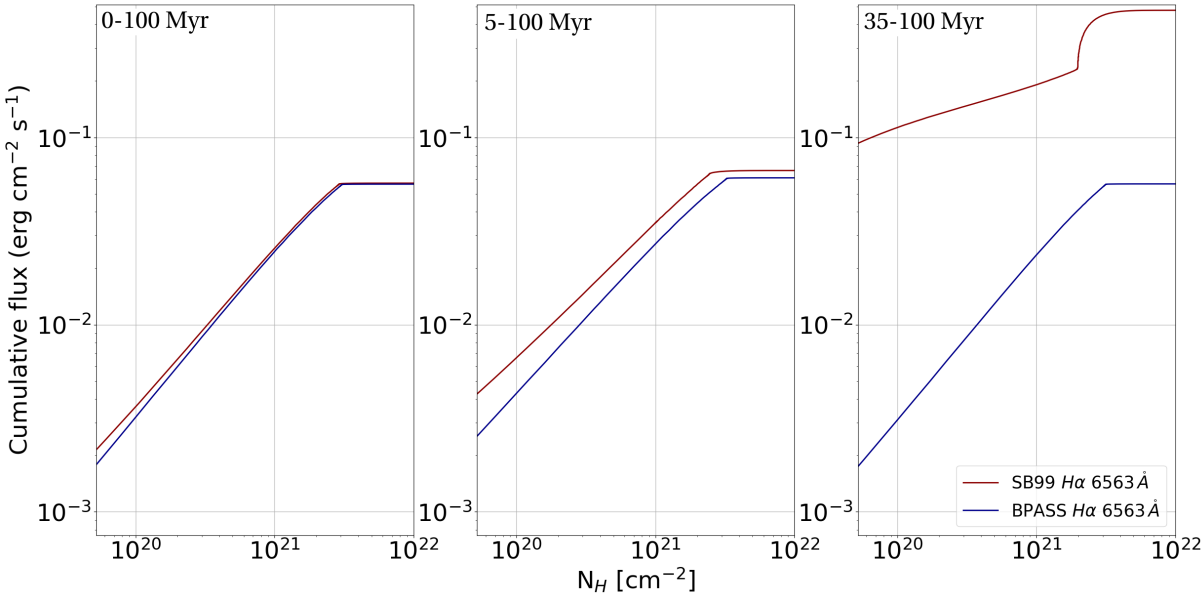

Figure 4.13: The cumulative flux of $H\alpha$ emission as a function of hydrogen column density for a CLOUDY model with $U = -1$, $log(n_H) = 2$ and $Z = 0.55\,\mathrm{Z}_\odot$. The plots are arranged from left to right according to the time of quenching: never quenched, $5\,\mathrm{Myr}$ and $35\,\mathrm{Myr}$ ago. Red lines are SB99 models, blue lines BPASS models.

The contour plots in Figure 4.12, with a fixed metallicity of $Z = 0.55\,\mathrm{Z}_\odot$, show that the $H\alpha$/[CII] ratio increases with increasing density and ionisation parameter. This behaviour is similar to that described in *Sections* 4.2.2 and 4.2.1. The critical density of $H\alpha$ is $n_{ce}(H\alpha\,6563\mathring{A}) \sim 10^{8-9}\,\mathrm{cm}^{-3}$ (Tielens, 2005). However, we observe a different behaviour for $H\alpha$ in quenched SF models, with a general increase in terms of emission for the SB99 models. This is because, as explained in the cumulative plot in Figure 4.13, SB99 models have more FUV photons and more neutral hydrogen than the BPASS models, resulting in a general increase in flux emission.

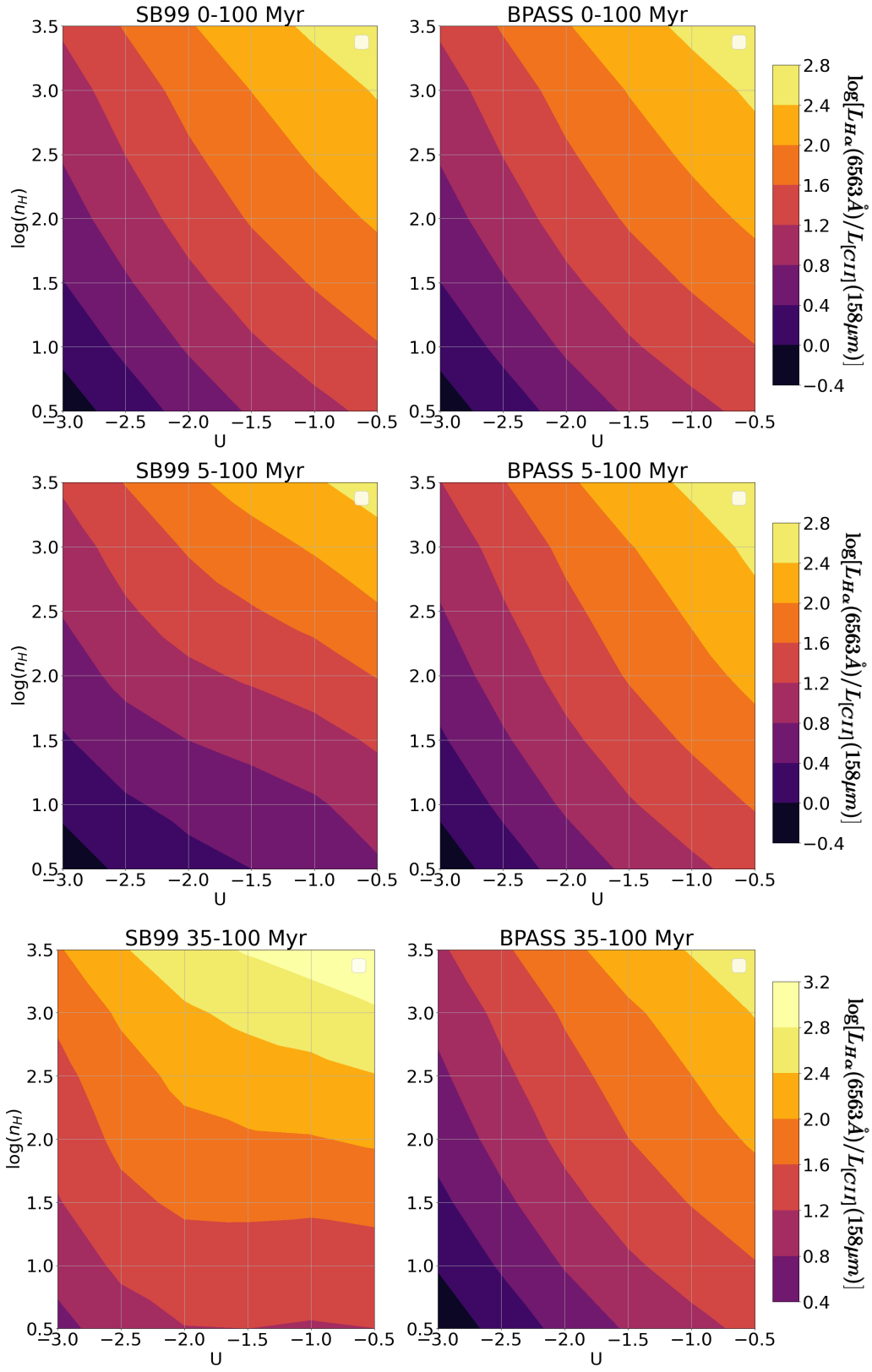

Figure 4.14: Contour plots of log($H\alpha$/[CII]) flux, as a function of hydrogen density and ionisation parameter, with a fixed metallicity of $Z = 0.55\,\mathrm{Z}_{\odot}$. The left plots are related to the SB99 models, the right plots to the BPASS models. The plots are arranged from up to down in accordance with the time frame in which we observe a quenching in star formation: never quenched, $5\,\mathrm{Myr}$ and $35\,\mathrm{Myr}$ ago.

4.2.4 [NII] 6583$\mathring{A}$

The [NII] $6583\mathring{A}$ is an emission line used for the measurement of the electron density in the gas around an AGN or in regions forming stars (see *Section* 1.2.1 for a detailed explanation). In Figure 4.15, the cumulative flux of [NII] emission is shown as a function of N_H. We observe that in the case of quenching SF, the emission initially increases for the SB99 case, but is reduced in the case of an older quenching in SF. This is because we are dealing with an emission from a first ionisation species (N^0 ionisation energy $29.6\,\mathrm{eV}$), unlike the cases seen in *Sections* 4.2.1 and 4.2.2. We can understand this behaviour by considering the trends in nitrogen ionisation discussed in *Section* 4.2: the increase of [NII] is caused by the reduction of the [NIII] emission due to the SB99 spectra, which are softer than the BPASS spectra.

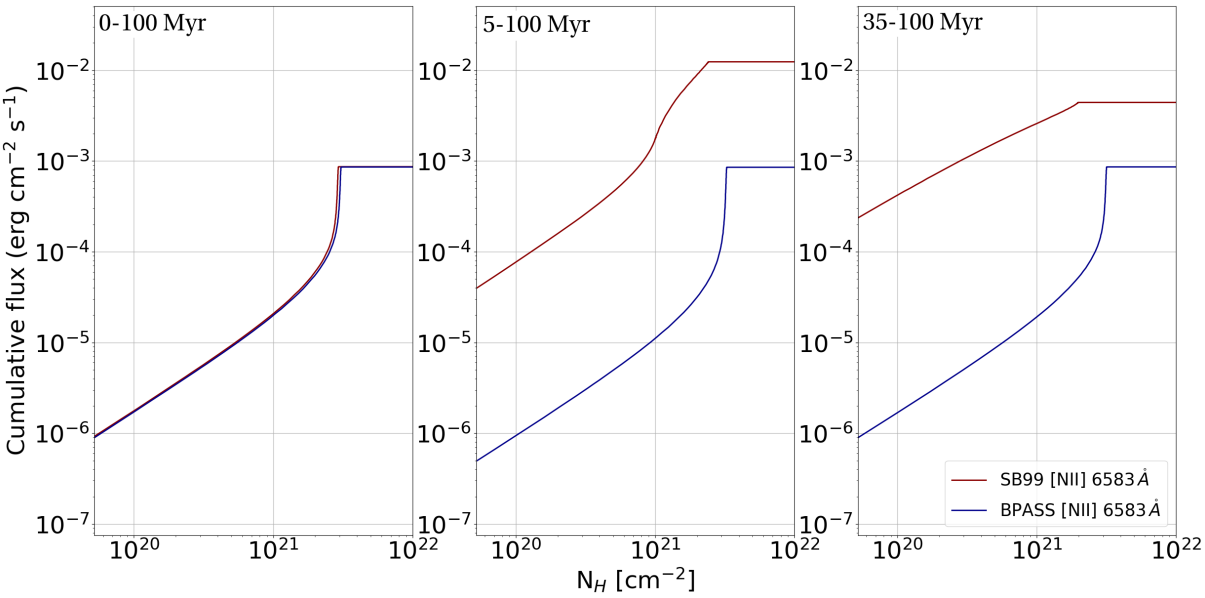

Figure 4.15: The cumulative flux of [NII] emission as a function of hydrogen column density for a CLOUDY model with $U = -1$, $log(n_H) = 2$ and $Z = 0.55\,\mathrm{Z}_\odot$. The plots are arranged from left to right according to the time of quenching: never quenched, $5\,\mathrm{Myr}$ and $35\,\mathrm{Myr}$ ago. Red lines are SB99 models, blue lines BPASS models.

The contour plots in Figure 4.16, with a fixed metallicity of $Z = 0.55\,\mathrm{Z}_\odot$, show that the [NII]/[CII] ratio increases with increasing density but is less influenced by U variations. The critical density of [NII] is $n_{ce}([NII]\,6583\mathring{A}) \sim 6.6 \times 10^4\,\mathrm{cm}^{-3}$. The [NII] emission line, as seen in Figure 4.7, is associated with the presence of singly ionised nitrogen. If we look at the figure 4.17, we see that with an increase in U, we have an increase of N^{2+}, while the quantity of N^+ is almost constant. The fact that an increase in U is not associated with a reduction in N^+ density is the explanation for the behaviour of [NII] emission. However, this change in the case of a softer spectrum, and in fact we start to observe a behaviour similar to the one observed in the [OIII] and CIII] case for the SB99 quenching SF cases. This is connected to the reduction of EUV photons in the SB99 models.

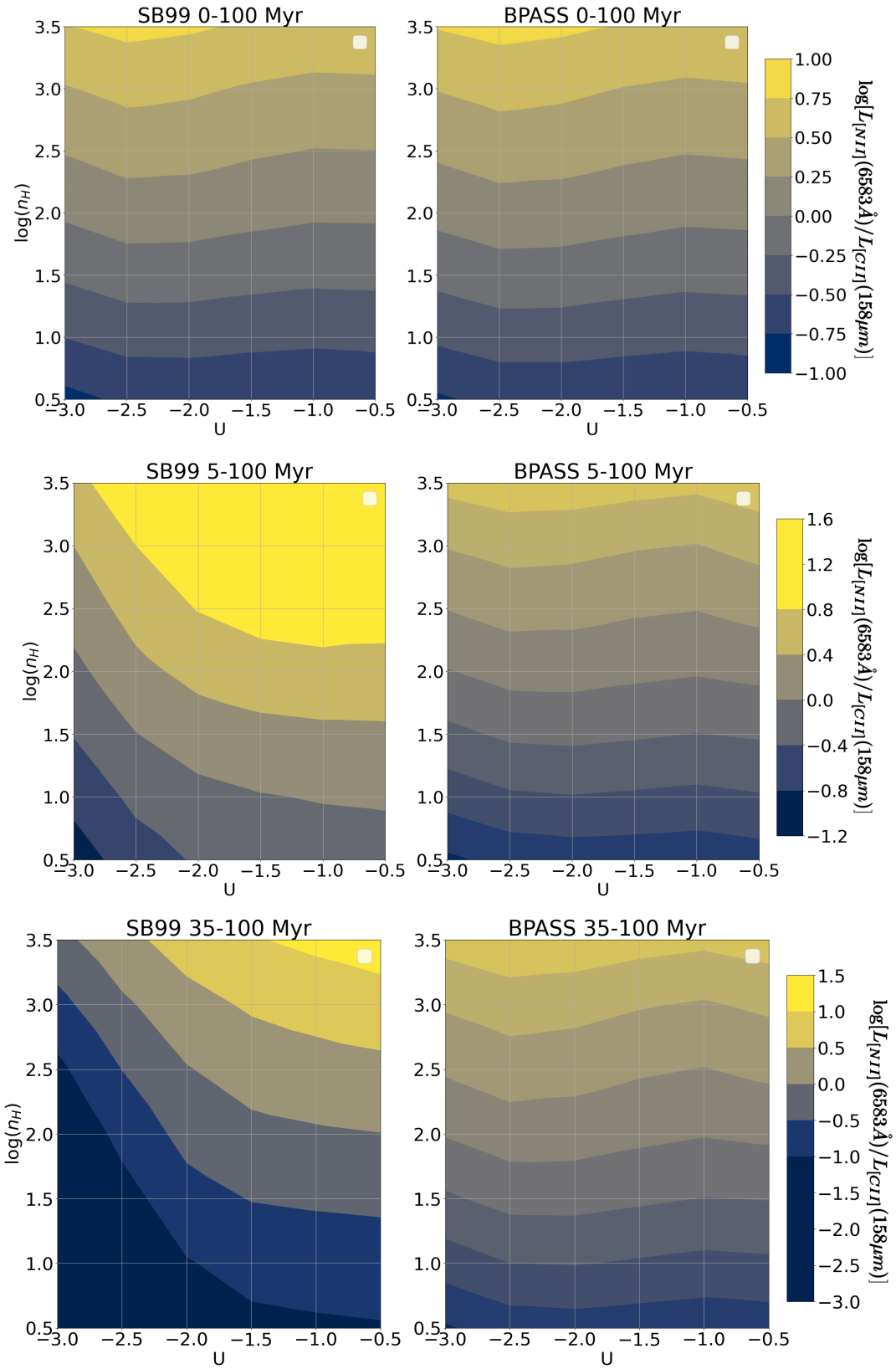

Figure 4.16: Contour plots of log([NII]/[CII]) flux, as a function of hydrogen density and ionisation parameter, with a fixed metallicity of $Z = 0.55\,\mathrm{Z}_{\odot}$. The left plots are related to the SB99 models, the right plots to the BPASS models. The plots are arranged from up to down in accordance with the time frame in which we observe a quenching in star formation: never quenched, $5\,\mathrm{Myr}$ and $35\,\mathrm{Myr}$ ago.

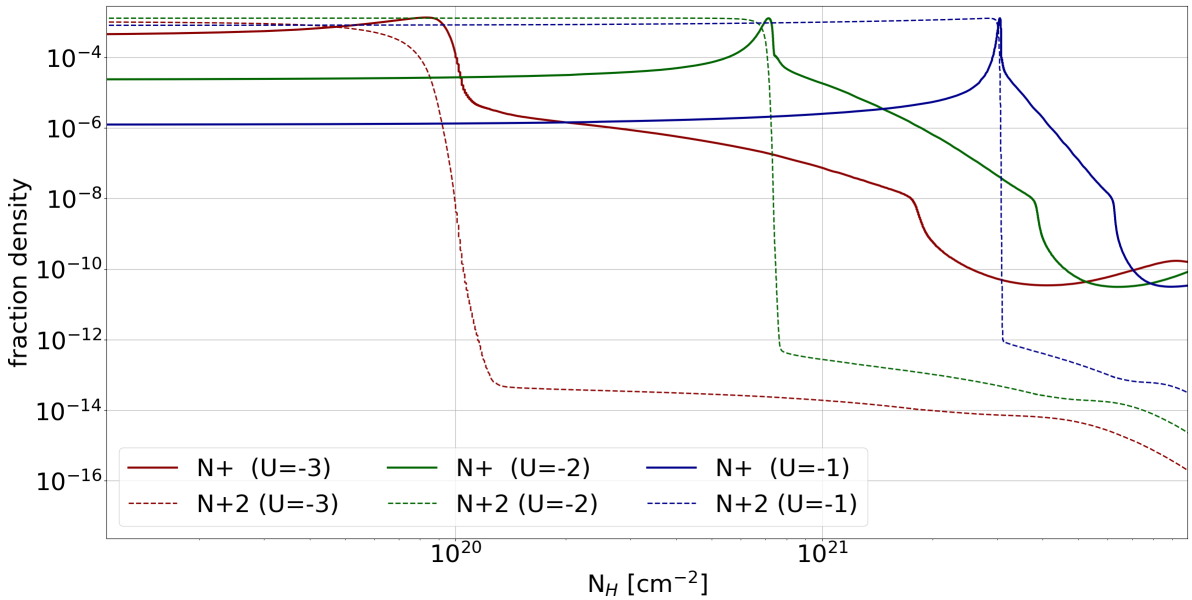

Figure 4.17: The fraction density of N^{+} and N^{2+} in function of hydrogen column density for the CLOUDY models with three different ionisation parameter values ($U = -3, -2, -1$, respectively red, green, and blue) and fixed $log(n_H) = 2$ and $Z = 0.55\,Z_{\odot}$. The plot is related to a SED produced by a stellar population of metallicity $Z \sim 0.5\,Z_{\odot}$. It is a BPASS spectra model without any quenching in SF.

4.3 Model validation

Before making any predictions for the ALPINE sample, I have used the datasets described in *Sections* 3.2 and 3.3 to assess whether the CLOUDY models that I have developed can reproduce the observed data. In particular, I have collected data for galaxies with the highest possible redshift ($2.5 < z < 3.5$), to test the model at redshift as close as possible to the ALPINE ones. The available observational data are the luminosities of the CIII],[OIII] and $H\alpha$ emission lines and the associated SFR values for each galaxy. In this section, I will use both the SB99 and BPASS models to examine the case of a continuous star formation without quenching.

Figure 4.18 shows the CIII] emission line predicted with my models for fixed values of $log(n_H)$ and Z, depending on the observed SFR. The left plots are from SB99, while the right plots are from BPASS. The ratio of the luminosity of CIII] to [CII] is considered at $N_H = 10^{22}\,\mathrm{cm}^{-2}$. The values of U are computed from the SFR values, using the equations reported in *Section* 3.2. We can appreciate that, in general, spanning the density values from $log(n_H) = 1$ to $log(n_H) = 2$ allows me to reproduce almost all the observation data from the VANDELS and VUDS datasets (*Section* 3.2). Generally, as the metallicity increases, the SFR values associated with a given $L_{CIII]}$ also increase due to the presence of more metals, and thus a more efficient radiative cooling of the gas (*Section* 1.2.1), leading to the collapse of GMCs into new stars. In Figure 4.21, the ratio of luminosity of CIII] to [CII] is considered in this case for a hydrogen column density lower than in the other graphs, $N_H = 10^{21}\,\mathrm{cm}^{-2}$. It is evident that reducing N_H allows a better representation of the points with lower SFR values. This can be explained by considering that lowering the column density N_H means reducing the PDR layer, where the [CII] luminosity is produced. Moreover, this can be attributed to the fact that galaxies with low star formation rates are usually small in size and thus have a relatively small value of N_H for the size of the photodissociation region. I report the prediction of low column density ($N_H \sim 10^{21}\,\mathrm{cm}^{-2}$) that could represent also a particular line of sight poor of gas and dust.

Figures 4.19 and 4.22 show the [OIII] luminosity, while Figures 4.20 and 4.23 display the $H\alpha$ luminosity. The data presented in these figures are also taken from the datasets described in *Section* 3.3. The models can reproduce the data as previously seen for the CIII] luminosity. However, it is evident that the model fails to accurately depict galaxies with relatively higher SFR values, but this may be an indication that the stellar populations are metal-rich with respect to the others.

In conclusion, the validation results suggest that the models are able to reproduce the observed trend for reasonable assumption of physical parameters in the analysed galaxies. This is particulary true for the SFR range of the ALPINE galaxies, and so I can make predictions for these ones assuming that the model is able to make good predictions.

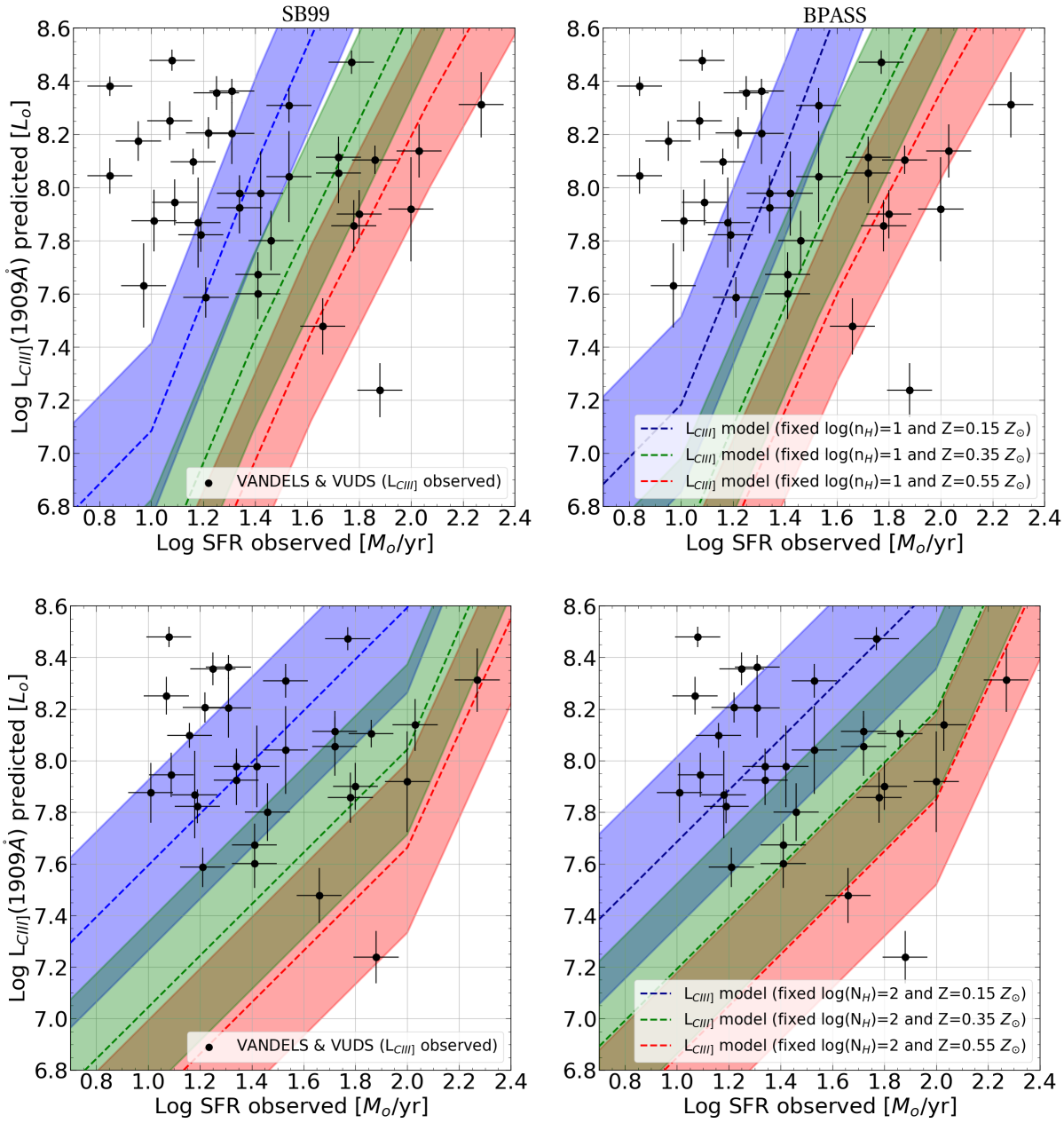

Figure 4.18: The predicted values of $L_{CIII]}$ as a function of SFR for $N_H = 10^{22}\,\mathrm{cm}^{-2}$. The black points are the observed values from the VANDELS & VUDS dataset. The blue, green and red bands are the predicted values with fixed $Z = 0.15, 0.35, 0.55$ respectively. The upper panels are related to models with fixed $log(n_H) = 1$, the lower panels with fixed $log(n_H) = 2$. The left panels are the SB99 models, the right panels the BPASS models. All the models are for continuos SF without quenching.

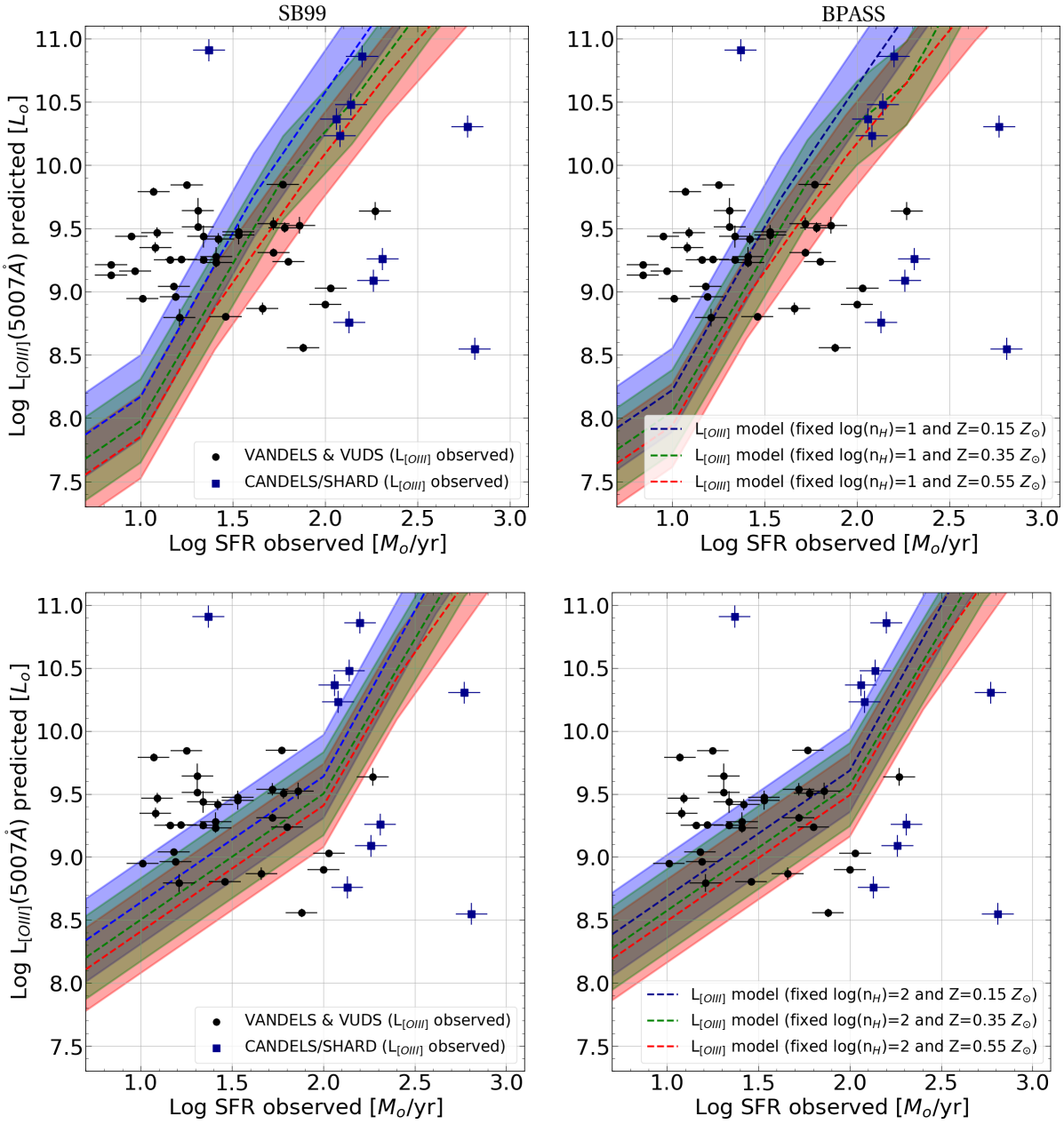

Figure 4.19: The predicted values of $L_{[OIII]}$ as a function of SFR for $N_H = 10^{22}\,\mathrm{cm}^{-2}$. The black circle points are the values from the VANDELS & VUDS dataset, whereas the blue square points are the values from the CANDELS/SHARDS dataset. The blue, green and red bands are the predicted values with fixed $Z = 0.15, 0.35, 0.55$ respectively. The upper panels are related to models with fixed $log(n_H) = 1$, the lower panels with fixed $log(n_H) = 2$. The left panels are the SB99 models, the right panels the BPASS models. All the models are for continuos SF without quenching.

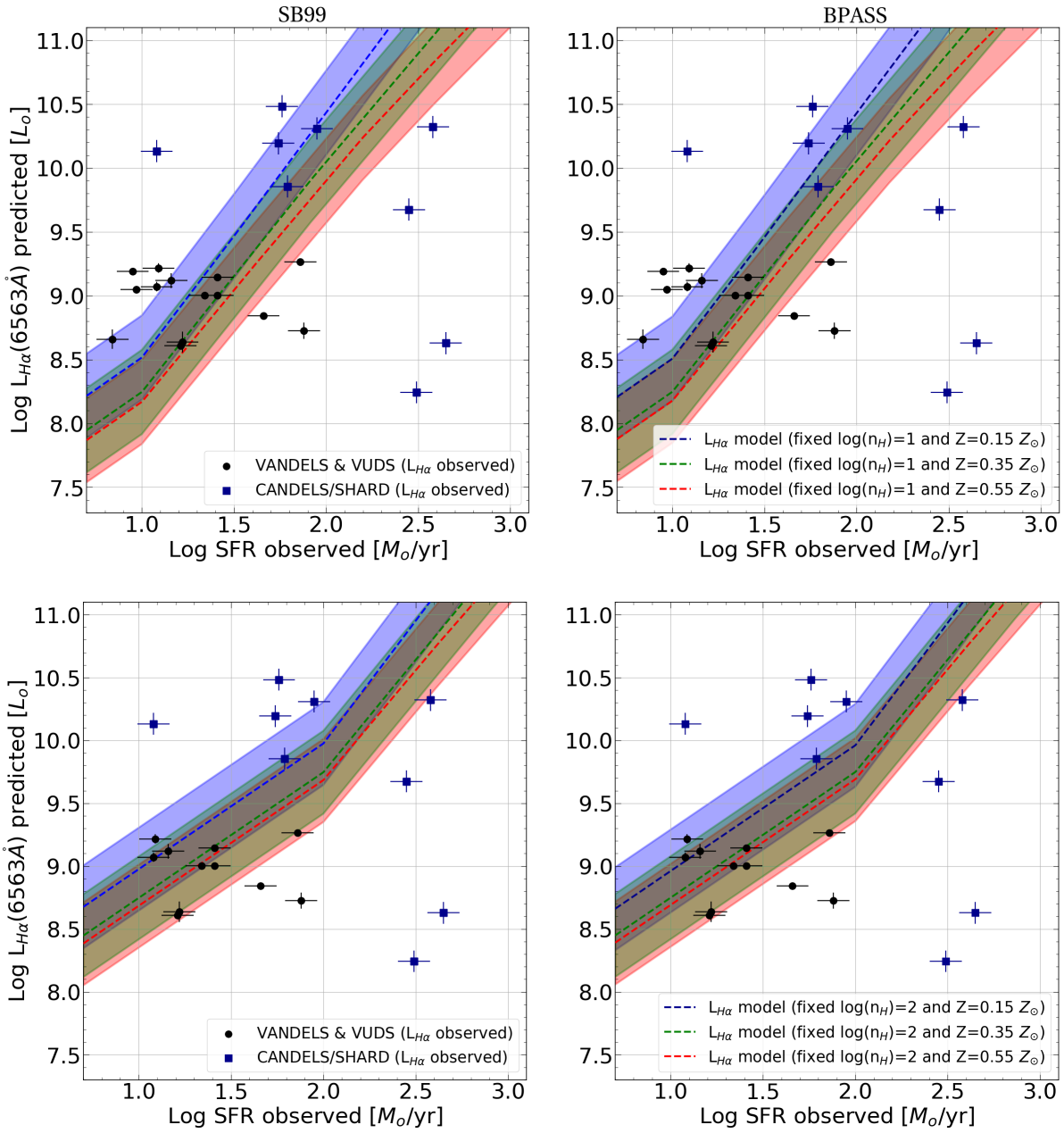

Figure 4.20: The predicted values of $L_{H\alpha}$ as a function of SFR for $N_H = 10^{22}\,\mathrm{cm}^{-2}$. The black circle points are the values from the VANDELS & VUDS dataset, whereas the blue square points are the values from the CANDELS/SHARDS dataset. The blue, green and red bands are the predicted values with fixed $Z = 0.15, 0.35, 0.55$ respectively. The upper panels are related to models with fixed $log(n_H) = 1$, the lower panels with fixed $log(n_H) = 2$. The left panels are the SB99 models, the right panels the BPASS models. All the models are for continuos SF without quenching.

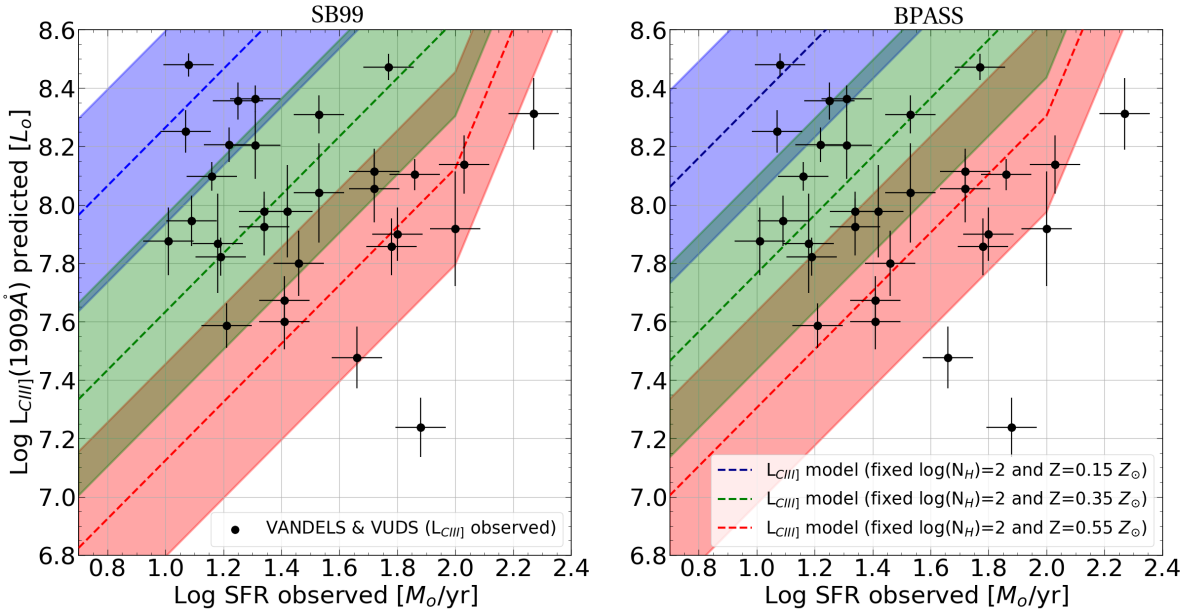

Figure 4.21: The predicted values of $L_{CIII]}$ as a function of SFR for $N_H = 10^{21}\,\mathrm{cm}^{-2}$. The black points are the values from the VANDELS & VUDS dataset. The blue, green and red bands are the predicted values with fixed $Z = 0.15, 0.35, 0.55$ respectively. The hydrogen density is fixed at $log(n_H) = 2$. The left panels are the SB99 models, the right panels the BPASS models. All the models are for continuos SF without quenching.

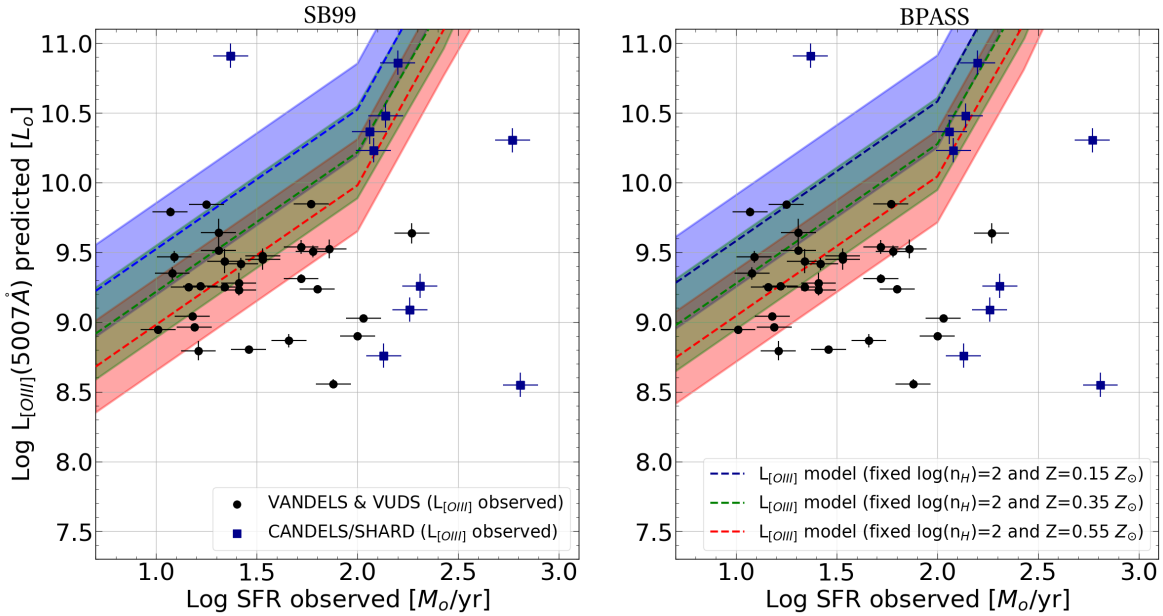

Figure 4.22: The predicted values of $L_{[OIII]}$ as a function of SFR for $N_H = 10^{21}\,\mathrm{cm}^{-2}$. The black points are the values from the VANDELS & VUDS dataset, whereas the blue square points are the values from the CANDELS/SHARDS dataset. The blue, green and red bands are the predicted values with fixed $Z = 0.15, 0.35, 0.55$ respectively. The hydrogen density is fixed at $log(n_H) = 2$. The left panels are the SB99 models, the right panels the BPASS models. All the models are for continuos SF without quenching.

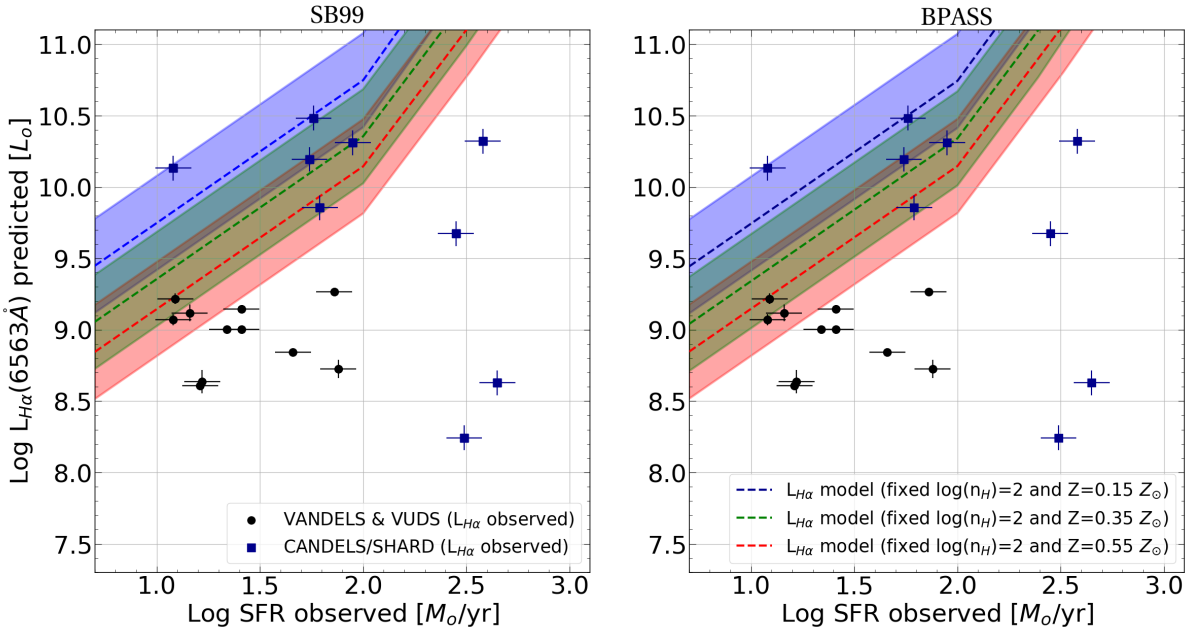

Figure 4.23: The predicted values of $L_{H\alpha}$ as a function of SFR for $N_H = 10^{21}\,\mathrm{cm}^{-2}$. The black points are the values from the VANDELS & VUDS dataset, whereas the blue square points are the values from the CANDELS/SHARDS dataset. The blue, green and red bands are the predicted values with fixed $Z = 0.15, 0.35, 0.55$ respectively. The hydrogen density is fixed at $log(n_H) = 2$. The left panels are the SB99 models, the right panels the BPASS models. All the models are for continuos SF without quenching.

4.4 ALPINE theoretical predictions

In this Section, I discuss the predictions for the ALPINE galaxies related to the CIII] $1909\AA$, [OIII] $5007\AA$, $H\alpha$ $6563\AA$ and [NII] $6583\AA$ emission lines. I am considering models with a continuous SF without quenching because the star formation history (SFH) of ALPINE galaxies is uncertain, thus I stick to the more general case. The interested reader can find the quenched cases in *Appendix* 5.

In order to make these predictions, I have used the analytical model from Ferrara et al. (2019), described in *Section* 2.5, to obtain the set of physical parameters associated with my model: U, n, and Z. To do this, I have used the Σ_{SFR} from the ALPINE dataset and the Schmidt (1959); Kennicutt (1998) relation to obtain the corresponding $\Sigma_{[CII]}$. For the Kennicutt-Schmidt law, I have chosen three different values for the burstiness parameter k_s: $1, 5$ and 10. The fiducial value assumed for ALPINE is $k_s = 5$, as reported by (Markov et al., 2022) and (Vallini et al., 2021). Then, I take the associated ratio $R(U, n, Z)$ between the optical and UV lines with respect to the [CII] emission line, to obtain predictions from the observed $L_{[CII]}$.

In Figure 4.24, I show the predicted CIII] luminosity as a function of SFR for ALPINE galaxies. The solid black line represents the weighted linear regression performed with my predicted data using the Python packages *statsmodel* (Seabold & Perktold, 2010) and *seaborn* (Waskom, 2021). We can notice that the results from CLOUDY models

coupled with BPASS SED (right panel) are in slightly better agreement with galaxies with [CII] and CIII] joint detections at $z \sim 5$ (Markov et al., 2022) with respect to the SB99 case. This underlines the importance of binary stars in the high-redshift galaxies SED. Moreover, we observe a moderate good linear correlation between CIII] luminosity and SFR for the ALPINE sample.

In figure 4.25,4.26 and 4.27 I show instead the predictions for the [OIII], $H\alpha$ and [NII]. In all of these cases, because these lines are connected to the SF of galaxies, we observe a linear correlation with the predicted emission luminosity and the observed SFR. The best linear correlations found, in terms of the error on the angular coefficient that results from the linear fit, is visible in the case of CIII] and [NII] (respectively, a relative error of 27% and 18% for the angular coefficients). The correlation coefficients for SB99 and the BPASS model in the CIII]-SFR relation are $r = 0.549$ and $r = 0.563$, respectively. The associated p-values for the two models are $p - value \approx 0.1\%$ and $p - value \approx 0.09\%$. Regarding the [NII]-SFR relation, for the SB99 and BPASS models $r = 0.689$ and $r = 0.693$, respectively. The associated p-values for the two models are $p - value \approx 0.00033\%$ and $p - value \approx 0.00036\%$. These statistical results indicate that the preferred candidate to show a relation similar to that found by De Looze et al. (2014) for the [CII] emission in the local Universe is the [NII]-SFR relation.

If we consider the cases with SF quenching, we expected a complete different behaviour in this relations for what regards the case of no binaries in the stellar population. The behaviour will be modified because of what is already discussed in *Section* 4.2. In *Appendix* 5 are reported the predictions for ALPINE galaxies in the case of quenched SF.

Finally, I used my models to predict optical line ratios for ALPINE, and derive the expected location of ALPINE galaxies in the BPT diagram (Baldwin et al., 1981). This enables the characterisation of the dominant production mechanisms (star formation vs. black hole accretion) present in these galaxies. The BPT diagram obtained from my models is reported in Fig.4.28. We can notice that all ALPINE sources are located below the line separating AGN from Star forming galaxies. This is in agreement with expectation as AGN radiation is not implemented in my models. BPT diagrams lines are influenced by different star formation efficiency (SFE) of the galaxies, that in these models is connected to the value of the burstiness parameter k_s. For higher values of k_s, we have an higher SFE, because the galaxies are able to produce more stars from the gas. This impacts the incident radiation: more young stars implies large emission of ionising photons. The Figure 4.28 clearly demonstrates the effect of an increase in SFE on the BPT diagram: as k_s increases, the predicted values move closer to the AGN region. The presence of binaries changes the predicted location of galaxies within the BPT as shown in Figure 4.29. For the quenched SFH ($5 - 100\,\mathrm{Myr}$), the BPASS model (right panel) returns a much larger value for $\log([OIII]/H\beta)$ with respect to that from SB99 (left panel). This is due to the harder spectrum of stellar populations that include binary stars, as discussed in *Section* 4.1. In particular, in SB99, the UV photon budget drops dramatically immedieatly after the quenching, while this is not the case for BPASS where the mass accretion processes in the closed binary systems provides an additional channel for the UV photon production at older ages. In conclusion, the BPT diagram

predictions are strongly dependent on the presence of binaries in the stellar population, on the SFH, and on the SFE. Overall the BPASS case in Figure 4.28, could mimick the presence of an AGN in the BPT diagram. To obtain a complete picture of the ISM conditions in ALPINE, it could be beneficial to include AGN radiation in my CLOUDY models and test their BPT locations.

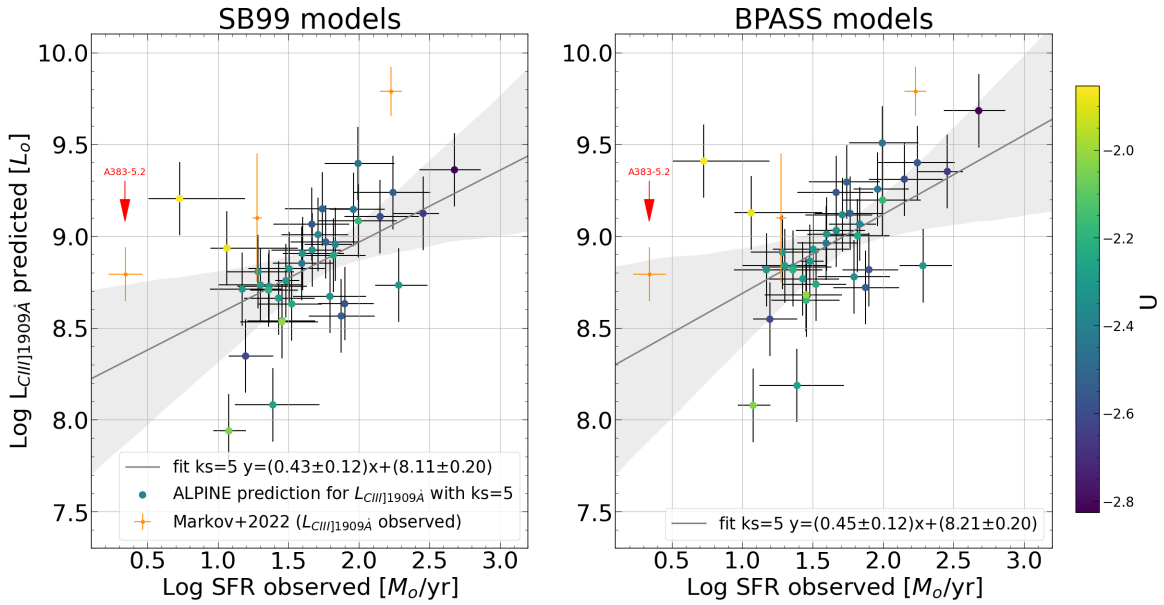

Figure 4.24: The predicted CIII] $1909\,\text{Å}$ luminosity as a function of SFR for the ALPINE sample. Best-fit relation (solid black line) obtained by performing a weighted linear regression. The errors in $L_{\text{CIII]}}$ are assumed as a percentage error of 20%. In the plot is reported the fiducial fit ($k_s = 5$). The r and the p-values associated are: r[SB99,BPASS]$= [0.549, 0.563]$, $p - value$[SB99,BPASS]$= [0.00111, 0.000896]$. Three galaxies from Markov et al. (2022) at redshift $z \sim 5$ are also reported as orange crosses. These galaxies are both [CII] and CIII] detected. The models have continuous SF with no quenching.

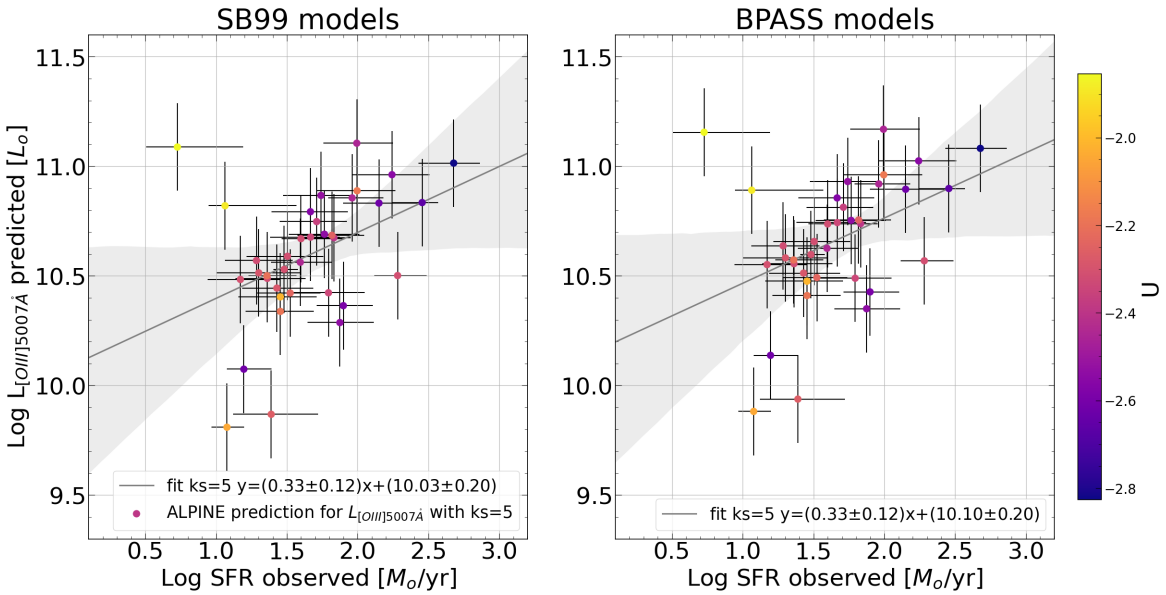

Figure 4.25: The predicted [OIII] $5007\,\text{Å}$ luminosity as a function of SFR for the ALPINE sample. Best-fit relation (solid black line) obtained by performing a weighted linear regression. The errors in $L_{\text{CIII]}}$ are assumed as a percentage error of 20%. In the plot is reported the fiducial fit ($k_s = 5$). The r and the p-values associated are: r[SB99,BPASS]$= [0.429, 0.425]$, $p-value$[SB99,BPASS]$= [0.00905, 0.00966]$. The models have continuous SF with no quenching.

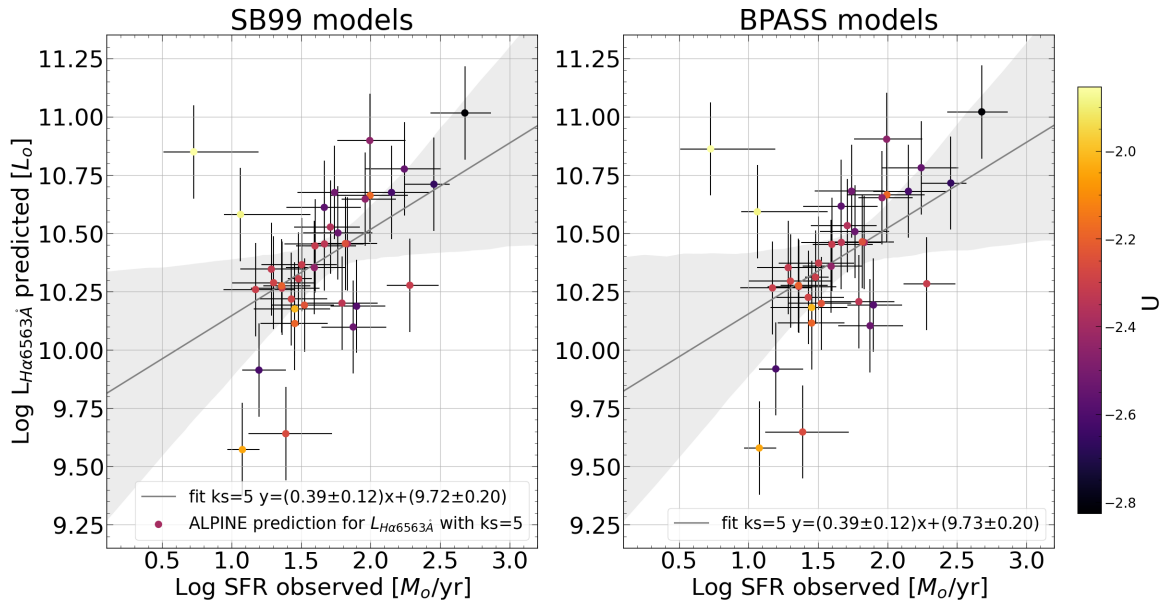

Figure 4.26: The predicted $H\alpha$ $6563\,\text{Å}$ luminosity as a function of SFR for the ALPINE sample. Best-fit relation (solid black line) obtained by performing a weighted linear regression. The errors in $L_{\text{CIII]}}$ are assumed as a percentage error of 20%. In the plot is reported the fiducial fit ($k_s = 5$). The r and the p-values associated are: r[SB99,BPASS]$= [0.489, 0.486]$, $p-value$[SB99,BPASS]$= [0.00247, 0.00266]$. The models have continuous SF with no quenching.

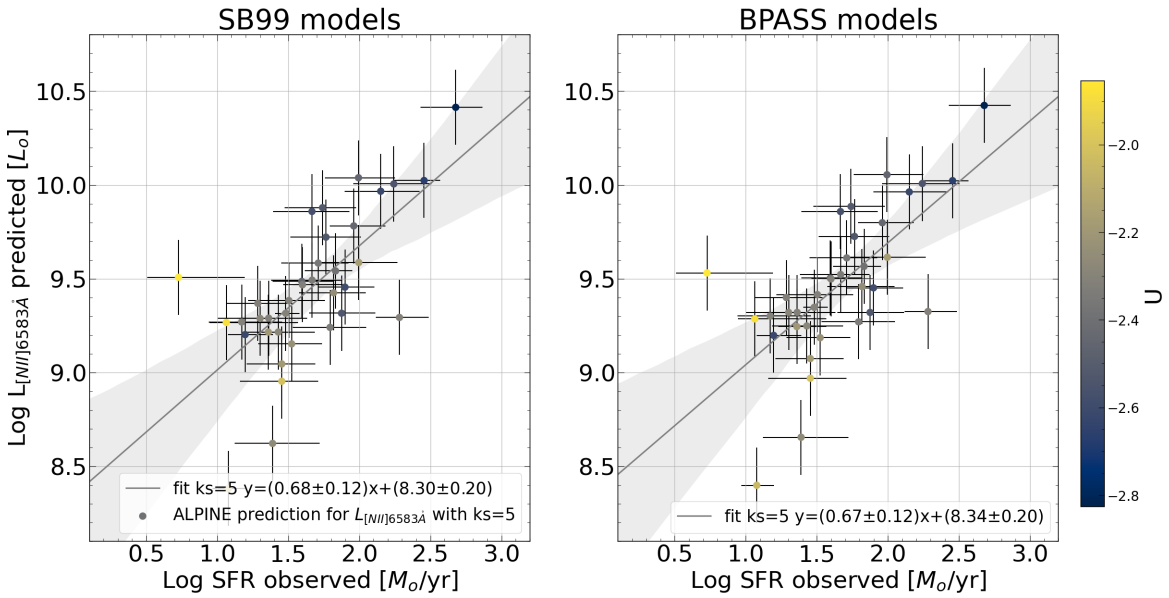

Figure 4.27: The predicted $[NII]\ 6583\,\text{Å}$ luminosity as a function of SFR for the ALPINE sample. Best-fit relation (solid black line) obtained by performing a weighted linear regression. The errors in $L_{\text{CIII]}}$ are assumed as a percentage error of 20%. In the plot is reported the fiducial fit ($k_s = 5$). The r and the p-values associated are: r[SB99,BPASS]$= [0.689, 0.693]$, $p - value$[SB99,BPASS]$= [3.33 \cdot 10^{-6}, 3.58 \cdot 10^{-6}]$. The models have continuous SF with no quenching.

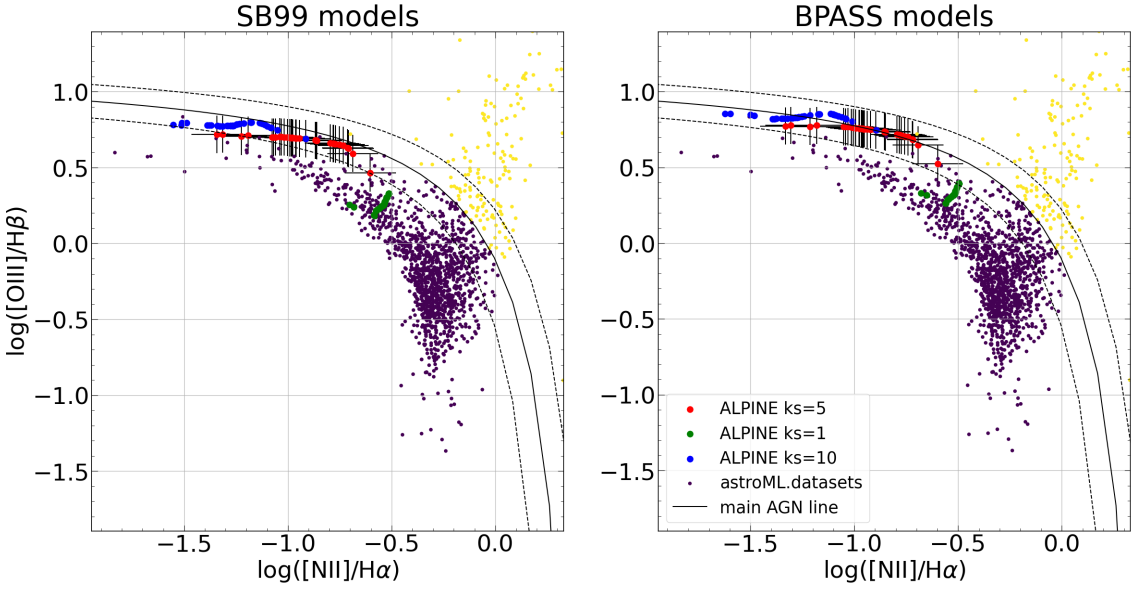

Figure 4.28: The BPT diagram. The violet and yellow points are from the astroML.datasets (Vanderplas et al., 2012) The violet points are galaxies without an AGN, and the yellow ones are AGN galaxies. The red, green and blue points are the predicted value for the ALPINE sample assuming respectively $k_s = 5, 1$ and 10. The model is with continuous SF with no quenching.

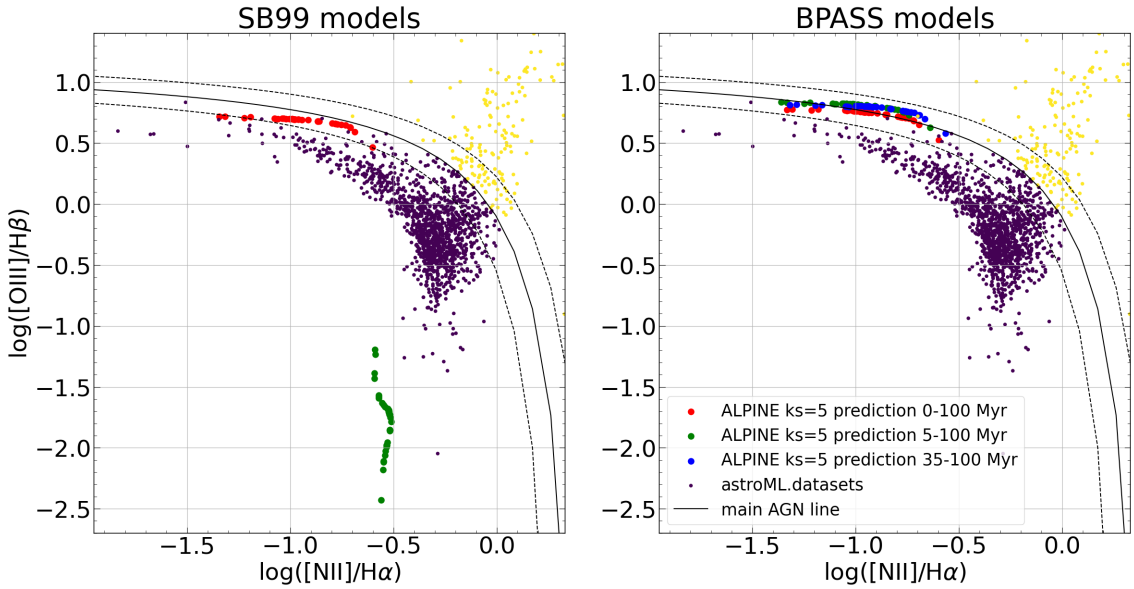

Figure 4.29: The BPT diagram. The violet and yellow points are from the astroML.datasets (Vanderplas et al., 2012) The violet points are galaxies without an AGN, and the yellow ones are AGN galaxies. The red points are the predicted value for the ALPINE sample in case of continous SF without quenching. The green points are the predicted value for the ALPINE sample in case of continous SF with quenching $5\,\mathrm{Myr}$ ago. The blue points for continous SF with quenching $35\,\mathrm{Myr}$ ago (out of axis range in SB99). All points are associated to the fiducial value $k_s = 5$.

Chapter 5

Conclusions and future perspectives

With my Thesis work, I highlighted the importance of developing simulations for photodissociation regions (PDRs) and HII regions able to connect the far-infrared (FIR) lines observed by ALMA with the ultra-violet (UV) and optical lines that are being observed in high-redshift galaxies by JWST. The possibility of finding a close connection between the UV lines and the properties of the high-redshift galaxies opens an important window in the characterisation of the ISM phases in EoR galaxies.

In my Thesis, I simulated FIR and UV/optical lines using the CLOUDY photoionisation code (Ferland et al., 2017) and two different codes for simulating the incident radiation field from a stellar population: Starburst99 (SB99, Leitherer et al. (1999)) and Binary Population and Spectral Synthesis Code (BPASS, Stanway & Eldridge (2018)). Both are spectral synthesis codes, but in BPASS the presence of a binary star population is included.

The main results obtained from this Thesis work are the following:

- I have shown the impact of binary stars in making the UV spectra harder, and in particular the increased importance of this type of star in the case of quenched star formation (SF).
- The presence of binary stars affects the free-electron temperature T_e (Figure 4.2) by widening the depth and increasing the temperature of the HII regions, and also affecting the element fraction densities for different ionisation levels (Figures 4.5,4.6,4.4 and 4.7). Therefore, the presence of binaries must be taken into account in the line emission modelling (e.g. Jaskot & Ravindranath (2016)).
- The developed models are validated using galaxies from datasets VANDELS, VUDS, and CANDELS/SHARDS in which observations for galaxies are presented at redshift $2.5 < z < 3.5$. In the figures of *Section* 4.3 it is visible that my models are able to reproduce the observed trend for reasonable assumption of physical parameters in the analysed galaxies.
- I derived the relations of the UV and optical lines (CIII] $1909\mathring{A}$, [OIII] $5007\mathring{A}$, $H\alpha$ $6563\mathring{A}$ and [NII] $6583\mathring{A}$) luminosities with the SFR, thanks to the use of an analytical model (Ferrara et al., 2019) that associates at each galaxy a value for

the physical parameter of my CLOUDY model: hydrogen density (n), ionisation parameter (U) and metallicity (Z). I have made ALPINE predictions for three different assumed values for the burstiness parameter k_s: $1, 5$ and 10. The fiducial value assumed for ALPINE is $k_s = 5$, as reported by (Markov et al., 2022) and (Vallini et al., 2021).
My predictions (see Figures 4.24,4.25,4.26 and 4.27), show a correlation between the UV/optical lines and the SFR, suggesting the use of these correlations at high-z, analogues to the [CII]-SFR relation found locally by De Looze et al. (2014). It is especially evident when considering two of the correlations that I have studied: CIII]-SFR and [NII]-SFR. The correlation coefficients for SB99 and the BPASS model in the CIII]-SFR relation are $r = 0.549$ and $r = 0.563$, respectively. The associated p-values for the two models are $p - value \approx 0.1\%$ and $p - value \approx 0.09\%$. Regarding the [NII]-SFR relation, for SB99 and BPASS models $r = 0.689$ and $r = 0.693$, respectively. The associated p-values for the two models are $p - value \approx 0.00033\%$ and $p - value \approx 0.00036\%$. These relations could be, if confirmed by observations with JWST, important tools for characterising the SFR of high redshift galaxies using UV and optical lines. This is especially true for the [NII]-SFR relation, which has shown the best linear correlation in my studies.

- I made a prediction about the BPT diagram (Baldwin et al., 1981) positions for the ALPINE galaxies. I showed that BPT lines are influenced by different star formation efficiency (SFE) of the galaxies, which in my models is connected to the value of the burstiness parameter k_s. For higher values of k_s, we have a higher SFE. This impacts the incident radiation: more young stars implies a large emission of ionising photons. The impact of an increase of SFE in the BPT diagram is that higher values of k_s correspond to predictions moving toward the AGN region (Figure 4.28). Moreover, binaries change the predicted location of galaxies within the BPT, in particular for the quenched SFH the BPASS models return a much larger value for $\log([OIII]/H\beta)$ with respect to that from SB99. This is due to the harder spectrum of stellar populations that include binary stars. In SB99, the UV photon budget drops dramatically immediately after the quenching, while this is not the case for BPASS where the mass accretion processes in the closed binary systems provide an additional channel for the UV photon production at older ages (Figure 4.29). In conclusion, the BPT diagram predictions are strongly dependent on the presence of binaries in the stellar population, on the SFH, and on the SFE. This raises the questions of how significant binaries, burstiness parameter and SFH are in EoR galaxies and if they can imitate an AGN in a BPT diagram. To answer this, more complex CLOUDY models must be developed that take into account the presence of an AGN in the incident radiation and make line predictions accordingly. These predictions must then be validated with data from JWST and zoom-in cosmological simulations.

In the future, the JWST proposal accepted (*PI: A.Faisst*) will enable us to observe 18 representative ALPINE galaxies between $4.4 < z < 5.7$ with NIRSpec, and obtain all major optical emission lines ([OII], Hβ, [OIII], [NII], Hα and [SII]). This will be essential to confirm the predictions made in this work and make necessary adjustments to the models in order to characterise the ISM properties of some of the ALPINE galaxies. Furthermore, to gain a better understanding of the real impact of binaries on these

predictions, it is important to include models that take into account the presence of an AGN in this work. This will help us to determine the relative importance of binary stars compared to AGN in EoR galaxies, and also to check the validity of the BPT diagram for high-z galaxies. In order to make these futures works simpler, I have organised all models in a cloud directory (CLOUDY models).

Acknowledgments

I am deeply grateful to my supervisors Livia Vallini and Francesca Pozzi for their continuous support and guidance throughout the writing of this Master Thesis. I am deeply grateful to my co-supervisor Federico Esposito for his invaluable help in teaching me the CLOUDY code and for his thoughtful remarks on the data analysis.

I am grateful to Diego Zuccato for his assistance with the OPH cluster during the technical implementation of my models. I am also thankful to Jan Eldridge for responding to my queries regarding the BPASS code used in the creation of my Thesis.

I am grateful to my course mate for the shared experiences over the past two years. I am thankful to my friends for their unwavering support and patience throughout this period. I am also thankful to my family for their backing during these two difficult years and for their ongoing support.

Il maestro ed io entrammo in quel cammino nascosto per tornare alla luce del sole; e senza prenderci un attimo di riposo salimmo in alto, lui per primo e io dietro, fino a quando vidi gli astri del cielo attraverso un'apertura circolare. E di lì uscimmo per rivedere le stelle.

Appendix

Appendix A: Escape probability formalism

This approximation is based on the idea that the various regions of the medium are not radiatively linked, meaning that the photons emitted are either re-absorbed close to the point of emission or escape from the medium. Only when there is a great difference in speed between two points can this occur, and this approximation is known as a large velocity gradient (LVG) approximation. With LVG the Doppler shift moves the frequency of a photon emitted in a certain region to a frequency that cannot be absorbed at any other point of the medium.

For simplicity, we assume that the field is only caused by the medium when using the Escape Probability Formalism. We define the probability β of a photon to escape from the medium ($0 < \beta < 1$) as dependent only on the geometry and the optical depth of the medium. The escape probability formalism assumes that the radiative field of the medium can be expressed as:

$$J_\nu = S_\nu(1 - \beta) \tag{1}$$

When β is equal to zero, no photons are able to leave the medium, whereas when it is set to one, all photons are able to escape. Considering the expression of the source function using the Einstein coefficients, $S_\nu = (n_u A_{ul})/(n_l B_{lu} - n_u B_{ul})$, and using the escape probability formalism in the statistical equilibrium equation (Eq.1.7), we obtain the following solution:

$$\frac{n_u}{n_l} = \frac{g_u}{g_l} exp(-(E_u - E_l)/k_b T) \frac{1}{a + \beta \frac{n_{crit}}{n_{coll}}} \tag{2}$$

We will consider a semi-infinite homogeneous slab and calculate the value of β. Let us assume that the radiation field is caused only by the medium and that the slab of material has constant ρ, T, and S_ν throughout the slab (a plane-parallel slab). We have so the following equations:

$$\begin{aligned} I_\nu &= S_\nu(1 - e^{-\tau}) \\ J_\nu &= S_\nu(1 - \beta) \end{aligned} \tag{3}$$

We can calculate β by considering the line emission distribution $\phi(\nu)$ and the optical depth of the medium τ:

$$\beta = \frac{1}{4\pi} \int \phi(\nu) e^{-\tau} dv d\Omega \tag{4}$$

For a homogeneous semi-infinite slab, we have the following approximations:

$$\begin{aligned} \tau << 1 \rightarrow \beta \approx 1/2 \\ \tau >> 1 \rightarrow \beta \propto 1/\tau \end{aligned} \tag{5}$$

For an emission line with a Gaussian profile (Doppler shape), the optical depth can be determined by using the semi-infinite homogeneous slab approximation and assuming all molecules/atoms are in the lower energy level. This value is dependent on the column density of the medium.

$$\tau = \frac{A_{ul} c 3 N_H}{8\pi\nu_0 3b} \frac{g_u}{g_l} \tag{6}$$

where N_H is the hydrogen column density.

Appendix B: Spectroscopy Term

If we have a system of N electrons, each electron has an orbital angular momentum of lh and a spin angular momentum of $h/2$. The $L-S$ coupling approximation states that the total angular momentum of N electrons is the sum of their individual orbital and spin angular momenta. Specifically, L is the sum of the individual orbital angular momenta and S is the sum of the individual spin angular momenta. The total angular momentum is $J = L + S$. With these definitions, we can introduce the energy level notation: $(2S+1)L_J^P$, where P is the parity.

Appendix C: CLOUDY Models

The models and codes that have been created are collected in this Google Drive folder: CLOUDY models.

Appendix D: Composite stellar population code

```
import pandas as pd
import numpy as np
from subprocess import run as rn

directory= <directory>
sed = pd.read_csv(directory, header=None, delimiter='\s+')

initial_age= 6.05
step_eta= 0.1

eta=[]
eta.append("Wavelenght")
eta.append("10^"+str(initial_age))

for i in range(1,51,1):
  eta.append("10^"+"{:.2f}".format(initial_age+step_eta*i))

```

```
sed.columns = eta

#now time to produce 10 Myr SED with constant SFR

#F(lambda)=f0delta0+ sum(fi*step_i)

Ftot=[]
Ftot.append(("Wavelenght","Flux"))

Fo=sed["10^6.05"]*10**6.05

Fi=[]
Fsum=Fo

for i in range (2,21,1):
  exp1=6.15+0.1*(i-1)
  exp2=6.05+0.1*(i-1)
  deltaI=10**exp1-10**exp2
  Fi=sed["10^"+"{:.2f}".format(initial_age+step_eta*i)]*deltaI
  Fsum+=Fi


for i in range (0,100000,1):
  Ftot.append((sed["Wavelenght"][i],Fsum[i]))

#units Angstroms
#Flambda units Angstroms

new_sed=open("Bpass_0.020_0-100Myr.sed","x")
new_sed.write("#BPASS Angstroms Lo/A\n") #nuFnu
new_sed.write(str(Ftot[1][0])+"      "+str(Ftot[1][1])+" Flambda units
    Angstroms\n")

for i in range(2,len(Ftot)):
  new_sed.write(str(Ftot[i][0])+"      "+str(Ftot[i][1])+"\n")


new_sed.write("**********")
```

This programme utilises the equations outlined in Section 2.3.2 by employing a series of `for` cycles. A composite stellar population is constructed to reach an age of $100\,\mathrm{Myr}$ by combining ten different starbursts, resulting in a star formation rate of $1\,\mathrm{M}_{\odot}\,\mathrm{yr}^{-1}$. The code produces a `.sed` file containing the results, which can be read by CLOUDY code as a spectral energy distribution (SED) shape. The file reports the wavelength and the associated flux per unit of Angstrom.

Appendix E: CLOUDY input file

An example of CLOUDY input file for a BPASS SED model:

```
title U_hden_Z_SED_0.008
set save prefix "pdr"
table SED "Bpass_0.008_100Myr.sed"
ionization parameter -3
hden 0.5
abundances GASS no grains
```

```
metals and grains linear 0.15
turbulence 1.5 km/s
CMB, z=6
cosmic rays background
iterate to convergence
database H2
grains ISM no qheat
grains PAH no qheat function 3
stop temperature off
stop column density 22
#
# SAVE COMMANDS
#
save last overview last ".ovr"
save last PDR ".pdr"
save last heating ".het"
save last cooling ".col"
save last lines, array ".lina" last, units microns
save last continuum last ".con" units microns
save last species all densities ".spc"
save last grain temperature last ".grntem"
save last lines zone cumulative emergent ".linc"
...
end of lines
```

Appendix F: CLOUDY input files generation

An example of the python/bash code used for generate all the CLOUDY input files for different SED shape models:

```
from subprocess import run as rn

def decimal_range(start, stop, increment):
    while start < stop: # and not math.isclose(start, stop): Py>3.5
        yield start
        start += increment

rn("cd /home/STUDENTI/enrico.veraldi/cloudy_run/pdr_U_hden_0.008_sphere/
   ",shell=True)
rn("rm sbatch_script.sh",shell=True)
rn("touch sbatch_script.sh",shell=True)

script=open("sbatch_script.sh","w")
directory="/home/STUDENTI/enrico.veraldi/cloudy_run/pdr_U_hden_0.008
   _sphere/"
cloudy_path="/home/software/astro/cloudy/c22.02/source/cloudy.exe -r"

script.write("#!/bin/bash \n")
script.write("#SBATCH --partition=m1 \n")
script.write("#SBATCH --account=astro \n")
script.write("#SBATCH --time=08:00:00 \n")
script.write("#SBATCH --nodes=1 \n")
script.write("#SBATCH --ntasks-per-node=56 \n")
script.write("#SBATCH --constrain=ib \n")
script.write("#SBATCH --mem=250000 \n")
script.write("#SBATCH --job-name=\"cloudy22\" \n")
```

```
script.write("#SBATCH --mail-user=enrico.veraldi@studio.unibo.it \n")
script.write("#SBATCH --mail-type=ALL \n")
script.write("\n")

script.write("cd "+str(directory)+"\n")

for i in decimal_range(-3,0,0.5): #U
  for j in decimal_range(0.5,4,0.5): #hden
    for k in decimal_range(0.15,0.55,0.10): #Z percentage

      rn("cp pdr_BPASS.in pdr_U"+"{:.2f}".format(i)+"_hden"+"{:.2f}".format(j)+"_Z"+"{:.2f}".format(k)+".in",shell=True)
      rn("sed -i \"s/ionization parameter -3/ionization parameter "+"{:.2f}".format(i)+"/\" "+" pdr_U"+"{:.2f}".format(i)+"_hden"+"{:.2f}".format(j)+"_Z"+"{:.2f}".format(k)+".in",shell=True)
      rn("sed -i \"s/ionization parameter -3/ionization parameter "+"{:.2f}".format(i)+"/\" "+" pdr_U"+"{:.2f}".format(i)+"_hden"+"{:.2f}".format(j)+"_Z"+"{:.2f}".format(k)+".in",shell=True)
      rn("sed -i \"s/ionization parameter -3/ionization parameter "+"{:.2f}".format(i)+"/\" "+" pdr_U"+"{:.2f}".format(i)+"_hden"+"{:.2f}".format(j)+"_Z"+"{:.2f}".format(k)+".in",shell=True)
      rn("sed -i \"s/ionization parameter -3/ionization parameter "+"{:.2f}".format(i)+"/\" "+" pdr_U"+"{:.2f}".format(i)+"_hden"+"{:.2f}".format(j)+"_Z"+"{:.2f}".format(k)+".in",shell=True)
      rn("sed -i \"s/ionization parameter -3/ionization parameter "+"{:.2f}".format(i)+"/\" "+" pdr_U"+"{:.2f}".format(i)+"_hden"+"{:.2f}".format(j)+"_Z"+"{:.2f}".format(k)+".in",shell=True)
      rn("sed -i \"s/ionization parameter -3/ionization parameter "+"{:.2f}".format(i)+"/\" "+" pdr_U"+"{:.2f}".format(i)+"_hden"+"{:.2f}".format(j)+"_Z"+"{:.2f}".format(k)+".in",shell=True)
      rn("sed -i \"s/ionization parameter -3/ionization parameter "+"{:.2f}".format(i)+"/\" "+" pdr_U"+"{:.2f}".format(i)+"_hden"+"{:.2f}".format(j)+"_Z"+"{:.2f}".format(k)+".in",shell=True)
      rn("sed -i \"s/ionization parameter -3/ionization parameter "+"{:.2f}".format(i)+"/\" "+" pdr_U"+"{:.2f}".format(i)+"_hden"+"{:.2f}".format(j)+"_Z"+"{:.2f}".format(k)+".in",shell=True)
      rn("sed -i \"s/ionization parameter -3/ionization parameter "+"{:.2f}".format(i)+"/\" "+" pdr_U"+"{:.2f}".format(i)+"_hden"+"{:.2f}".format(j)+"_Z"+"{:.2f}".format(k)+".in",shell=True)
      rn("sed -i \"s/hden 0/hden "+"{:.2f}".format(j)+"/\" "+" pdr_U"+"{:.2f}".format(i)+"_hden"+"{:.2f}".format(j)+"_Z"+"{:.2f}".format(k)+".in",shell=True)
      rn("sed -i \"s+metals and grains linear 0.15+metals and grains linear "+"{:.2f}".format(k)+"+\" "+" pdr_U"+"{:.2f}".format(i)+"_hden"+"{:.2f}".format(j)+"_Z"+"{:.2f}".format(k)+".in",shell=True)
      rn("sed -i \"s/set save prefix \\\"pdr\\\"/set save prefix \\\"pdr_U"+"{:.2f}".format(i)+"_hden"+"{:.2f}".format(j)+"_Z"+"{:.2f}".format(k)+"\\\"/\" "+ " pdr_U"+"{:.2f}".format(i)+"_hden"+"{:.2f}".format(j)+"_Z"+"{:.2f}".format(k)+".in",shell=True)
      rn("wait",shell=True)
      script.write(str(cloudy_path)+" pdr_U"+"{:.2f}".format(i)+"_hden"+"{:.2f}".format(j)+"_Z"+"{:.2f}".format(k)+" & \n")


script.write("wait \n")
```

Appendix G: ALPINE predictions for quenched SF model

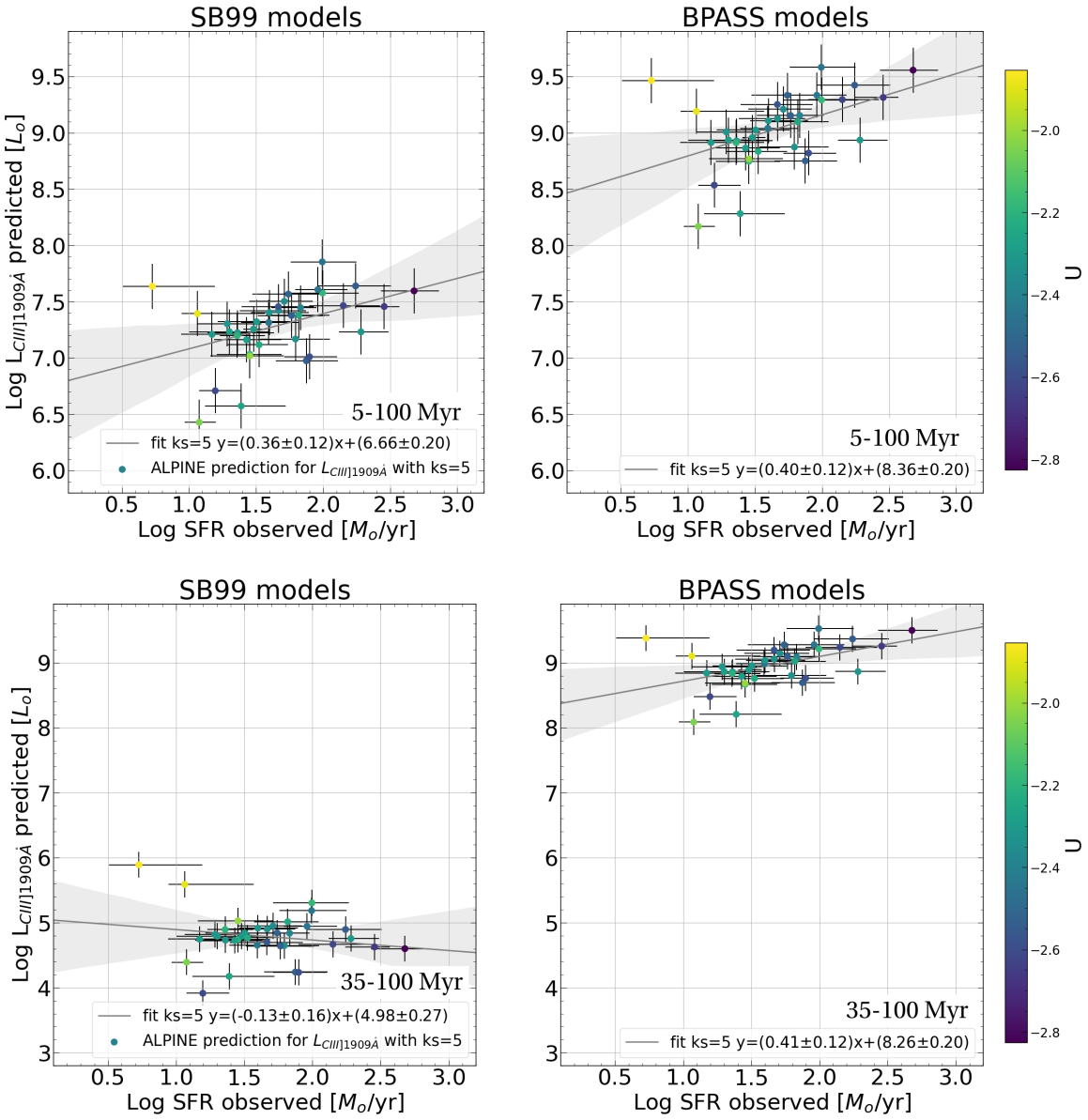

Figure 1: The luminosity of CIII] $1909\,\text{Å}$ predicted from my models as a function of the SFR for the ALPINE sample. The best-fit relation (solid black line) is obtained by performing a weighted linear regression, assuming as weight the quadratic sum of the errors in SFR and $L_{\text{CIII]}}$ (for the last one I have assumed a percentage error of 20%). The fit was performed for three different values of burstiness parameter $k_s(1, 5, 10)$ associated to the theoretical evaluation of n, U and Z (Ferrara et al., 2019) In the plot is reported the fiducial fit, assumed in the theoretical computation with $k_s = 5$. The upper panels are related to quenched SF 5 Myr ago, the lower panels are related to quenched SF 35 Myr ago.

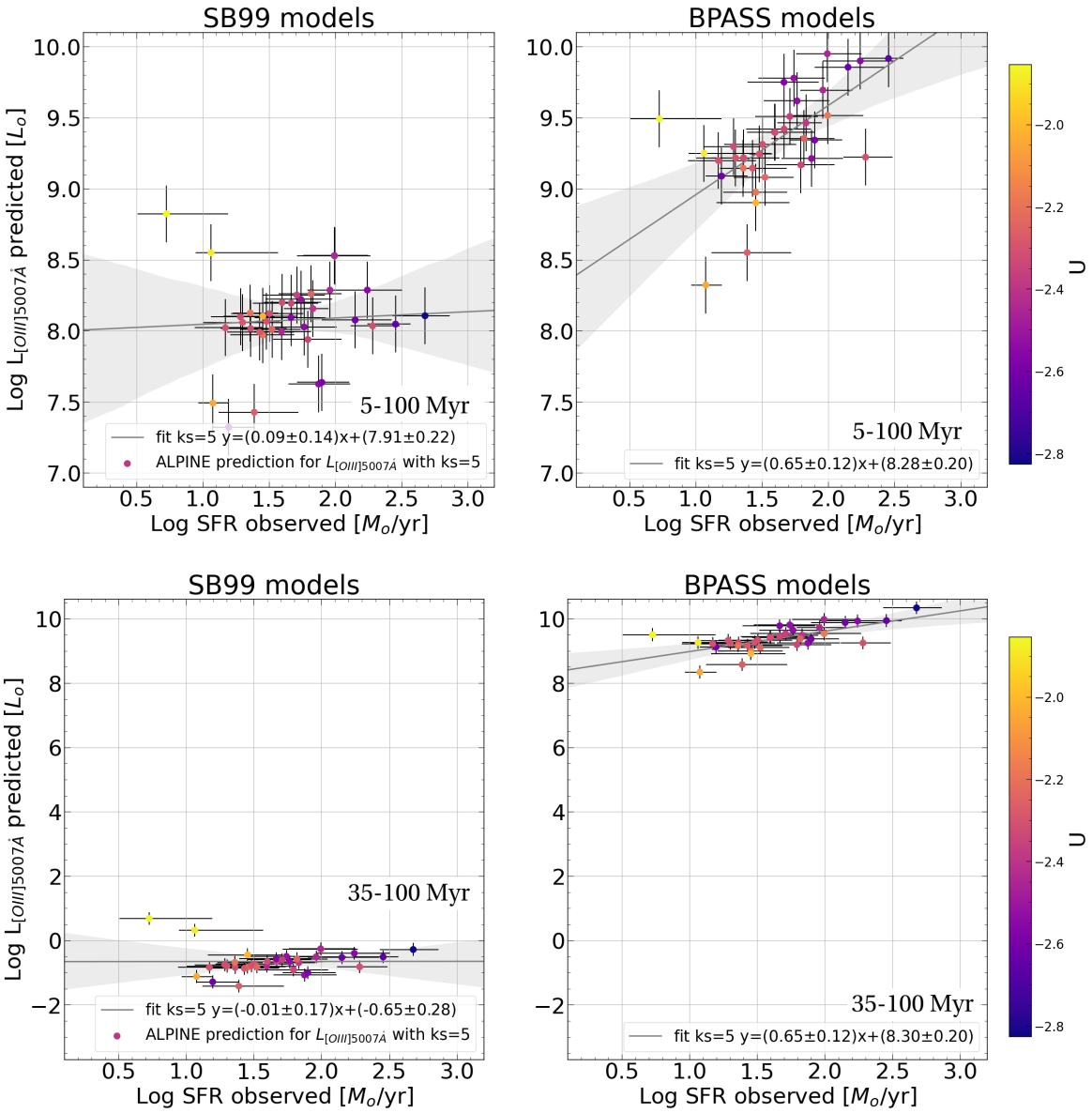

Figure 2: The luminosity of [OIII] $5007\,\text{Å}$ predicted from my models as a function of the SFR for the ALPINE sample. The best-fit relation (solid black line) is obtained by performing a weighted linear regression, assuming as weight the quadratic sum of the errors in SFR and $L_{[\text{OIII}]}$ (for the last one I have assumed a percentage error of 20%). The fit was performed for three different values of burstiness parameter $k_s(1, 5, 10)$ associated to the theoretical evaluation of n, U and Z (Ferrara et al., 2019) In the plot is reported the fiducial fit, assumed in the theoretical computation with $k_s = 5$. The upper panels are related to quenched SF 5 Myr ago, the lower panels are related to quenched SF 35 Myr ago.

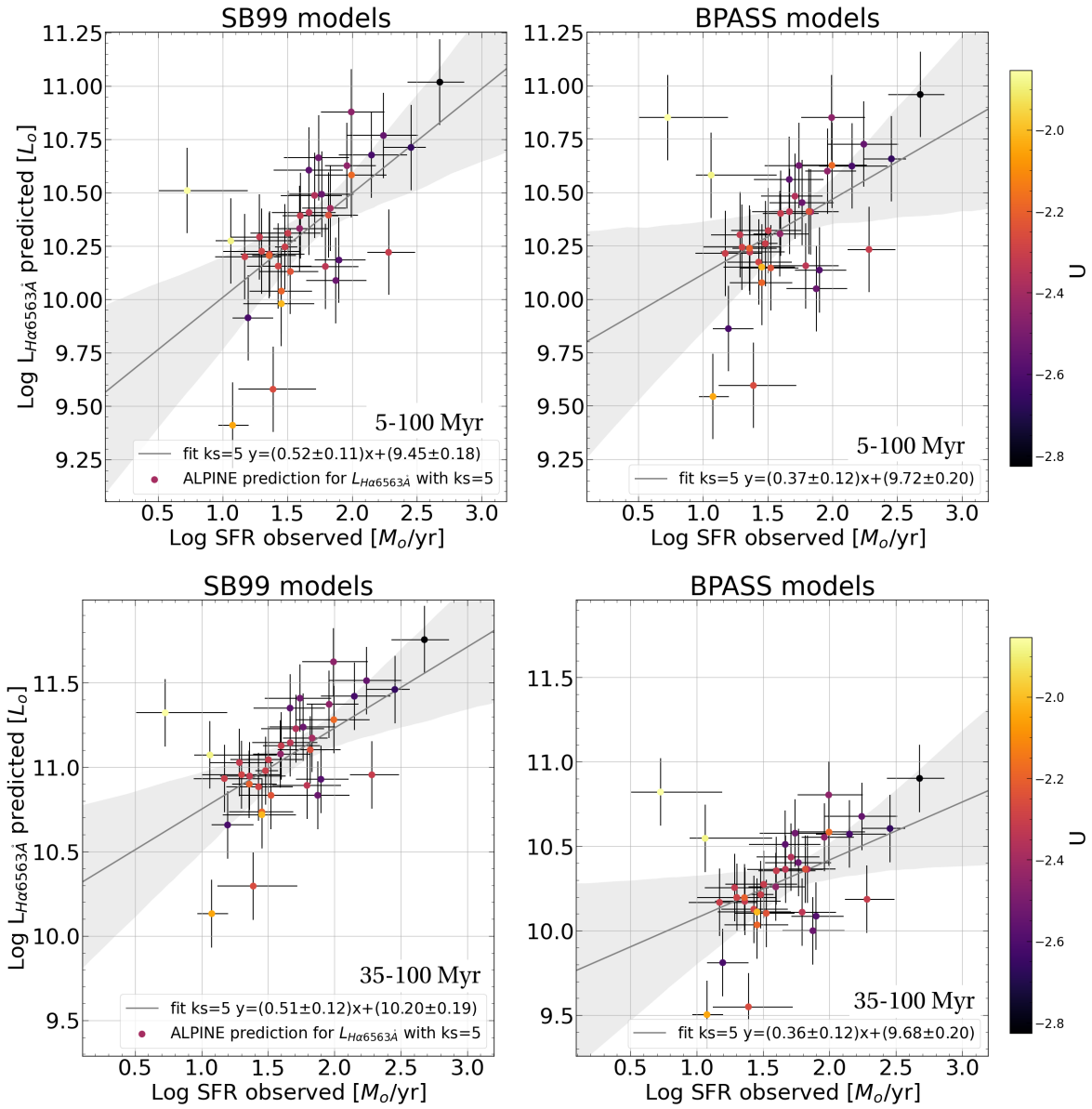

Figure 3: The luminosity of $H\alpha$ $6563\,\text{Å}$ predicted from my models as a function of the SFR for the ALPINE sample. The best-fit relation (solid black line) is obtained by performing a weighted linear regression, assuming as weight the quadratic sum of the errors in SFR and $L_{\text{H}\alpha}$ (for the last one I have assumed a percentage error of 20%). The fit was performed for three different values of burstiness parameter $k_s(1, 5, 10)$ associated to the theoretical evaluation of n, U and Z (Ferrara et al., 2019) In the plot is reported the fiducial fit, assumed in the theoretical computation with $k_s = 5$. The upper panels are related to quenched SF 5 Myr ago, the lower panels are related to quenched SF 35 Myr ago.

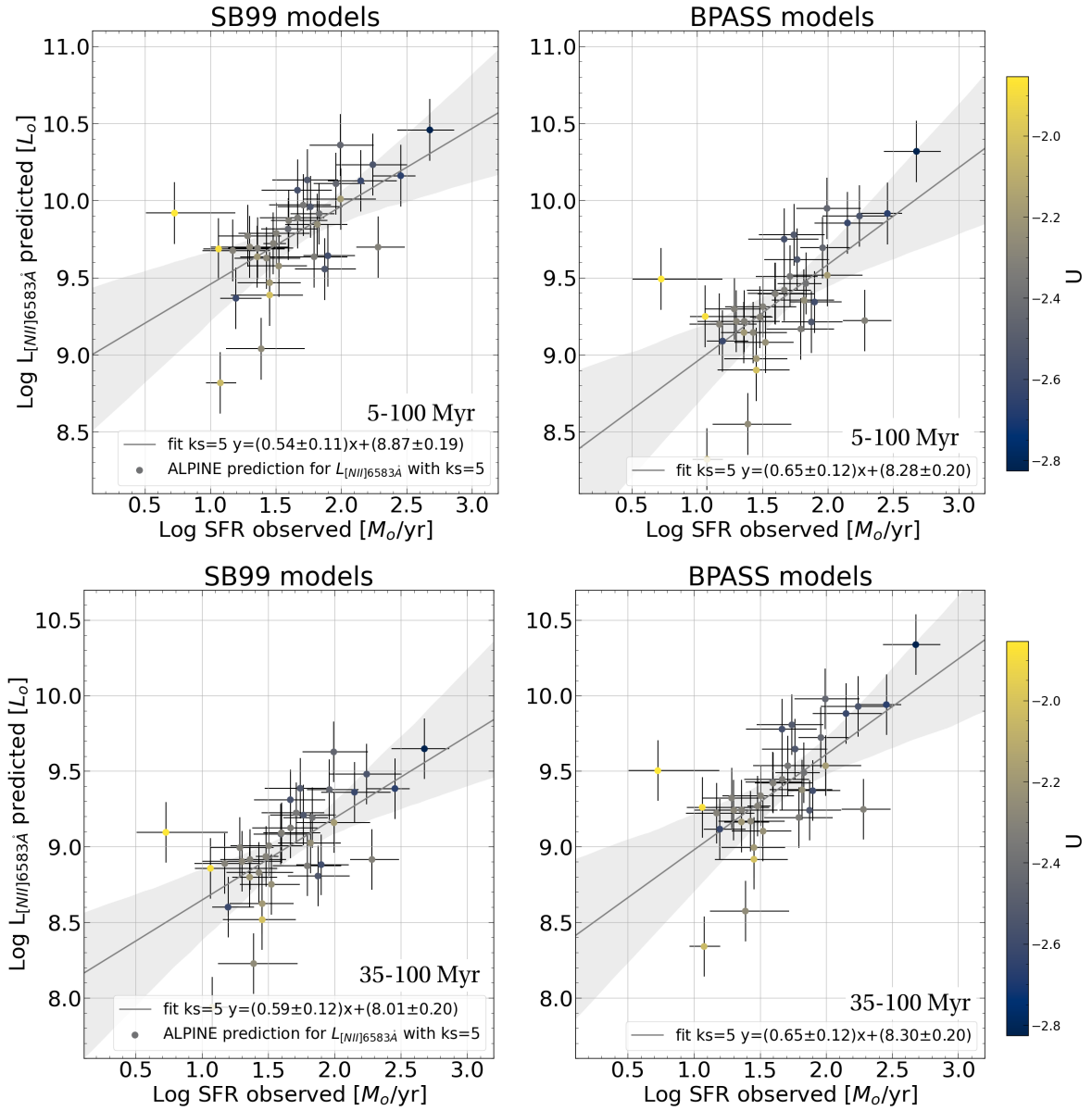

Figure 4: The luminosity of [NII] $6583\,\text{Å}$ predicted from my models as a function of the SFR for the ALPINE sample. The best-fit relation (solid black line) is obtained by performing a weighted linear regression, assuming as weight the quadratic sum of the errors in SFR and $L_{[\text{NII}]}$ (for the last one I have assumed a percentage error of 20%). The fit was performed for three different values of burstiness parameter $k_s(1, 5, 10)$ associated to the theoretical evaluation of n, U and Z (Ferrara et al., 2019) In the plot is reported the fiducial fit, assumed in the theoretical computation with $k_s = 5$. The upper panels are related to quenched SF 5 Myr ago, the lower panels are related to quenched SF 35 Myr ago.

Bibliography

Amenomori M., et al., 2008, ApJ, 678, 1165

Baldwin J. A., Phillips M. M., Terlevich R., 1981, PASP, 93, 5

Barro G., et al., 2019, ApJS, 243, 22

Baskin A., Laor A., 2005, MNRAS, 358, 1043

Baumjohann Wolfgang; Treumann R. A., 2006, Basic Space Plasma Physics. London: Imperial College Press

Béthermin M., et al., 2020, A&A, 643, A2

Bianchi S., 2013, A&A, 552, A89

Bouwens R. J., et al., 2022, ApJ, 931, 160

Burgarella D., et al., 2022, A&A, 664, A73

Carniani S., Maiolino R., Smit R., Amorín R., 2018, ApJ, 854, L7

Clarke C., Carswell B., 2014, Principles of Astrophysical Fluid Dynamics

Coles & Lucchin 2002, Cosmology: The Origin and Evolution of Cosmic Structure

De Looze I., et al., 2014, A&A, 568, A62

Dessauges-Zavadsky M., et al., 2020, A&A, 643, A5

Draine 2011, Physics of the Interstellar and Intergalactic Medium

Dunlop J. S., et al., 2021, PRIMER: Public Release IMaging for Extragalactic Research, JWST Proposal. Cycle 1, ID. #1837

Eisenstein D. J., et al., 2023, arXiv e-prints, p. arXiv:2306.02465

Eldridge J. J., Stanway E. R., 2022, ARA&A, 60, 455

Faisst A. L., et al., 2020, ApJS, 247, 61

Ferland G. J., et al., 2017, Rev. Mexicana Astron. Astrofis., 53, 385

Ferrara A., Vallini L., Pallottini A., Gallerani S., Carniani S., Kohandel M., Decataldo D., Behrens C., 2019, MNRAS, 489, 1

Froebrich D., Rowles J., 2010, MNRAS, 406, 1350

Fudamoto Y., et al., 2022, ApJ, 934, 144

Fujimoto S., et al., 2020, ApJ, 900, 1

Furtak L. J., et al., 2023, ApJ, 952, 142

Gardner J. P., et al., 2006, Space Sci. Rev., 123, 485

Giavalisco M., et al., 2004, ApJ, 600, L93

Goulding A. D., et al., 2023, arXiv e-prints, p. arXiv:2308.02750

Grevesse N., Asplund M., Sauval A. J., Scott P., 2010, Ap&SS, 328, 179

Grogin N. A., et al., 2011, ApJS, 197, 35

Gruppioni C., et al., 2020, A&A, 643, A8

Habing H. J., 1968, Bull. Astron. Inst. Netherlands, 19, 421

Hamann M. G., Barlow C. S., 1997, The Astrophysical Journal, 489, 698

Hansen C. J., Kawaler S. D., 1994, Stellar Interiors. Physical Principles, Structure, and Evolution., doi:10.1007/978-1-4419-9110-2.

Harikane Y., et al., 2022, ApJS, 259, 20

Harrison C. M., Alexander D. M., Mullaney J. R., Swinbank A. M., 2014, MNRAS, 441, 3306

Haverkorn M., Spangler S. R., 2013, Space Sci. Rev., 178, 483

Hernández-Vera C., et al., 2023, A&A, 677, A152

Hilborn R. C., 2002, arXiv e-prints, p. physics/0202029

Hogg R. V.; Craig A. T., 1978, Introduction to Mathematical Statistics (4th ed.). New York: Macmillan. pp. Remark 3.3.1.

Indriolo N., Geballe T. R., Oka T., McCall B. J., 2007, ApJ, 671, 1736

Jaskot A. E., Ravindranath S., 2016, ApJ, 833, 136

Karttunen 2007, Fundamental Astronomy

Kennicutt Robert C. J., 1998, ARA&A, 36, 189

Kennicutt R. C., Evans N. J., 2012, ARA&A, 50, 531

Lagache G., Cousin M., Chatzikos M., 2018, A&A, 609, A130

Larson R. L., et al., 2023, arXiv e-prints, p. arXiv:2303.08918

Le Fèvre O., et al., 2019, A&A, 625, A51

Le Fèvre O., et al., 2020, A&A, 643, A1

Leitherer C., et al., 1999, ApJS, 123, 3

Llerena M., et al., 2023, A&A, 676, A53

Loiacono F., et al., 2021, A&A, 646, A76

Maiolino R., et al., 2015, MNRAS, 452, 54

Maiolino R., et al., 2023a, arXiv e-prints, p. arXiv:2305.12492

Maiolino R., et al., 2023b, arXiv e-prints, p. arXiv:2308.01230

Markov V., Carniani S., Vallini L., Ferrara A., Pallottini A., Maiolino R., Gallerani S., Pentericci L., 2022, A&A, 663, A172

Mascia S., et al., 2023, A&A, 672, A155

Osterbrock D. E., Ferland G. J., 2006, Astrophysics of gaseous nebulae and active galactic nuclei

Pallottini A., et al., 2022, MNRAS, 513, 5621

Pozzi F., et al., 2021, A&A, 653, A84

Rybicki & Lightman 2004, Radiative processes in astrophysics. WILEY-VCH Verlag GmbH & Co. KGaA

Schaerer D., et al., 2020, A&A, 643, A3

Schmidt M., 1959, ApJ, 129, 243

Scoville N., 2007, in Baker A. J., Glenn J., Harris A. I., Mangum J. G., Yun M. S., eds, Astronomical Society of the Pacific Conference Series Vol. 375, From Z-Machines to ALMA: (Sub)Millimeter Spectroscopy of Galaxies. p. 166

Seabold S., Perktold J., 2010, in 9th Python in Science Conference.

Stanway E. R., Eldridge J. J., 2018, MNRAS, 479, 75

Strömgren B., 1939, ApJ, 89, 526

Tielens 2005, The physics and chemistry of the interstellar medium. Cambridge University Press, The Edinburgh Building, Cambridge, UK

Topping M. W., et al., 2022, MNRAS, 516, 975

Vallini L., Ferrara A., Pallottini A., Carniani S., Gallerani S., 2021, MNRAS, 505, 5543

Vanderplas J., Connolly A., Ivezić Ž., Gray A., 2012, in Conference on Intelligent Data Understanding (CIDU). pp 47 –54, doi:10.1109/CIDU.2012.6382200

Wang J., Mao Y. F., Wei J. Y., 2011, ApJ, 741, 50

Waskom M. L., 2021, Journal of Open Source Software, 6, 3021

Wolfire M. G., Vallini L., Chevance M., 2022, ARA&A, 60, 247

Wootten A., Thompson A. R., 2009, IEEE Proceedings, 97, 1463

Yang G., et al., 2023, arXiv e-prints, p. arXiv:2307.14509

Zanella A., et al., 2018, MNRAS, 481, 1976